PHOTOMEDICINE
AND
PHOTOBIOLOGY

Vol.43, 44   2023

CONTENTS

【Article】

Wataru Kashihara and Tadashi Suzuki*

Department of Chemistry and Biological Science, Aoyama Gakuin University,,
5-10-1 Fuchinobe, Chuo-ku, Sagamihara, Kanagawa 252-5258, Japan

Megumi Mizawa[1]*, Hiroshi Hara[2], Teruhiko Makino[1], Tadamichi Shimizu[1]

[1] *Department of Dermatology, Faculty of Medicine, Academic Assembly, University of Toyama, Toyama, Japan*
[2] *Department of Dermatology, Nigata Prefectural Central Hospital, Joetsu, Japan*

Kazutaka Hirakawa[1,2,3,4*], Ayano Katayama[1], Shinya Yamaoka[2], and Shigetoshi Okazaki[5]

[1] *Department of Applied Chemistry and Biochemical Engineering, Faculty of Engineering, Shizuoka University, Johoku 3-5-1, Naka-ku, Hamamatsu, Shizuoka 432-8561, Japan*
[2] *Applied Chemistry and Biochemical Engineering Course, Department of Engineering, Graduate School of Integrated Science and Technology, Shizuoka University, Johoku 3-5-1, Naka-ku, Hamamatsu 432-8561, Japan*
[3] *Department of Optoelectronics and Nanostructure Science, Graduate School of Science and Technology, Shizuoka University, Johoku 3-5-1, Naka-ku, Hamamatsu, Shizuoka 432-8561, Japan*
[4] *Cooperative Major in Medical Photonics, Shizuoka University, Johoku 3-5-1, Hamamatsu 432-8561, Japan*
[5] *Preeminent Medical Photonics Education and Research Center, Hamamatsu University School of Medicine, Handayama 1-20-1, Higashi-ku, Hamamatsu, Shizuoka 431-3192, Japan*

Kousuke Meisho, Tatsuya Nishihara, and Kazuhito Tanabe

Department of Chemistry and Biological Science, College of Science and Engineering, Aoyama Gakuin University, 5-10-1 Fuchinobe, Chuo-ku, Sagamihara, Kanagawa 252-5258, Japan

Soyoung Park,*[,1] and Hiroshi Sugiyama*[,2]

[1] *Immunology Frontier Research Center, Osaka University, Yamadaoka, Suita, Osaka, 565-0871, Japan*
[2] *Institute for Integrated Cell-Material Sciences (iCeMS), Kyoto University, Yoshida-ushinomiyacho, Sakyo-ku, Kyoto 606-8501, Japan*

Kazutaka Hirakawa[1,2,3*], Satoki Matsui[1], and Shigetoshi Okazaki[45]

[1] *Applied Chemistry and Biochemical Engineering Course, Department of Engineering, Graduate School of Integrated Science and Technology, Shizuoka University, Johoku 3-5-1, Naka-ku, Hamamatsu 432-8561, Japan*

[2] *Department of Optoelectronics and Nanostructure Science, Graduate School of Science and Technology, Shizuoka University, Johoku 3-5-1, Naka-ku, Hamamatsu, Shizuoka 432-8561, Japan*

[3] *Cooperative Major in Medical Photonics, Shizuoka University, Johoku 3-5-1, Hamamatsu 432-8561, Japan*

[4] *Preeminent Medical Photonics Education and Research Center, Hamamatsu University School of Medicine, Handayama 1-20-1, Higashi-ku, Hamamatsu, Shizuoka 431-3192, Japan*

【Author Guidelines】

Short Review: Photochemical Reaction of Ketoprofen

Wataru Kashihara and Tadashi Suzuki*

*Department of Chemistry and Biological Science, Aoyama Gakuin University,
5-10-1 Fuchinobe, Chuo-ku, Sagamihara, Kanagawa 252-5258, Japan*

*Corresponding author:

Department of Chemistry and Biological Science, Aoyama Gakuin University, 5-10-1 Fuchinobe, Chuo-ku, Sagamihara, Kanagawa 252-5258, Japan
TEL: +81-042-759-6232
FAX: +81-042-759-6415
E-mail: suzuki@chem.aoyama.ac.jp

ABSTRACT

Photochemistry of ketoprofen (KP), one of the most popular nonsteroidal anti-inflammatory drugs (NSAIDs), has been intensively studied to understand drug-induced photosensitivity, which is known as a serious adverse effect. In this article, the photochemical reaction of KP recently reported by experimental and computational methods, was reviewed.

Key words: ketoprofen, nonsteroidal anti-inflammatory drugs, drug-induced photosensitivity, transient absorption spectroscopy, transient grating method

1. Drug-induced photosensitivity of KP

Nonsteroidal anti-inflammatory drugs (NSAIDs) have been used in the medical treatment for reducing fever and minor pain. However, drug-induced photosensitivity, which is classified under the phototoxic and photoallergic types, has been reported as an adverse effect. [1-4] Ketoprofen (2−(3−benzoylphenyl)propionic acid, KP), one of the most widely used NSAIDs, is clinically well known to induce the photoallergic type of drug-induced photosensitivity. [5-8] There are two major theories for formation of allergens; prohapten and photohapten theories. In the prohapten theory, a drug takes place photoreaction by UV irradiation to form a hapten, which binds to proteins. In the photohapten theory, a drug is docked into a protein, and a covalent bond is formed between the drug and a protein by UV light irradiation, leading to production of an allergen. It has been reported that KP *in vivo* produces an allergen by UV irradiation with the photohapten theory. [9-11] In this review, our recent works for the photochemistry of KP by transient absorption spectroscopy and transient grating method coupled with theoretical calculations are summarized.

2. Photochemical reaction of KP

The photochemistry of KP has been extensively studied to understand drug-induced photosensitivity. Fig. 1 shows the scheme of the photochemical reaction of KP, proposed from results of the study by the product analysis, [12,13] nano- or pico-second transient absorption spectroscopy, [14-23] time-resolved Raman spectroscopy, [24-27] time-resolved laser-induced optoacoustic spectroscopy, [28]

and quantum chemical calculations. [29-31] KP is weak acid (pK_a = 4.7) and forms an acid-base equilibrium with the deprotonated KP (KP−). The excited triplet KP, [3]KP*, produces through intersystem crossing from [1]KP* by UV irradiation. The [3]KP* abstracts a hydrogen atom from a surrounding molecule to yield a KP ketyl radical (KPH) and a counter radical. On the other hand, in the neutral or basic solution, the carboxylate anion of KP (KP−) with the UV irradiation yielded a carbanion through the decarboxylation to form a 3-ethylbenzophenone ketyl biradical (3-EBPH) or 3-ethylbenzophenone (3-EBP) by a proton transfer from a surrounding molecule.

3. Photochemical reaction of KP with triethylamine

The photochemistry of KP with and without triethylamine (TEA) in methanol was investigated by transient absorption spectroscopy and transient grating method. [21,32] The acid-base equilibrium between KP and TEA was found to be formed: KP + TEA ⇄ KP− + TEAH+. Here, TEAH+ is protonated TEA. From transient absorption spectra, it was found that the excitation of KP− rapidly produces the carbanion through decarboxylation reaction following the carbanion takes place a proton abstraction from TEAH+ to produce 3-EBPH. Furthermore, 3-EBPH was found to make a 1:1 complex with TEA. These results imply that an amino group in a protein should have important role for initial photoreaction of KP. [21]

Since the diffusion process of transient species should be related to reactivity, information on the translational diffusion dynamics in photoreaction of KP is essential

for understanding the photoreaction of KP with various biomolecules *in vivo*. The diffusion coefficients for photochemical species in methanol with and without TEA were obtained by transient grating method. The diffusion coefficients for the KPH, the carboxylate anion, and the EBPH···TEA complex were obtained to be $(6.9 \pm 0.1) \times 10^{-10}$ m^2 s^{-1}, $(8.1 \pm 0.1) \times 10^{-10}$ m^2 s^{-1}, and $(5.6 \pm 0.2) \times 10^{-10}$ m^2 s^{-1}, respectively. It was found these values are smaller than that for neutral KP obtained to be $(9.8 \pm 0.2) \times 10^{-10}$ m^2 s^{-1}. The contribution of slow diffusion for these species would be due to larger molecular volume and/or a specific attractive interaction with solvent. [32] Nishiyama *et al*. recently reported photochemical reaction of KP$^-$ in aqueous solutions at neutral pH investigated by transient grating method. The aggregation dynamics of 3-EBP was observed and it was driven in water-rich solutions. [33]

Photochemistry and diffusion dynamics of KP in biosystem will be probed by transient grating coupled with the transient absorption spectroscopy.

4. Photochemical reaction of KP with indoles

The photoreaction of neutral KP with indole and 3-methylindole, which are a side chain of the Trp residue, in acetonitrile were intensively studied by transient absorption spectroscopy. The reaction rate constants of the hydrogen atom abstraction rate constants of ^{3}KP* by indole and 3-methylindole were obtained to be $(1.4 \pm 0.1) \times 10^9$ M^{-1} s^{-1} and $(3.7 \pm 0.1) \times 10^9$ M^{-1} s^{-1}, respectively. The value for 3-methylindole was larger than that for indole. The transient absorption spectra of KP and 3-methylindole at 4 μs after the laser included the absorption bands of KPH and an indolyl radical. In addition, the absorption band in the transient spectra was observed at around 350 nm, assigned to the corresponding C-centered radical with quantum chemical calculations. These results indicate that ^{3}KP* abstracts a hydrogen atom in the methyl group
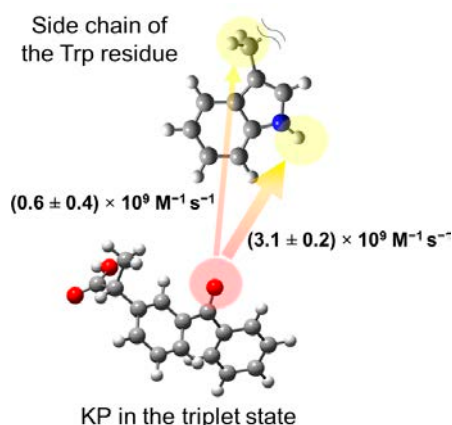
Fig. 2. The hydrogen atom abstraction and its rate constants of KP in the triplet state with 3-methylindole, which is a side chain of the Trp residue.

as well as that of N–H in the indole frame, producing an indolyl or a C-centered radical (Fig. 2). From the peaks of transient absorption spectra for indole radicals, the formation rate constants by 3-methylindole producing the indolyl and the C-centered radicals were estimated to be $(3.1 \pm 0.2) \times 10^9$ M^{-1} s^{-1} and $(0.6 \pm 0.4) \times 10^9$ M^{-1} s^{-1}, respectively. [22]

5. Photochemical reaction of KP with proteinogenic amino acids

The photochemical reaction of KP with twenty kinds of proteinogenic amino acids in phosphate buffer solution at pH 7.4 was intensively studied by transient absorption spectroscopy. The amino acids were classified into three groups on the reactivity. Three kinds of amino acids (His, Trp, and Tyr) were found excessively to accelerate the proton transfer reaction producing 3-EBPH from the
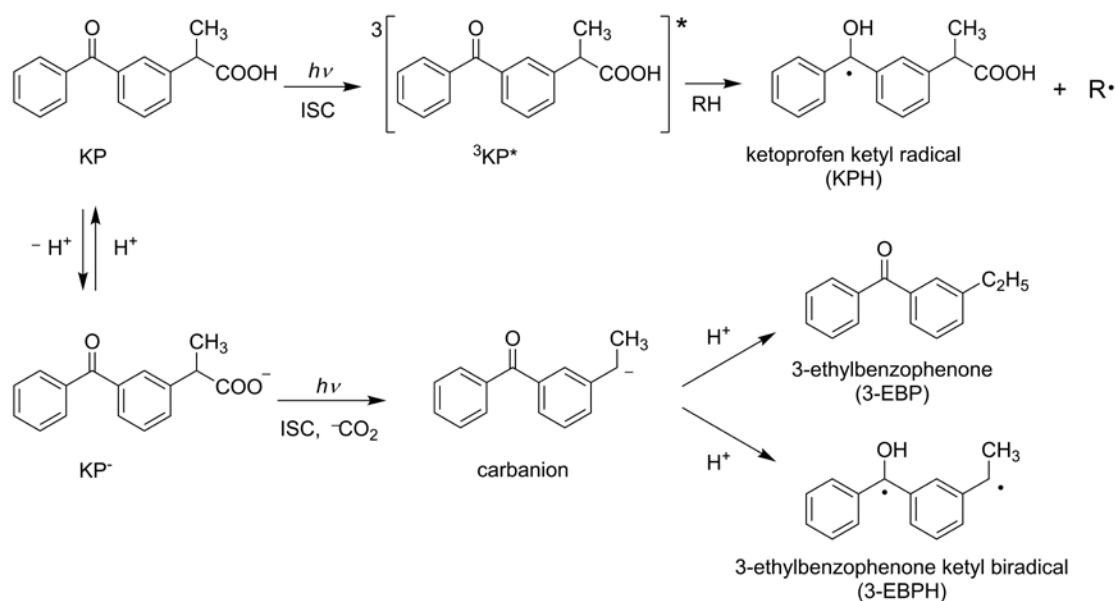
Fig. 1. Reaction scheme of KP and its carboxylate anion (KP$^-$) with UV irradiation.

Table 1. Reaction rate constants to form 3-EBPH by amino acids.

Amino acids [a]	Reaction rate constants to form 3-EBPH / 10^9 M^{-1} s^{-1}	Ref.
His	4.6	19
Trp	2.7	20
Tyr	0.78	20
Cys	0.32 ± 0.01	23
Asn	0.16 ± 0.01	23
Arg	0.15 ± 0.01, 0.13	23,19
Lys	0.14 ± 0.01, 0.12	23,19
Met	0.13 ± 0.01	23
Gln	0.13 ± 0.01	23
Phe	0.13 ± 0.01	23
Thr	0.10 ± 0.01	23
Ser	0.07 ± 0.01	23

[a] His: histidine, Trp: tryptophan, Tyr: tyrosine, Cys: cysteine, Asn: asparagine, Arg: arginine, Lys: lysine, Met: methionine, Gln: glutamine, Phe: phenylalanine, Thr: threonine, Ser: serine.

carbanion (Table 1). It was concluded that the reactivity of the carbanion with the amino acids strongly depends on the pK_a value of the amino acid side chains. [23]

To understand the photochemistry of KP⁻ in a protein, the structures of the complexes for KP⁻ docked in human serum albumin (HSA) were investigated. [23,34-39] It was found that Tyr411 and Arg410, which are the amino acid residues having high reactivity with the carbanion, would locate in the vicinity of KP⁻ in the binding site II on HSA by molecular mechanics and molecular dynamics calculations (Fig. 3). The main initial process for drug-induced photosensitivity by KP docked in the binding site II of HSA was discussed. [23] The proton transfer reaction with Tyr411 or Arg410 in HSA would yield 3-EBPH from the carbanion, produced through a photodecarboxylation reaction of KP⁻. The covalent bond between 3-EBPH and HSA would be formed finally to generate an allergen. We can examine the initial processes of photochemistry in the other proteins by performing the docking simulation of complexes for KP with these proteins. This approach can be applied to many other NSAIDs causing drug-induced photosensitivity.

6. Conclusion

In this review, photochemistry of KP reported by experimental and computational methods was summarized. The photochemical reaction of KP docked in a protein should lead to generation of allergen. Thus, the photochemical reaction of KP with the side chain of amino acids should be a key for understanding of the initial reaction process for drug-induced photosensitivity. The approach will be effective to clarify drug-induced photosensitivity caused by other NSAIDs as well as KP.
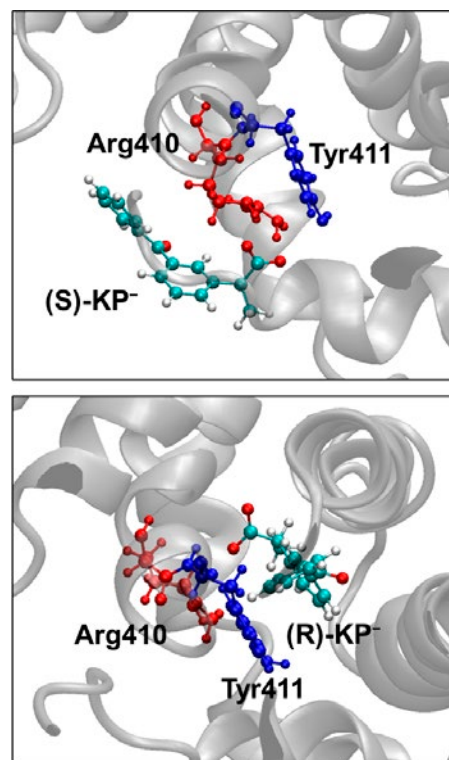
Fig. 3. The global minimum structures for the complexes of (S)-KP⁻ (top) and (R)- KP⁻ (bottom) docked in HSA.

REFERENCES

1. Boscá F, Miranda M A. Photosensitizing drugs containing the benzophenone chromophore. J Photochem Photobiol B, 1998; 43: 1-26.
2. Boscá F, Marin M L, Miranda M A. Photoreactivity of the Nonsteroidal Anti-inflammatory 2-Arylpropionic Acids with Photosensitizing Side Effects. Photochem Photobiol, 2001; 74: 637-655.
3. Gouda A A, El-Sayed M I K, Amin A S, El Sheikh R, Spectrophotometric and spectrofluorometric methods for the determination of non-steroidal anti-inflammatory drugs: A review. Arab J Chem, 2013; 6: 145-163.
4. Monteiro A F, Rato M, Martins C, Drug-induced photosensitivity: Photoallergic and phototoxic reactions. Clin Dermatol, 2016; 34: 571-581.
5. Bagheri H, Lhiaubet V, Montastruc J L, Chouini-Lalanne N. Photosensitivity to ketoprofen - Mechanisms and pharmacoepidemiological data. Drug Saf, 2000; 22: 339-349.
6. Le Coz C J, Bottlaender A, Scrivener J N, Santinelli F, Cribier B J, Heid E, Grosshans E M. Photocontact dermatitis from ketoprofen and tiaprofenic acid: cross-reactivity study in 12 consecutive patients. Contact Dermatitis, 1998; 38: 245-252.
7. Matsushita T, Kamide R. Five cases of photocontact dermatitis due to topical ketoprofen: photopatch testing and cross-reaction study. Photodermatol Photoimmunol Photomed, 2001; 17: 26-31.

8. Devleeschouwer V, Roelandts R, Garmyn M, Goossens A. Allergic and photoallergic contact dermatitis from ketoprofen: results of (photo) patch testing and follow-up of 42 patients. Contact Dermatitis, 2008; 58:159-166.

9. Imai S, Atarashi K, Ikesue K, Akiyama K, Tokura Y. Establishment of murine model of allergic photocontact dermatitis to ketoprofen and characterization of pathogenic T cells. J Dermatol Sci, 2006; 41: 127-136.

10. Atarashi K, Kabashima K, Akiyama K, Tokura Y. Stimulation of Langerhans cells with ketoprofen plus UVA in murine photocontact dermatitis to ketoprofen. J Dermatol Sci, 2007; 47: 151-159.

11. Atarashi K, Takano M, Kato S, Kuma H, Nakanishi M, Tokura Y. Addition of UVA–Absorber Butyl Methoxy Dibenzoylmethane to Topical Ketoprofen Formulation Reduces Ketoprofen–Photoallergic Reaction. J Photochem Photobiol B, 2012; 113: 56-62.

12. Costanzo L L, Guidi G D, Condorelli G, Cambria A, Fama M. Molecular Mechanism of Drug Photosensitization-II. Photohemolysis Sensitized by Ketoprofen. Photochem Photobiol, 1989; 50: 356-365.

13. Boscá F, Miranda M A, Carganico G, Mauleon D. Photochemical and Photobiological Properties of Ketoprofen Associated with the Benzophenone Chromophore. Photochem Photobiol, 1994; 60: 96-101.

14. Martinez L J, Scaiano J C. Transient Intermediates in the Laser Flash Photolysis of Ketoprofen in Aqueous Solutions: Unusual Photochemistry for the Benzophenone Chromophore. J Am Chem Soc, 1997; 119: 11066-11070.

15. Cosa G, Martinez J, Scaiano J C. Influence of solvent polarity and base concentration on the photochemistry of ketoprofen: independent singlet and triplet pathways. Phys Chem Chem Phys, 1999; 1: 3533-3537.

16. Monti S, Sortino S, Guidi G D, Marconi G. Photochemistry of 2-(3-benzoylphenyl)propionic acid (ketoprofen): Part 1 A picosecond and nanosecond time resolved study in aqueous solution. J Chem Soc Faraday Trans, 1997; 93: 2269-2275.

17. Suzuki T, Okita T, Osanai Y, Ichimura T. Reaction Dynamics of Excited 2-(3-Benzoylphenyl)propionic Acid (Ketoprofen) with Histidine. J Phys Chem B, 2008; 112: 15212-15216.

18. Suzuki T, Osanai Y, Isozaki T. Effect of Basic Amino Acids on Photoreaction of Ketoprofen in Phosphate Buffer Solution. Photochem Photobiol, 2012; 88: 884-888.

19. Suzuki T, Shinoda M, Osanai Y, Isozaki T. Photochemical Reaction of 2-(3-Benzoylphenyl) propionic Acid (ketoprofen) with Basic Amino Acids and Dipeptides. J Phys Chem B, 2013; 117: 9662-9668.

20. Shinoda M, Isozaki T, Suzuki T. Photoreaction of Ketoprofen with Tryptophan and Tyrosine in Phosphate Buffer Solution. Photochem Photobiol, 2014; 90: 92-98.

21. Suzuki H, Suzuki T, Ichimura T, Ikesue K, Sakai M. Reaction Dynamics of Excited Ketoprofen with Triethylamine. J Phys Chem B, 2007; 111: 3062-3068.

22. Kashihara W, Inoue M, Tanabe S, Miyata S, Sakai K, Isozaki T, Suzuki T. Hydrogen Abstraction of Ketoprofen in the Excited Triplet State with Indole and Methylindoles. J Phys Chem B, 2019; 123: 9388-9394.

23. Kashihara W, Shinoda M, Tsuchiya K, Isozaki T, Mijiddorj B, Ueda K, Suzuki T. Photochemical Reaction of Ketoprofen with Proteinogenic Amino Acids. J Phys Chem B, 2022; 126: 2098-2107.

24. Chuang Y P, Xue J, Du Y, Li M, An H Y, Phillips D. L. Time-Resolved Resonance Raman and Density Functional Theory Investigation of the Photochemistry of (S)-Ketoprofen. J Phys Chem B, 2009; 113: 10530-10539.

25. Li M D, Du Y, Chuang Y. P, Xue J, Phillips D L. Water concentration dependent photochemistry of ketoprofen in aqueous solutions. Phys Chem Chem Phys, 2010; 12: 4800-4808.

26. Li M D, Yeung C S, Guan X, Ma J, Li W, Ma C, Phillips D L. Water- and Acid-Mediated Excited-State Intramolecular Proton Transfer and Decarboxylation Reactions of Ketoprofen in Water-Rich and Acidic Aqueous Solutions. Chem Eur J, 2011; 17: 10935-10950

27. Li M D, Ma J, Su T, Liu M, Yu L, Phillips D L. Direct Observation of Triplet State Mediated Decarboxylation of the Neutral and Anion Forms of Ketoprofen in Water-Rich, Acidic, and PBS Solutions. J Phys Chem B, 2012; 116: 5882-5887.

28. Borsarelli C D, Braslavsky S E, Sortino S, Marconi G, Monti S. Photodecarboxylation of Ketoprofen in Aqueous Solution: A Time-resolved Laser-induced Optoacoustic Study. Photochem Photobiol, 2000; 72: 163-171.

29. Lhiaubet V, Gutierrez F, Penaud-Berruyer F, Amouyal E, Daudey J P, Poteau R, Chouini-Lalanne N, Paillous N. Spectroscopic and theoretical studies of the excited states of fenofibric acid and ketoprofen in relation with their photosensitizing properties. New J Chem, 2000; 24: 403-410.

30. Musa K A K, Matxain J M, Eriksson L A. Mechanism of photoinduced decomposition of ketoprofen. J Med Chem, 2007; 50: 1735-1743.

31. Bignon E, Marazzi M, Besancenot V, Gattuso H, Drouot G, Morell C, Eriksson L A, Grandemange S, Dumont E, Monari A. Ibuprofen and ketoprofen potentiate UVA-induced cell death by a photosensitization process. Sci Rep, 2017; 7: 8885.

32. Kashihara W, Takeyama J, Suzuki T. Diffusion process in photoreaction of ketoprofen probed by transient grating method. J Photochem Photobiol A, 2020; 399:

112623.

33. Nishiyama Y, Nagatani H. Molecular diffusion and aggregate formation of photoproducts from ketoprofen in aqueous solutions. Chem Phys Lett, 2022; 795: 139511.

34. Rahman M H, Yamasaki K, Shin Y H, Lin C C, Otagiri M. Characterization of High Affinity Binding Sites of Non-steroidal Anti-inflammatory Drugs with Respect to Site-Specific Probes on Human Serum Albumin. Biol Pharm Bull, 1993; 16: 1169-1174.

35. Chuang V T G, Kuniyasu A, Nakayama H, Matsushita Y, Hirono S, Otagiri M. Helix 6 of subdomain III A of human serum albumin is the region primarily photolabeled by ketoprofen, an arylpropionic acid NSAID containing a benzophenone moiety. Biochim Biophys Acta, 1999; 1434: 18-30.

36. Watanabe H, Tanase S, Nakajou K, Maruyama T, Kragh-Hansen. U, Otagiri M. Role of Arg-410 and Tyr-411 in human serum albumin for ligand binding and esterase-like activity. Biochem J, 2000; 349: 813-819.

37. Monti S, Manet I, Manoli F, Sortino S. Binding and photochemistry of enantiomeric 2-(3-benzoylphenyl) propionic acid (ketoprofen) in the human serum albumin environment. Photochem Photobiol Sci, 2007; 6: 462-470.

38. Monti S, Ottani S, Manoli F, Manet I, Scagnolari F, Zambelli B, Marcini G. Chiral Recognition of 2-(3-Benzoylphenyl)propionic Acid (Ketoprofen) by Serum Albumin: An Investigation with Microcalorimetry, Circular Dichromism and Molecular Modeling. Phys Chem Chem Phys, 2009; 11: 9104-9113.

39. Monti S, Manet I. Supramolecular Photochemistry of Drugs in Biomolecular Environments. Chem Soc Rev, 2014; 43: 4051-4067.

Clinical, Genetic, and Epidemiological Findings of Erythropoietic Protoporphyria in Japan

Megumi Mizawa[1)*], Hiroshi Hara[2)], Teruhiko Makino[1)], Tadamichi Shimizu[1)]

1) Department of Dermatology, Faculty of Medicine, Academic Assembly, University of Toyama, Toyama, Japan
2) Department of Dermatology, Nigata Prefectural Central Hospital, Joetsu, Japan

*Corresponding author:
Megumi Mizawa, M.D., Ph.D.
Department of Dermatology, Faculty of Medicine, Academic Assembly, University of Toyama,
Sugitani, Toyama 930-0194, Japan.
Tel: +81-76-434-7305; Fax: +81-76-434-5028
E-mail: megumiza@med.u-toyama.ac.jp

ABSTRACT

Erythropoietic protoporphyria (EPP) is a rare autosomal dominant disorder of heme biosynthesis, and results from a partial decrease in ferrochelatase activity leading to the excess accumulation of protoporphyrin. In typical EPP, photosensitivity usually initially appears after the first exposure to the sun in early infancy or childhood. In addition to phototoxic episodes, these disorders have multisystemic manifestations, including hepatopathy and anemia. Physicians occasionally experience Japanese EPP patients with mild symptoms and no *FECH* gene mutations. Patients who are homozygous for the c.315-48T>C polymorphism may develop a mild phenotype of EPP via a slight increase in protoporphyrin. We reviewed 10 reported EPP patients who were homozygous for the c.315-48T>C polymorphism and had no *FECH* gene mutation. The frequency of the homozygous c.315-48T>C polymorphism in the Japanese population is higher than that observed in European countries. Therefore, there may be more patients with a mild phenotype of EPP who have not been diagnosed in Japan. Erythropoietic protoporphyria has been reported worldwide, but there is regional variation in its epidemiology. To examine the characteristics of EPP in the Japanese population, we reviewed 127 Japanese EPP cases reported from 1980 to 2022 that were identified using Ichushi-Web. The median age of these Japanese EPP patients at onset was 6 years. Approximately 20% of Japanese patients are recognized to have symptoms of erythropoietic protoporphyria after 10 years of age. Japanese erythropoietic protoporphyria shows a characteristic phenotype of late onset and mild symptoms in comparison to Caucasian erythropoietic protoporphyria. This review describes the characteristics of erythropoietic protoporphyria in Japanese patients.

Keywords: erythropoietic protoporphyria, ferrochelatase, photosensitivity

1. Introduction

Erythropoietic protoporphyria (EPP; OMIM #177000) results from pathogenic variants in the *ferrochelatase* (*FECH*) gene, which encodes an enzyme that catalyzes iron insertion into protoporphyrin (PP) to form heme. We reviewed the clinical, genetic, and epidemiological findings of EPP patients in the Japanese population.

2. Clinical and laboratory findings of typical EPP

EPP presents in early childhood with severe, nonblistering phototoxicity preceded by characteristic prodromal symptoms, often including tingling, burning, or itching. Continued exposure leads to severe phototoxic pain that can be associated with erythema and swelling of sun-exposed skin, primarily the dorsum of the hands and face. In addition to phototoxic episodes, these disorders have multisystemic manifestations including hepatopathy, iron deficiency anemia, and vitamin D deficiency. Partial deficiency in FECH activity results in the accumulation of PP in the skin, blood cells, and skin blood vessels. The accumulation of phototoxic PP in superficial vessels is activated by blue light (400–410 nm), triggering singlet oxygen free-radical reactions that lead to severe neuropathic pain that lasts for hours to days. PP is released from erythroid cells into the circulation, gains access to the vascular endothelium and liver, and is excreted through the biliary system. Laboratory investigations have revealed increased PP concentrations. A large number of fluorocytes were observed in the peripheral blood (Fig. 1A). The characteristics of photosensitivity in EPP are first a burning, stinging sensation appearing immediately upon sun exposure, followed by erythema, edema, and petechiae (1-3). Repeated sun exposure can lead to more chronic skin changes, such as circular or linear scarring and waxy thickening (1, 3). PP is cleared by the hepatobiliary system and has a concentration-dependent hepatotoxic effect; as such, its accumulation in the liver can impair the
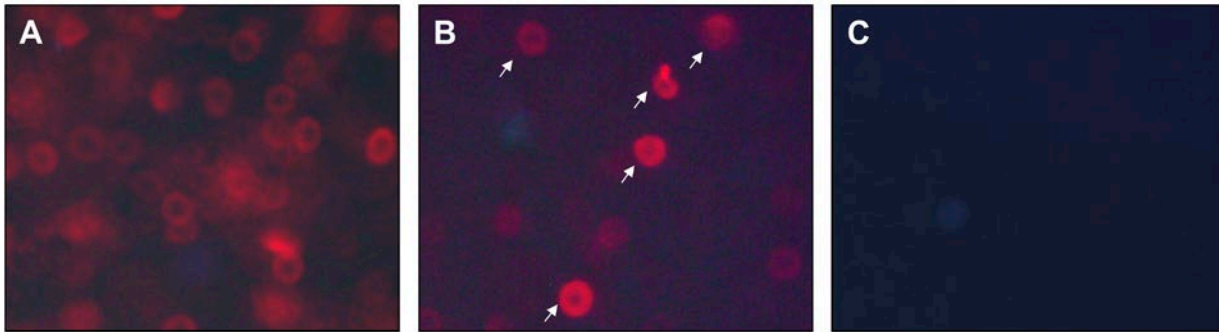
Fig. 1. Fluorocytes. A. Fluorocytes in a typical EPP patient. B. Only a few fluorocytes were observed in the peripheral blood of an incomplete EPP patient (white arrow). C. No fluorocytes were observed in control subjects.

hepatobiliary system in <10% of patients and potentially lead to liver failure (4-6). Mild hypochromic microcytic anemia may also develop (7).

3. Genetic findings of EPP and other porphyrias

The phenotypic expression of protoporphyria occurs due to decreased activity of FECH or increased activity of aminolevulinic acid synthase (ALAS) in red blood cells. EPP is an autosomal-dominant inherited disorder. More than 200 different mutations of the *FECH* gene have been reported (8). However, EPP has low clinical penetrance, with <10% of mutation carriers developing overt clinical symptoms (9). Gouya et al. (10-12) revealed that the intronic single nucleotide polymorphism (SNP) (rs: 2272783) of C at c.315-48 *in trans* to a mutated *FECH* gene allele results in the development of the EPP phenotype via the low expression of FECH. Although approximately 4% of EPP patients have two rare pathogenic *FECH* gene variants, approximately 96% of EPP patients have a rare pathogenic *FECH* gene variant *in trans* of a common intronic *FECH* gene variant c.315-48T>C (rs2272783, historically called IVS3-48T>C), which is known to increase the use of an aberrant splice site. Some SNPs in the coding region of the *FECH* gene have been reported. It has been shown that the c.68–23C>T variant (rs: 2269219) causes exon skipping (13). In addition, the functional significance of c.1-251A>G (rs: 17063905) on the transcriptional activity of the *FECH* gene lies in decreasing promoter activity (14). Recently, a novel deep intronic variant c.464–1169 A>C (p.Ala155ValfsTer22) located in intron 4 was also reported (8).

In a few cases, the accumulation of PP has been reported to be a consequence of a gain-of-function mutation in an erythroid variant of the *delta-aminolaevulinate synthase 2* (*ALAS2*) gene, the first enzyme of erythroid heme biosynthesis (X-linked erythropoietic protoporphyria, XLEPP; OMIM #300752) (15). More recently, an increase in the activity of ALAS2 protein has been reported to result from a point mutation in the *caseinolytic mitochondrial matrix peptidase chaperone subunit* (*CLPX*) gene, which encodes a regulatory protein responsible for the activation of ALAS2 (EPP2; OMIM #618015) (16, 17). Although EPP usually presents at childhood, adult-

onset cases secondary to hematological disease (usually myelodysplastic syndrome) have rarely been reported. It has been reported that most cases of EPP with MDS have an abnormality in chromosome 18, which encodes the *FECH* gene. An abnormal chromosome 18, possibly deletion of the *FECH* gene, in clones of myelocytes and peripheral blood cells induces EPP (18, 19).

4. Homozygous c.315-48T>C polymorphism may cause EPP with a mild phenotype

We previously reported that the homozygous c.315-48T>C polymorphism develops a mild phenotype of EPP via a slight increase in PP. We referred to this condition as incomplete EPP. There have been 10 reported EPP patients with both homozygous c.315-48T>C polymorphism and no *FECH* gene mutation (Table 1). Schneider-Yin et al. also reported an Ashkenazi Jewish patient with homozygous c.315-48T>C polymorphism and no *FECH* gene mutation, who showed both clinical and biochemical indications of a mild phenotype of EPP (no.5) (20). Saruwatari et al. reported an EPP patient with 3 SNPs, homozygous c.315-48T>C polymorphism and no *FECH* gene mutation; those SNPs did not affect the mRNA structure (no. 4) (21). Another 5 EPP patients (nos. 6-10) showed classical clinical features. In addition, Suzuki et al. reported a case of late-onset EPP associated with MDS that was suspected to have been caused by homozygous c.315-48T>C polymorphism in the *FECH* gene allele. No deletion or mutation in the *FECH* gene was detected in this patient (19). In contrast, six noncarriers of the *FECH* gene mutation who were homozygous for the c.1-251A>G, c.68-23C>T, and c.315-48T>C variants did not show biochemical or clinical symptoms of the disease (10).

The FECH activity in EPP patients has been reported to be decreased in comparison to normal subjects, although the values are variable, ranging widely from 8% to 45% (4, 22). Tahara et al. examined FECH activity in subjects with no *FECH* gene mutations. Consequently, the FECH activity in subjects with homozygous and heterozygous c.315-48T>C polymorphism was 38% and 50–60%, respectively, of that observed in patients with homozygous c.315-48T polymorphism (23). Interestingly, in their analysis of the percentage of aberrantly inserted FECH mRNA in patients

with nonclassical EPP (with homozygous c.315-48T>C and no *FECH* gene mutation), Brancaleoni et al. (24) found that the levels were comparable to those in classical EPP patients (with c.315-48T>C and the *FECH* gene mutation). Furthermore, the expression of the *FECH* gene in nonclassical EPP was comparable to that in classical EPP patients (24). Two other variants in the *FECH* gene (c.1–252A > G and c.68–23C > T) have been found to be associated with the intron 3 variant (13, 14). However, the presence of the G base at position c.1–252 and the T base at position c.68–23 did not seem to influence the total expression of the *FECH* gene (24). Therefore, the homozygous c.315-48T>C polymorphism was identified as pathological. These findings support the hypothesis that the slight decrease in FECH activity is caused by the homozygous c.315-48T>C polymorphism, resulting in a mild clinical appearance of EPP. In previous studies, it was speculated that the genotypic frequency of the splice site modulator c.315-48T>C may affect the penetrance of the EPP phenotype in affected families as well as the prevalence of the disease in a population. However, a recent study reported that the c.464–1169 A>C intronic

substitution (p. Ala155ValfsTer22) disrupts an exonic splicing silencer site, causing the insertion of a "cryptic exon" containing a stop codon in the mature *FECH* gene transcript (8). Further studies are required to clarify the variability in the clinical manifestations of EPP.

The frequency of the homozygous c.315-48T>C polymorphism in the Japanese population is >10 times that in individuals from European countries (25). Therefore, there may be more patients with incomplete EPP who have not been diagnosed in Japan. Furthermore, this may explain the late age of onset in Japanese EPP patients, which we mentioned in the next chapter. Indeed, three Japanese incomplete EPP patients developed their disease at 5–6 years of age (Table 1: nos. 1-3) (26). Of the 127 Japanese EPP patients we mentioned in the next chapter, 8 had mild photosensitivity and showed a slight increase in their PP levels (<400 μg/dl). Their median age of onset was 3 years (range: 1–15 years), and their median age at diagnosis was 15 years (range: 1–45 years). However, those patients did not undergo genetic analyses, so the precise details of their condition remain unclear. Nevertheless, we speculate that some or all of them may

Table 1. EPP patients with homozygous c.315-48T>C polymorphism and no *FECH* gene mutation

Reference	Country	No	Patient	PP levels	Clinical symptoms	FECH gene mutation	IVS3-48
Mizawa et al.[26]	Japan	1	6-year-old female	115 (normal range; 30-86 μg/dl)	mild photosensitivity	Wt/Wt	C/C
		2	7-year-old female	103 (normal range; 30-86 μg/dl)	mild photosensitivity	Wt/Wt	C/C
		3	9-year-old male	122 (normal range; 30-86 μg/dl)	mild photosensitivity	Wt/Wt	C/C
Saruwatari H et al.[21]	Japan	4	16-year-old male	3668 (normal range; 30-86 μg/dl)	photosensitivity	3 SNPs*	C/C
Schneider-Yin et al.[20]	Israel	5	58-year-old male	338 (normal range; <80 μg/dl RBC)	mild photosensitivity	Wt/Wt	C/C
Whatley et al.[63]	United Kingdom	6	ND	18.2 (μmol L^{-1})	Typical EPP	Wt/Wt	C/C
Brancaleoni V et al.[22]	Italy	7	ND	100 μg/gHb (normal range; 3.0 μg/gHb)	Typical EPP	Wt/Wt	C/C
		8	ND	15 μg/gHb (normal range; 3.0 μg/gHb)	Typical EPP	Wt/Wt	C/C
		9	ND	32.2 μg/gHb (normal range; 3.0 μg/gHb)	Typical EPP	Wt/Wt	C/C
		10	ND	33 μg/gHb (normal range; 3.0 μg/gHb)	Typical EPP	Wt/Wt	C/C

* The three single nucleotide polymorphisms (SNPs) are A316G, G827C and G950A; they did not affect the mRNA structure.

have incomplete EPP.

5. The clinical features and course of Japanese EPP with a mild phenotype

We previously reported three Japanese patients with a mild phenotype of EPP (Table 1: nos. 1-3). They had mild photosensitivity associated with a slight increase in the PP concentration and the formation of a small number of fluorocytes (Fig. 1B). The *FECH* gene mutation was not detected by direct sequencing analyses in any of the patients. However, all patients had homozygous c.315-48T>C polymorphism (26). The three abovementioned Japanese incomplete EPP patients (patient nos. 1-3) were advised to avoid exposure to sunlight. They were followed up for their clinical symptoms and PP levels every year for 5–10 years. Their PP levels have also slightly increased over time. Patient no. 3 occasionally suffered from slight painful photosensitivity in the summer. Nevertheless, in patient nos. 1-3, the frequency and severity of photosensitivity gradually decreased with age, although they were unable to avoid sun exposure completely and sometimes developed mild sunburn. The PP level of patient no. 2 decreased to close to the normal limit. These findings suggest that the symptoms of incomplete EPP patients may improve with age. Careful follow-up of the PP levels of patients with incomplete EPP is needed.

A previous report found that 40% of EPP patients showed an improvement in their symptoms following a build-up of sunlight tolerance after repeated exposure (27). EPP patients seem to benefit from UV 'desensitization' therapy, and anecdotal evidence suggests that natural sunlight exposure improves light tolerance (28). Narrow-band UV-B therapy was reported to increase light protection via epidermal thickening and hyperpigmentation and to suppress the skin immune system in EPP patients with mild symptoms (29). Oral β-carotene (60–180 mg/day) seems to be effective for clearing singlet oxygen generated by the photochemical reaction of porphyrin (30) or in protecting the skin from sunlight by skin discoloration due to carotenemia (31). Afamelanotide, a potent α-melanocyte-stimulating hormone (α-MSH) analog, was recently approved as a treatment for EPP by the European Medicines Agency in 2014. Afamelanotide can darken the skin color and increase tolerance to sunlight exposure without pain (27, 28). Afamelanotide-induced eumelanin synthesis provided photoprotection and decreased the consequences of phototoxicity (32). Furthermore, a novel oral melanocortin 1 receptor agonist, dersimelagon, induces melanogenesis *in vitro* and *in vivo*, suggesting its potential application for the prevention of phototoxic reactions in patients with photodermatoses, such as EPP and XLEPP (33). Clinical trials of dersimelagon are currently underway. These findings support the hypothesis that increased epidermal melanin production and distribution caused by suntan reduces damaging UV and visible light penetration. Although the precise mechanism underlying the improvement of EPP symptoms remains unclear, we speculate that having a slight suntan can help to improve photosensitivity.

6. Epidemiology and clinical features of Japanese EPP patients

EPP is considered to occur across races and ethnic groups. However, we often experience a difference between Japanese patients and those from other countries regarding the epidemiology and clinical symptoms of EPP.

In a recent report from Italy, the minimum prevalence of EPP was reported to be 3.15 cases per million population, and the incidence was reported to be 0.13 cases per million population/year (34). This report mentioned that the incidence significantly increased after 2009 due to the availability of alfa-melanotide, which effectively limits skin photosensitivity. A prevalence of 1 per 180,000 population has been reported in Sweden (35), and a slightly higher prevalence has been reported in the European immigrant populations of South Africa (1/152,000) (36), the United Kingdom (1/143,000) (37), Northern Ireland (1/79,000) (38), and the Netherlands (1/75,000) (39). The exact prevalence of EPP in Japan has not been precisely determined. However, the penetrance of the EPP phenotype in the Japanese population is expected to be higher than that in Western countries due to the high frequency of the c.315-48T>C polymorphism (43%) (25). The reported frequency of the c.315-48T>C allele in different populations is as follows: Chinese (Han), 41% (40); Southeast Asians, 31%; French Caucasians, 6.4% (5); British, 13% (41); Ashkenazi Jews, 8% (20); Swiss, 7% (42); Czechs, 5.5% (43); Spanish, 5% (44); North Africans, 2.7%; West Africans, <1% (5); and Italians, 1% (45). Conversely, EPP is rare in West Africans because of the extremely low frequency of the c.315-48T>C polymorphism in West Africans (5, 25).

The initial clinical symptoms of EPP usually appear at the first exposure to the sun in early infancy or childhood. A previous review of 223 EPP cases in the United Kingdom demonstrated that the median age of onset was 1 year (range: 0–12 years) (37). In Sweden, the onset of symptoms most frequently occurred in the first year of life, and the median age was 3 years (range 0–25 years) (35). In North American patients with EPP, the mean age at the onset of symptoms was reported to be 4.1 (standard deviation 3.0) years (n=158) (46). To examine the characteristics of EPP in the Japanese population, we reviewed 127 Japanese EPP cases reported from 1980 to 2022, which were identified using Ichushi-Web (Table 2). Of the 78 papers reviewed, 68 were written in Japanese, and 10 were written in English (19, 21, 47-54). The median age at onset was 6 years (range: 1–37 years; n=84), including 2 patients with acquired EPP with myelodysplastic syndrome (Fig. 2). Surprisingly, approximately 20% of all patients were recognized as having symptoms of EPP after 10 years of age. We hypothesize that the onset of EPP in the Japanese
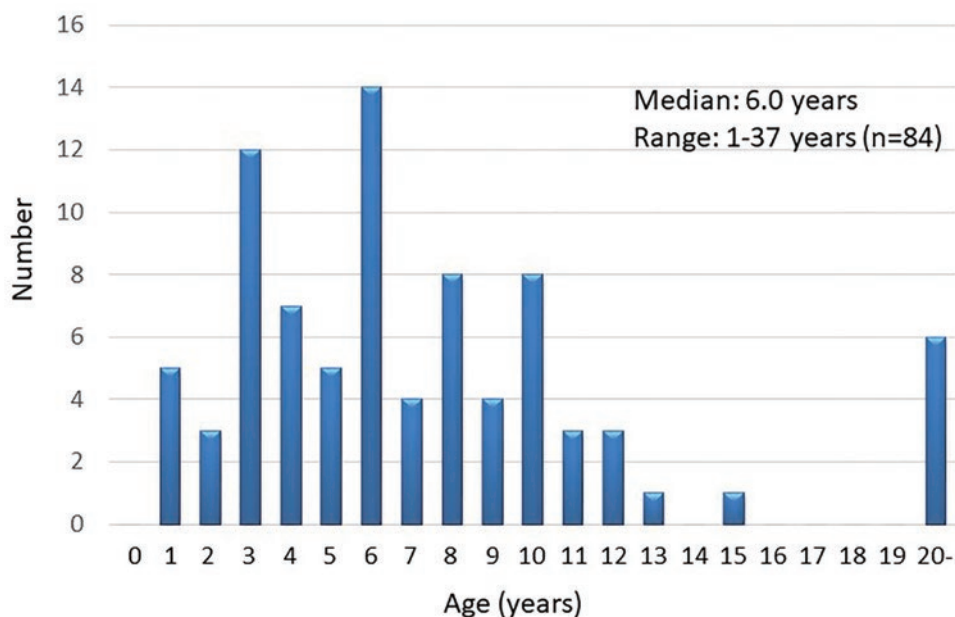
Fig. 2. The age at the onset of EPP symptoms of 84 patients reported in Japan from 1980 to 2022.
Of the 127 EPP patients, the data of 84 patients whose age of onset could be identified were included in the analysis.

Table 2. Summary of EPP in the Japanese population

Country	Japan

Number of patients
        males
        females
	127 patients
	89 (70%)
	38 (30%)

Race/ethnicity	Japanese : 126 patients (100%)
Age at onset	Median: 6.0 years (range: 0-37 years) (n=84)
Age at diagnosis	Median: 15.0 years (range: 1-60 years) (n=124) Only 24 patients (19.4%) diagnosed before 10 years of age.

Total erythrocyte porphyrin
 	
        males
        females
	Median 1931 µg/dl (n=120)
	range: 138.4-21809µg/dl
	(normal range: 30–86 µg/dl)
	
	Median: 1926 µg/dl (range: 159-21809) (n=83)
	Median: 1936 µg/dl (range: 138.4-13011) (n=37)
	There was no significant difference between male and female.

Liver disfunction	58 patients (50.9%)(n=114) 15 patients (13%) had protoporphyric liver failure. Among them, 2 patients died and 1 patient received a liver transplant. A total of 5 patients (4.4%) had gallstones. Patients with EPP-rerated liver dysfunction had significantly higher median PP levels than patients without EPP-related liver dysfunction ($P<0.001$). Patients with liver dysfunction: median: 3310 µg/dl (range: 159-21809) (n=54) Patients without liver dysfunction: median: 1141 µg/dl (range: 138.4-5250) (n=55)
Anemia	44 patients (47.8%) (n=92) There was no significant difference in PP levels between patients with and without anemia. Patients with anemia: median: 2101 µg/dl (range: 159-21809) (n=43) Patients without anemia: median: 2178 µg/dl (range: 138.4-13011) (n=47)

population is later than that in Caucasian populations.

The median age at diagnosis was reported to be 12 years in the United Kingdom (37), 22 years in Sweden (35), and 28 years in Italy (34). In Japan, the median age at diagnosis is 15 years, with only 24 patients (19.4%) diagnosed before 10 years of age. Similarly, it has been reported that only 12.2% of EPP patients are diagnosed before 10 years of age in Italy (34). Although patients are symptomatic in early childhood, there was a lag in the diagnosis, with many patients going undiagnosed or misdiagnosed for several years or even decades.

It was reported that male patients with EPP had significantly higher PP levels than female patients in the United Kingdom, Sweden and North America (35, 37, 46). However, among Japanese patients, there was no significant difference in the PP levels between males and females.

The incidence of cholelithiasis in EPP patients has been reported to be as high as 20% and can occur at a young age (9, 55). Conversely, hepatic failure is much less common. The incidence rates have been reported to range from 2% to 5% (9, 56). In Japanese population studies, 58 patients (50.9%; n=114) had liver dysfunction, including slight abnormalities in AST, ALT, ALP, and GGT levels, which were higher than previously reported (3, 21, 37). Fifteen patients (13%) had protoporphyric liver failure. Among them, two patients died, and one received a liver transplant. A total of 5 patients (4.4%) had gallstones. Among EPP patients, abnormal liver function test results were reported in 8% of patients in the United Kingdom (37), 25% of patients in Sweden (35) and 26.5% of patients

in North America (46). Patients with liver dysfunction had significantly higher median PP levels (median: 3310 μg/dl [range: 159-21809]; n=54) than patients without liver dysfunction (median: 1141 μg/dl [range: 138.4-5250]; n=55) (P<0.001). In addition, patients with severe liver dysfunction had significantly higher median PP levels (median: 8808 μg/dl [range: 1147-21809]; n=12) than patients with liver dysfunction (without severe) (median: 2398 μg/dl [range: 159-10225]; n=42) (P<0.001) (Fig. 3A). The percentage of liver dysfunction in Japanese EPP patients was found to be higher than that in other countries. However, the prevalence of liver dysfunction in other countries is the result of a cohort study. On the other hand, the percentage of liver dysfunction in Japanese patients was only determined based on a review of reported cases. Thus, the comparison of the data is associated with some limitations.

Microcytic anemia is estimated to be found in 20–60% of patients (57). It was reported to be detected in 21% of Swedish EPP patients (35) and 46.6% of North American EPP patients (46). Anemia was reported in 44 Japanese patients with EPP (47.8%; n=92). The PP levels of patients with and without anemia did not differ to a statistically significant extent (Fig. 3B).

There seem to be regional differences in the age at the onset EPP. The exact mechanism underlying the onset of EPP symptoms remains unclear. Interestingly, few published reports have included adult-onset EPP cases with the *FECH* gene mutation (41, 58). Late-onset EPP patients developed photosensitivity after strong sun exposure in a tropical climate in middle-age despite not experiencing
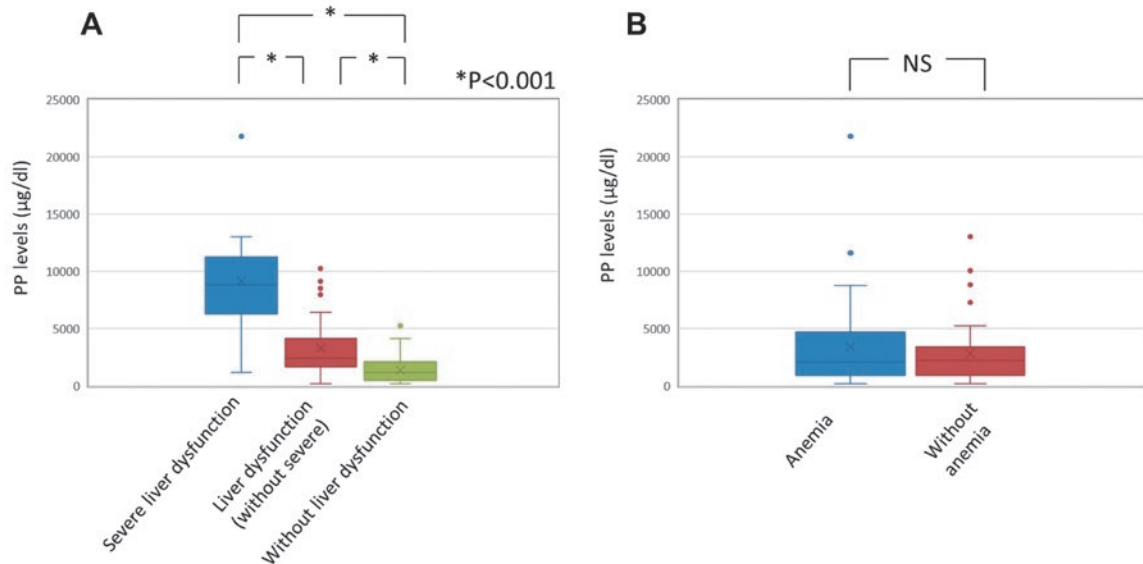

Fig. 3. A. Relationship between PP levels and liver dysfunction. In 109 of the 127 EPP patients, the presence or absence of liver dysfunction, its severity and PP levels could be identified. Their data were used for analysis (n=109). Patients with severe liver dysfunction had significantly higher median PP levels (median: 8808 μg/dl [range: 1147-21809]; n=12) than patients with liver dysfunction (without severe) (median: 2398 μg/dl [range: 159-10225]; n=42) (P<0.001).

Fig. 3. B. Relationship between PP levels and anemia. In 90 of the 127 EPP patients, the presence or absence of anemia and PP levels could be identified. Their data were used in the analysis (n=90). There was no significant difference in PP levels between patients with (median: 2101 μg/dl [range: 159-21809]; n=43) or without anemia (median: 2178 μg/dl [range: 138.4-13011]; n=47).

any symptoms in Northern Europe, where they were only exposed to weak sunlight (41, 58). We also encountered a case in which photosensitivity initially appeared at 13 years of age in a Japanese patient, although the patient had been found to have fluorocytes, an increased PP level and a *FECH* gene mutation when she was 7 years of age (59). In this Japanese patient, we speculate that avoiding sun exposure may have delayed the onset of EPP. Thus, the dose of sun exposure may play an important role in the induction of EPP symptoms.

We can propose several possible reasons for the late age of onset in Japanese EPP patients. First, most of the Japanese population tends to avoid strong sun exposure, as recommended by the Japanese Ministry of the Environment since 1998. Second, the melanin and carotene content in Japanese skin is greater than that in Caucasian skin (60-62). This greater amount of melanin and carotene imbues superior natural photoprotection (30, 60, 62). Finally, Japanese EPP patients include a proportion of incomplete EPP patients, who have a mild phenotype and whose symptoms may be less obvious in comparison to patients with typical EPP.

7. Conclusion

This review demonstrates the clinical appearance, genetic features and epidemiology of Japanese EPP patients. Japanese EPP shows a characteristic phenotype, including late onset and mild symptoms, in comparison to Caucasian EPP. This may be explained by the existence of incomplete EPP patients in Japan. Further studies are required to clarify the characteristics of Japanese EPP.

REFERENCES

1. Murphy GM. Diagnosis and management of the erythropoietic porphyrias. Dermatol Ther 2003; 16: 57-64.
2. Lecha M. Erythropoietic protoporphyria. Photodermatol Photoimmunol Photomed 2003; 19: 142-146.
3. Lim HW. Pathogenesis of photosensitivity in the cutaneous porphyrias. J Invest Dermatol 2005; 124: xvi-xvii.
4. Taketani S, Fujita H. The ferrochelatase gene structure and molecular defects associated with erythropoietic protoporphyria. J Bioenerg Biomembr 1995; 27: 231-238.
5. Gouya L, Martin-Schmitt C, Robreau AM, Austerlitz F, Da Silva V, Brun P, et al. Contribution of a common single-nucleotide polymorphism to the genetic predis-position for erythropoietic protoporphyria. Am J Hum Genet 2006; 78: 2-14.
6. Gross U, Hoffmann GF, Doss MO. Erythropoietic and hepatic porphyrias. J Inherit Metab Dis 2000; 23: 641-661.
7. Cox TM, Alexander GJ, Sarkany RP. Protoporphyria. Semin Liver Dis 1998; 18: 85-93.
8. Chiara M, Primon I, Tarantini L, Agnelli L, Brancaleoni V, Granata F, et al. Targeted resequencing of FECH locus reveals that a novel deep intronic pathogenic variant and eQTLs may cause erythropoietic protoporphyria (EPP) through a methylation-dependent mechanism. Genet Med 2020;22(1):35-43.
9. Schneider-Yin X, Gouya L, Meier-Weinand A, Deybach JC, Minder EI. New insights into the pathogenesis of erythropoietic protoporphyria and their impact on patient care. Eur J Pediatr 2000; 159: 719-725.
10. Colombo FP, Rossetti MV, Méndez M, Martínez JE, Enríquez de Salamanca R, del C Batlle AM, et al. Functional associations of genetic variants involved in the clinical manifestation of erythropoietic protoporphyria in the Argentinean population. J Eur Acad Dermatol Venereol 2013; 27: 754-762.
11. Gouya L, Puy H, Robreau AM, Bourgeois M, Lamoril J, Da Silva V, et al. The penetrance of dominant erythropoietic protoporphyria is modulated by expression of wildtype FECH. Nat Genet 2002; 30: 27-28.
12. Gouya L, Puy H, Lamoril J, Da Silva V, Grandchamp B, Nordmann Y, et al. Inheritance in erythropoietic protoporphyria: a common wild-type ferrochelatase allelic variant with low expression accounts for clinical manifestation. Blood 1999; 93: 2105-2110.
13. Nakahashi Y, Fujita H, Taketani S, Ishida N, Kappas A, Sassa S. The molecular defect of ferrochelatase in a patient with erythropoietic protoporphyria. Proc Natl Acad Sci USA 1992; 89: 281-285.
14. Di Pierro E, Cappellini MD, Mazzucchelli R, Moriondo V, Mologni D, Zanone Poma B, et al. A point mutation affecting an SP1 binding site in the promoter of the ferrochelatase gene impairs gene transcription and causes erythropoietic protoporphyria. Exp Hematol 2005; 33: 584-591.
15. Whatley SD, Ducamp S, Gouya L, Grandchamp B, Beaumont C, Badminton MN, et al. C-terminal deletions in the ALAS2 gene lead to gain of function and cause X-linked dominant protoporphyria without anemia or iron overload. Am J Hum Genet 2008; 83: 408-14.
16. Yien YY, Ducamp S, van der Vorm LN, Kardon JR, Manceau H, Kannengiesser C, et al. Mutation in human CLPX elevates levels of delta-aminolevulinate synthase and protoporphyrin IX to promote erythropoietic protoporphyria. Proc Natl Acad Sci USA 2017; 114: E8045-52.
17. Whitman JC, Paw BH, Chung J. The role of ClpX in erythropoietic protoporphyria. Hematol Transfus Cell Ther 2018; 40: 182-8.
18. Snast I, Kaftory R, Sherman S, Edel Y, Hodak E, Levi A, et al. Acquired erythropoietic protoporphyria: A systematic review of the literature. Photodermatol Photoimmunol Photomed. 2020;36(1):29-33.
19. Suzuki H, Kikuchi K, Fukuhara N, Nakano H, Aiba

S. Case of late-onset erythropoietic protoporphyria with myelodysplastic syndrome who has homozygous IVS3-48C polymorphism in the ferrochelatase gene. J Dermatol. 2017;44(6):651-655.

20. Schneider-Yin X, Mamet R, Minder EI, Schoenfeld N. Biochemical and molecular diagnosis of erythropoietic protoporphyria in an Ashkenazi Jewish family. J Inherit Metab Dis 2008; Suppl 2: S363-367.

21. Saruwatari H, Ueki Y, Yotsumoto S, Shimada T, Fukumaru S, Kanekura T, et al. Genetic analysis of the ferrochelatase gene in eight Japanese patients from seven families with erythropoietic protoporphyria. J Dermatol 2006; 33: 603-608.

22. Elder GH, Gouya L, Whatley SD, Puy H, Badminton MN, Deybach JC. The molecular genetics of erythropoietic protoporphyria. Cell Mol Biol (Noisy-le-grand) 2009; 55: 118-126.

23. Tahara T, Yamamoto M, Akagi R, Harigae H, Taketani S. The low expression allele (IVS3-48C) of the ferrochelatase gene leads to low enzyme activity associated with erythropoietic protoporphyria. Int J Hematol 2010; 92: 769-771.

24. Brancaleoni V, Granata F, Missineo P, Fustinoni S, Graziadei G, Di Pierro E. Digital PCR (dPCR) analysis reveals that the homozygous c.315-48T>C variant in the FECH gene might cause erythropoietic protoporphyria (EPP). Mol Genet Metab 2018; 124: 287-296.

25. Nakano H, Nakano A, Toyomaki Y, Ohashi S, Harada K, Moritsugu R, et al. Novel ferrochelatase mutations in Japanese patients with erythropoietic protoporphyria: high frequency of the splice site modulator IVS3-48C polymorphism in the Japanese population. J Invest Dermatol 2006; 126: 2717-2719.

26. Mizawa M, Makino T, Nakano H, Sawamura D, Shimizu T. Incomplete erythropoietic protoporphyria caused by a splice site modulator homozygous IVS3-48C polymorphism in the ferrochelatase gene. Br J Dermatol 2016; 174: 172-175.

27. de Bataille S, Dutartre H, Puy H, Deybach JC, Gouya L, Raffray E, et al. Influence of meteorological data on sun tolerance in patients with erythropoietic protoporphyria in France. Br J Dermatol 2016; 175: 768-775.

28. Powell J, Badminton M. Shedding light on recent advances in our understanding of cutaneous porphyrias. Br J Dermatol 2018; 179: 1-2.

29. Sivaramakrishnan M, Woods J, Dawe R. Narrowband ultraviolet B phototherapy in erythropoietic protoporphyria: case series. Br J Dermatol 2014; 170: 987-988.

30. Nishikawa Y, Okuda S, Takebayashi C, Tanimoto T, Kami M, Kobayashi K. A case of late onset erythropoietic protoporphyria associated with myelodysplastic syndrome treated by the combination of beta carotene and azacitidine. Ann Hematol 2013; 92: 1415-1416.

31. Balwani M, Desnick RJ. The porphyrias: advances in diagnosis and treatment. Blood 2012; 120: 4496-4504.

32. Langendonk JG, Balwani M, Anderson KE, Bonkovsky HL, Anstey AV, Bissell DM, et al. Afamelanotide for erythropoietic protoporphyria. N Engl J Med 2015; 373: 48-59.

33. Suzuki T, Kawano Y, Matsumoto A, Kondo M, Funayama K, Tanemura S, et al. Melanogenic effect of dersimelagon (MT-7117), a novel oral melanocortin 1 receptor agonist. Skin Health Dis. 2021;2(1):e78.

34. Ventura P, Brancaleoni V, Di Pierro E, Graziadei G, Macrì A, Carmine Guida C, et al. Clinical and molecular epidemiology of erythropoietic protoporphyria in Italy. Eur J Dermatol 2020; 30: 532-540.

35. Wahlin S, Floderus Y, Stål P, Harper P. Erythropoietic protoporphyria in Sweden: demographic, clinical, biochemical and genetic characteristics. J Intern Med 2011; 269: 278-288.

36. Parker M, Corrigall AV, Hift RJ, Meissner PN. Molecular characterization of erythropoietic protoporphyria in South Africa. Br J Dermatol 2008; 159: 182-191.

37. Holme SA, Anstey AV, Finlay AY, Elder GH, Badminton MN. Erythropoietic protoporphyria in the U.K.: clinical features and effect on quality of life. Br J Dermatol 2006; 155: 574-581.

38. Todd DJ. Erythropoietic protoporphyria. Br J Dermatol 1994; 131: 751-766.

39. Went LN, Klasen EC. Genetic aspects of erythropoietic protoporphyria. Ann Hum Genet 1984; 48: 105-117.

40. Kong XF, Ye J, Gao DY, Gong QM, Zhang DH, Lu ZM, et al. Identification of a ferrochelatase mutation in a Chinese family with erythropoietic protoporphyria. J Hepatol. 2008;48(2):375-9.

41. Berroeta L, Man I, Goudie DR, Whatley SD, Elder GH, Ibbotson SH. Late presentation of erythropoietic protoporphyria: case report and genetic analysis of family members. Br J Dermatol. 2007;157(5):1030-1.

42. Schneider-Yin X, Harms J, Minder EI. Porphyria in Switzerland, 15 years experience. Swiss Med Wkly. 2009;139(13-14):198-206.

43. Farrag MS, Kučerová J, Šlachtová L, Šeda O, Šperl J, Martásek P. A Novel Mutation in the FECH Gene in a Czech Family with Erythropoietic Protoporphyria and a Population Study of IVS3-48C Variant Contributing to the Disease. Folia Biol (Praha). 2015;61(6):227-32.

44. Herrero C, To-Figueras J, Badenas C, Méndez M, Serrano P, Enríquez-Salamanca R, et al. Clinical, biochemical, and genetic study of 11 patients with erythropoietic protoporphyria including one with homozygous disease. Arch Dermatol. 2007;143(9):1125-9.

45. Aurizi C, Schneider-Yin X, Sorge F, Macrì A, Minder EI, Biolcati G. Heterogeneity of mutations in the ferrochelatase gene in Italian patients with erythropoietic protoporphyria. Mol Genet Metab.

2007;90(4):402-7.

46. Balwani M, Naik H, Anderson KE, Bissell DM, Bloomer J, Bonkovsky HL, et al. Clinical, Biochemical, and Genetic Characterization of North American Patients with Erythropoietic Protoporphyria and X-linked Protoporphyria. JAMA Dermatol 2017; 153: 789-796.

47. Kawada A, Gomi H, Shiraishi H, Hatanaka K, Matsuo I, Inafuku K, et al. An Infantile Case of Erythropoietic Protoporphyria with a Decreased mRNA Level of Ferrochelatase. Skin Research 2001; 43:111-115.

48. Imoto S, Tanizawa Y, Sato Y, Kaku K, Oka Y. A novel mutation in the ferrochelatase gene associated with erythropoietic protoporphyria. Porphyrins 1998; 7: 297-301.

49. Koga Y, Ogata R, Sakisaka S, Sakamoto A, Kuromatsu R, Uchimura Y, et al. A case of erythropoietic protoporphyria (EPP) with liver failure. Porphyrins 1998; 7: 279-284.

50. Aisaka Y, Asada N, Kitamoto M, Nakanishi T, Kajiyama G, Horie Y. Acute cholestasis associated with erythropoietic protoporphyria complicated with sepsis treated by antibiotics. Porphyrins 1998; 7: 274-278.

51. Shimazaki A, Hashimoto T, Kai M, Nakayama T, Yamada M, Zaguirre K, et al. Surgical treatment for breast cancer in a patient with erythropoietic protoporphyria and photosensitivity: a case report. Surg Case Rep. 2021;7(1):1.

52. Yoshida A, Hagiwara S, Watanabe T, Nishida N, Ida H, Sakurai T, et al. Erythropoietic Protoporphyria-related Hepatopathy Successfully Treated with Phlebotomy. Intern Med. 2018;57(17):2505-2509.

53. Fujimori N, Komatsu M, Tanaka N, Iwaya M, Nakano H, Sugiura A, et al. Cimetidine/lactulose therapy ameliorates erythropoietic protoporphyria-related liver injury. Clin J Gastroenterol. 2017;10(5):452-458.

54. Gomi H, Shiraishi K, Hatanaka K, Matsuo I. An infantile case of erythropoietic protoporphyria with a decreased mRNA level of ferrochelatase. Skin research. 2001;43:111-115.

55. Lecha M, Puy H, Deybach JC. Erythropoietic protoporphyria. Orphanet J Rare Dis 2009; 4: 19.

56. Murphy GM. Diagnosis and management of the erythropoietic porphyrias. Dermatol Ther 2003; 16: 57–64.

57. Michaels BD, Del Rosso JQ, Mobini N, Michaels JR. Erythropoietic protoporphyria: a case report and literature review. J Clin Aesthet Dermatol 2010; 3: 44-48.

58. Azad J, Brennan P, Carmichael AJ. New mutation identified in two sisters with adult-onset erythropoietic protoporphyria. Clin Exp Dermatol 2013; 38: 601-5.

59. Mizawa M, Makino T, Furukawa F, Torai R, Nakano H, Sawamura D, et al. The 6-year follow-up of a Japanese patient with silent erythropoietic protoporphyria. JAAD Case Rep 2017; 3: 169-171.

60. Zaidi Z. Characteristics of skin color. J Pak Med Assoc. 2016; 66: 914-915.

61. Eilers S, Bach DQ, Gaber R, Blatt H, Guevara Y, Nitsche K, et al. Accuracy of self-report in assessing Fitzpatrick skin phototypes I through VI. JAMA Dermatol. 2013; 149: 1289-1294.

62. Chan IL, Cohen S, da Cunha MG, Maluf LC. Characteristics and management of Asian skin. Int J Dermatol. 2019; 58: 131-143.

63. Whatley SD, Mason NG, Holme SA, Anstey AV, Elder GH, Badminton MN. Molecular epidemiology of erythropoietic protoporphyria in the U.K. Br J Dermatol 2010; 162: 642-646.

Mechanism of Photosensitized Protein Damage by Zinc Phthalocyanine

Kazutaka Hirakawa[1,2,3,4]*, Ayano Katayama[1], Shinya Yamaoka[2], and Shigetoshi Okazaki[5]

[1] Department of Applied Chemistry and Biochemical Engineering, Faculty of Engineering, Shizuoka University, Johoku 3-5-1, Naka-ku, Hamamatsu, Shizuoka 432-8561, Japan

[2] Applied Chemistry and Biochemical Engineering Course, Department of Engineering, Graduate School of Integrated Science and Technology, Shizuoka University, Johoku 3-5-1, Naka-ku, Hamamatsu 432-8561, Japan

[3] Department of Optoelectronics and Nanostructure Science, Graduate School of Science and Technology, Shizuoka University, Johoku 3-5-1, Naka-ku, Hamamatsu, Shizuoka 432-8561, Japan

[4] Cooperative Major in Medical Photonics, Shizuoka University, Johoku 3-5-1, Hamamatsu 432-8561, Japan

[5] Preeminent Medical Photonics Education and Research Center, Hamamatsu University School of Medicine, Handayama 1-20-1, Higashi-ku, Hamamatsu, Shizuoka 431-3192, Japan

*Corresponding author:

Prof. Dr. Kazutaka Hirakawa

Department of Applied Chemistry and Biochemical Engineering, Faculty of Engineering, Shizuoka University, Johoku 3-5-1, Naka-ku, Hamamatsu, Shizuoka 432-8561, Japan

Tel: (+)81-53-478-1287, Fax: (+)81-53-478-1287, E-mail: hirakawa.kazutaka@shizuoka.ac.jp

ABSTRACT

Zinc phthalocyanine (ZnPc) bound to the surface of human serum albumin (HSA), a water-soluble protein. Photoirradiated ZnPc oxidized the tryptophan residue of HSA. The inhibitory effect of sodium azide, a singlet oxygen ($^1O_2$) quencher, showed that the $^1O_2$-mediated mechanism partly contributes to this protein photodamage. However, only 20% of the protein photodamage was inhibited by sodium azide. Because the Gibbs energy of photoinduced electron transfer from tryptophan to the photoexcited ZnPc is negative, electron-transfer oxidation is possible in terms of thermodynamics. Fluorescence lifetime measurement also supported the electron-transfer quenching of photoexcited ZnPc by HSA. These results suggest that photoexcited ZnPc can damage protein through amino acid oxidation by electron extraction.

Keywords: Zinc phthalocyanine; Human serum albumin; Photodamage; Singlet oxygen; Electron transfer

INTRODUCTION

Phthalocyanine is a well-known singlet oxygen ($^1O_2$) generator [1,2]. Phthalocyanine can be photoexcited by long wavelength visible light, which can penetrate human tissue deeply, and the molar absorption coefficient of phthalocyanine is relatively large [1,2]. Therefore, phthalocyanine is considered to become an effective photosensitizer for photodynamic therapy (PDT), a less-invasive cancer treatment [1-4]. In addition, phthalocyanine is applied as the photosensitizer of photoimmunotherapy (PIT) [5]. The process by which PIT is triggered by phthalocyanine has been explained as being an oxygen-independent mechanism, the aggregation of phthalocyanine derivative molecules on the cell membrane (not $^1O_2$ production) [6,7]. Relevantly, the damaging effect of several photosensitizers on photosensitized biomolecules can be explained by an oxygen-independent mechanism, for example, the electron transfer-supported oxidation of biomolecules in addition to the $^1O_2$ production [8,9]. The electron-transfer mechanism depends on the redox potential of the photosensitizer and biomaterials. Tryptophan (Trp) residue of protein [8,9] and nicotinamide adenine dinucleotide (NADH) [9,10], the oxidation potential of which is relatively low, can be easily oxidized by photoexcited drugs through electron transfer. In this study, the possibility of electron transfer-mediated protein oxidation by phthalocyanine was examined. Phthalocyanines can form various metal complexes, change their photochemical properties, and induce electron-transfer reaction [11]. As a photosensitizer, zinc phthalocyanine (ZnPc), which has been extensively studied as a $^1O_2$ generator [1-4], was used to examine the photooxidation of human serum albumin (HSA), a water-soluble protein [12].

EXPERIMENTAL

ZnPc and HSA were purchased from Sigma-Aldrich Co. LLC. (St. Louis, MO, USA). Dimethyl sulfoxide (DMSO) and sodium azide (NaN_3) were purchased from FUJIFILM Wako Pure Chemical Co., Ltd. (Osaka, Japan). Spectroscopic-grade water was purchased from Dojin Chemicals Co. (Kumamoto, Japan). Methylene blue was obtained from Kanto Chemical, Co., Inc. (Tokyo, Japan). Sodium phosphate buffer (0.1 M, pH 7.6) was obtained from Nacalai Tesque Inc. (Kyoto, Japan). These chemical agents were used as received.

The absorption spectra of samples were measured with the UV-VIS spectrophotometer UV-1650PC (Shimadzu, Kyoto, Japan). The fluorescence spectra of samples were measured with an F-4500 fluorescence spectrophotometer (Hitachi, Tokyo, Japan). The fluorescence lifetime (τ_f), which equals the singlet excited-state (S_1) lifetime, of ZnPc and HSA was measured with a Fluorescence Lifetime System TemPro (HORIBA, Kyoto, Japan). The excitation wavelength for the τ_f measurements for ZnPc and HSA were 402 nm and 294 nm, respectively. The fluorescence quantum yield of ZnPc (Φ_f) was measured with an absolute photoluminescence quantum yield measurement system (C9920-20, Hamamatsu Photonics KK, Hamamatsu, Japan). The $^1O_2$ production was directly measured by near-infrared luminescence at around 1,270 nm from $^1O_2$ relaxation, which corresponds to the $^1O_2$ ($^1\Delta_g$)-$^3O_2$($^3\Sigma_g$) transition, as reported previously [13].

To evaluate the protein damage, the sample solution containing ZnPc and HSA was prepared in a 10 mM sodium phosphate buffer (pH 7.6) including 10% DMSO. The sample solution was irradiated with a light emitting diode (LED, λ_{max}= 659 nm, 2.0 mW cm^{-2}, CCS Inc., Kyoto, Japan). The intensity of the LED was measured with an 8230E optical power meter (ADC Corporation, Tokyo, Japan). The fluorescence intensity of HSA at 350

nm was measured with a fluorescence photometer 650-60 (Hitachi). The excitation wavelength for this assay was 298 nm. The amount of damaged HSA was estimated from the results of fluorometry based on the diminishment of the intrinsic fluorescence of Trp residue of HSA by photooxidation, as reported previously [8,9,14].

RESULTS AND DISCUSSION

Interaction between ZnPc and protein

Typical absorption peaks of ZnPc were clearly observed in DMSO (Fig. 1A). However, the absorption spectrum of ZnPc was broadened, and a hypochromic effect was observed in an aqueous solution (a 10 mM sodium phosphate buffer (pH 7.6) including 10% DMSO). This result suggests that hydrophobic ZnPc forms a self-aggregation. The absorption spectrum of ZnPc was slightly changed by the addition of HSA, a water-soluble protein, in a dose-dependent manner (Fig. 1B). This absorption spectral change can be explained by the interaction between ZnPc molecules and HSA. ZnPc is believed to bind to the hydrophobic pocket or surface of HSA. In the presence of a relatively small concentration of HSA, it is suggested that the aggregated ZnPc molecules bind to the HSA surface. The apparent binding constant (K) between ZnPc and HSA was calculated from an analysis of their absorbance change, as was previously reported [8,9,14]. In the case of a relatively small concentration of HSA, the estimated K value was 4.1×10^5 M^{-1}, assuming that two ZnPc molecules (ZnPc dimer) bind to the HSA surface (2:1 complex of ZnPc and HSA). In the presence of a large concentration of HSA, the absorbance of ZnPc reached a plateau at 10 μM HSA (Fig. 1B). This absorption spectral change could be analyzed with an assumption of a 1:1 complex formation, and the obtained K value was 1.1×10^6 M^{-1}. These findings show that 86% of ZnPc molecules are binding on HSA in the experimental condition of 5 μM ZnPc and 10 μM HSA. The binding position of ZnPc on HSA in the 1:1 complex (5 μM ZnPc and 10 μM HSA) was examined by the Förster resonance energy transfer (FRET) method based on the energy transfer theory [15] with a previously reported procedure that uses the average τ_f value of the Trp residue of HSA [9]. The critical distance of the FRET from the Trp to ZnPc, which was calculated from the fluorescence spectrum of Trp and the absorption spectrum of ZnPc, was 23.8 Å. The average τ_f of the Trp residue of HSA without ZnPc (6.35 ns) was decreased to be (5.15 ns) by the binding ZnPc molecules through the FRET. The estimated distance between the binding ZnPc molecule and the Trp residue of HSA, which is located almost at the center of HSA [12], was 30.3 Å. Since the average diameter of HSA is about 80 Å [16], the obtained value suggests that ZnPc molecules bind to the HSA surface.

The fluorescence of ZnPc was barely observed in the aqueous solution in this experimental condition (a 10 mM sodium phosphate buffer including 10% DMSO). In the
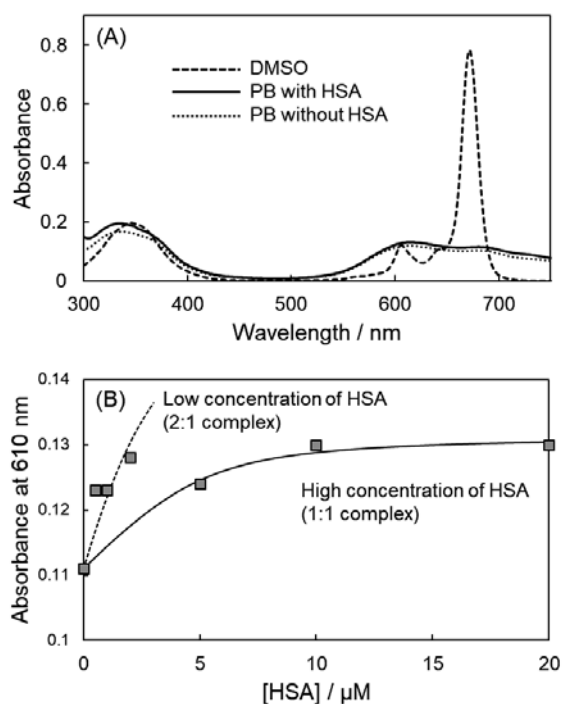

Fig. 1. The absorption spectra of ZnPc (A) and the absorbance change of ZnPc by HSA (B). The sample solution contained 5 μM ZnPc in DMSO or a 10 mM sodium phosphate buffer (pH 7.6) plus 10% DMSO (PB in this figure) with or without 10 μM HSA (A). For the absorbance change measurement, sample solutions containing 5 μM ZnPc and the indicated concentration of HSA were prepared in PB (B). The presented curves were simulated by reported previously, under the assumption of 2:1 (Low concentration of HSA) or 1:1 (High concentration of HSA) complex of ZnPc and HSA [8,14].

presence of HSA, the fluorescence intensity increased as the HSA concentration increased (Fig. 2). The Φ_f of ZnPc was recovered from a trace (without HSA) to 0.04 (with 10 μM HSA). The τ_f value of ZnPc was also increased from 0.01 ns (without HSA) to 5.95 ns (29%), 2.46 ns (59%), and 0.25 ns (12%) (with 10 μM HSA). The longest lifetime component (5.95 ns) can be assigned to the ZnPc monomer binding to the HSA surface. The other observed components of τ_f values can be explained by the ZnPc molecules binding to other positions of the HSA surface and the aggregation of ZnPc molecules. The fluorescence measurements demonstrate that the photoexcited state of ZnPc is quenched through self-aggregation, and the interaction with HSA resolves the aggregation state, resulting in the recovery of the photosensitizer activity of ZnPc.
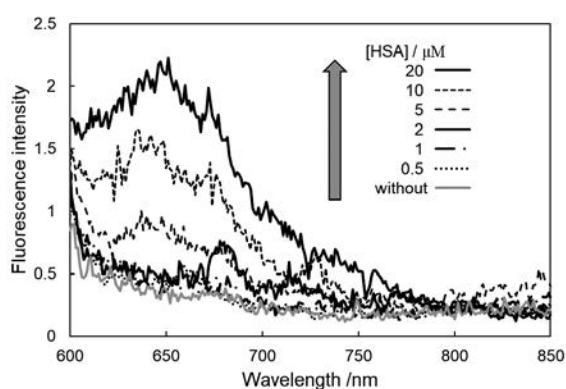
Fig. 2. Fluorescence spectra of 5 μM ZnPc with the indicated concentration of HSA in a 10 mM sodium phosphate buffer (pH 7.6) plus 10% DMSO. The excitation wavelength for fluorescence measurement was 590 nm.

Photosensitized protein oxidation by ZnPc

The photosensitized protein damage by ZnPc was evaluated using a fluorescence intensity of the Trp residue of HSA, which shows the typical fluorescence as being around 350 nm, as reported previously [8,9,14]. The protein damage photosensitized by ZnPc increased in a dose-dependent manner (Fig. 3). The total quantum yield of protein damage (Φ_D: 2.0×10^{-4}) was estimated from the initial decomposition rate and the absorbed photon fluence by ZnPc. This protein damage was partially inhibited by NaN$_3$, a physical quencher of $^1O_2$ [17]. ZnPc is a well-known $^1O_2$ generator [1,2]. It has been reported that the quantum yield of $^1O_2$ production (Φ_Δ) photosensitized by ZnPc is 0.67 in DMSO [18]. In this study, the near infrared emission at around 1270 nm assigned to the $^1O_2$ was detected during photoirradiation to ZnPc. The Φ_Δ was estimated by comparison with the near infrared emission intensity using methylene blue (Φ_Δ of methylene blue: 0.52, [19]). The estimated Φ_Δ of ZnPc in a 10 mM phosphate buffer including 10% DMSO was 0.04 and increased to 0.13 in the presence of 10 μM HSA, suggesting that the self-aggregation of ZnPc was resolved through interaction with HSA.
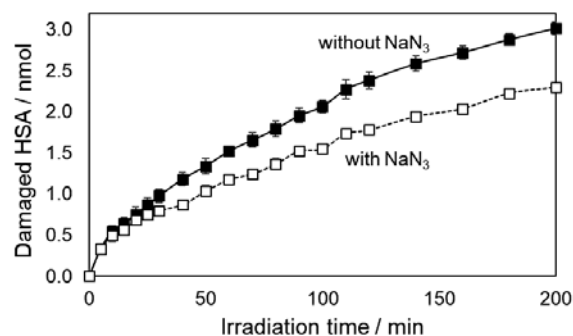

Fig. 3. The time profile of photosensitized HSA damage by ZnPc. The sample solution contained 5 μM ZnPc and 10 μM HSA with (□) or without (■) 10 mM NaN$_3$ in a 10 mM sodium phosphate buffer (pH 7.6) plus 10% DMSO. The sample solution was irradiated with an LED (λ_{max}= 659 nm, 2.0 mW cm^{-2}).

The addition of NaN$_3$ could not completely inhibit the HSA damage photosensitized by ZnPc, and an excess amount of NaN$_3$ (10 mM) inhibited the protein photodamage by only 20%. It is possible that HSA damage photosensitized by ZnPc with NaN$_3$ is an electron transfer-supported oxidation. Photoexcited ZnPc may extract an electron from the amino acid residue of HSA. In this study, the Trp residue of HSA was damaged by photoirradiation with ZnPc. The oxidized Trp residue is decomposed into further damaged products such as N-formylkynurenine [20,21]. Other amino acids, for example, tyrosine, histidine, and cysteine, are also considered to be oxidized through these mechanisms [22]. The Gibbs energy (ΔG) of Trp oxidation by the photoexcited state of ZnPc (S$_1$ of ZnPc) was roughly calculated by the redox potentials of the one-electron oxidation of Trp (0.78 V vs. saturated calomel electrode; SCE) [23], the one-electron reduction of ZnPc (0.86 V vs. SCE) [24,25], and the S$_1$ energy of ZnPc (1.93 eV, calculated from the fluorescence peak), similar to previous reports [8,9,14]. The estimated ΔG value was negative (-0.29 eV), supporting the possibility of electron transfer-mediated oxidation. The above-mentioned τ_f value of ZnPc also supports the electron-transfer mechanism. The shorter τ_f values of ZnPc with 10 μM HSA, 2.46 ns ($\tau_{f(short1)}$) and 0.25 ns ($\tau_{f(short2)}$), can be explained by the quenching of S$_1$ of ZnPc through electron transfer. The difference in the two observed shorter τ_f values can be explained by the difference in the binding position of the ZnPc molecule on the HSA surface. The τ_f values of chromophores binding on HSA depend on the microenvironment of binding position and to be complex [26]. A previous report suggests that the multi-components of τ_f values are due to the difference in the binding position of the photosensitizer molecules on the HSA surface [27]. One of the possible factors to affect the τ_f values is the difference of the distance between the binding ZnPc molecule and the Trp residue of HSA. The electron-transfer rate constant (k_{ET}) can be calculated by the following equation using the longest τ_f value ($\tau_{f(long)}$: 5.95 ns):

$$k_{ET} = \frac{1}{\tau_{f(short1)}} - \frac{1}{\tau_{f(long)}} \text{ or } \frac{1}{\tau_{f(short2)}} - \frac{1}{\tau_{f(long)}} \quad (1).$$

The calculated values using $\tau_{f(short1)}$ and $\tau_{f(short2)}$ were 2.4×10^8 s^{-1} and 3.8×10^9 s^{-1}, respectively. These rate constants are markedly larger than the diffusion-controlled process (7.4×10^4 s^{-1}), which is calculated from the diffusion-controlled rate coefficient in water at 298 K (7.4×10^9 M^{-1} s^{-1}). These findings kinetically support the association of ZnPc with HSA and the electron transfer-mediated oxidation of HSA by the S$_1$ of ZnPc. On the other hand, the triplet excited-state (T$_1$) energy of ZnPc (1.1 eV) [28] is small, and the estimated ΔG of the electron transfer from Trp to the T$_1$ of ZnPc becomes a positive value (+0.41 eV). Therefore, the possibility of electron-transfer oxidation of Trp by the T$_1$ of ZnPc is negligible. The quantum yields of HSA damage photosensitized by ZnPc through $^1O_2$ production ($\Phi_{D(\Delta)}$) and electron-transfer ($\Phi_{D(ET)}$) mechanisms can be estimated by the following equation:

$$\Phi_D = \Phi_{D(\Delta)} + \Phi_{D(ET)} \quad (2).$$

$\Phi_{D(ET)}$ equals the HSA photodamaging quantum yield by ZnPc in the presence of NaN$_3$. The estimated values of $\Phi_{D(\Delta)}$ and $\Phi_{D(ET)}$ are 4.0×10^{-5} and 1.6×10^{-4}, respectively. The obtained values suggest that the electron-transfer mechanism is important in the photosensitized protein oxidation by ZnPc.

CONCLUSIONS

Hydrophobic ZnPc bound to the HSA surface. In the experimental condition (5 μM ZnPc and 10 μM HSA), most ZnPc molecules (86%) can associate with the surface of HSA. Therefore, photosensitized protein oxidation by ZnPc can be evaluated using HSA. Photoirradiated ZnPc effectively oxidized the Trp residue of HSA. Analysis of the effect of NaN$_3$ showed that the contribution of the $^1O_2$-mediated mechanism is relatively small. The calculation of the ΔG value and τ_f measurement supported the oxidation of Trp residue of HSA through electron transfer. The relaxation process of photoexcited ZnPc and the proposed mechanism of protein damage photosensitized by ZnPc are shown in Fig. 4. The S$_1$ of ZnPc induces the oxidation of protein through electron transfer, and several parts of the S$_1$ of ZnPc change to the T$_1$, leading to the production of $^1O_2$. In the presence of enough oxygen,
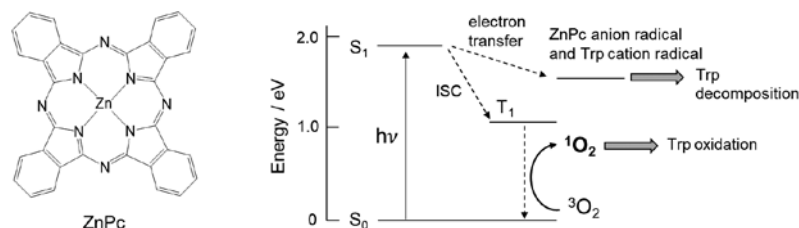
$^1O_2$ should be the important reactive species to oxidize biomolecules by photoirradiated ZnPc. The $^1O_2$-mediated mechanism of phototoxicity of phthalocyanines has been generally accepted; however, this study suggests that the electron transfer-supported oxidation mechanism also contributes to the phototoxic effect of phthalocyanine metal complexes.

Notes

The authors declare no conflict of interests.

References

1. Lang K, Mosinger J, Wagnerová DM. Photophysical properties of porphyrinoid sensitizers non-covalently bound to host molecules; models for photodynamic therapy. Coord Chem Rev, 2004;248:321–350.
2. Matlou GG, Oluwole DO, Prinsloo E, Nyokong T. Photodynamic therapy activity of zinc phthalocyanine linked to folic acid and magnetic nanoparticles. J Photochem Photobiol B, 2018;186:216–224.
3. Abrahamse H, Hamblin MR. New photosensitizers for photodynamic therapy. Biochem J, 2016;473:347-364.
4. Janas K, Boniewska-Bernacka E, Dyrda G, Słota R. Porphyrin and phthalocyanine photosensitizers designed for targeted photodynamic therapy of colorectal cancer. Bioorg Med Chem, 2021;30:115926.
5. Mitsunaga M, Ogawa M, Kosaka N, Rosenblum LT, Choyke PL, Kobayashi H. Cancer cell-selective in vivo near infrared photoimmunotherapy targeting specific membrane molecules. Nat Med, 2011;17:1685–1691.
6. Kobayashi H, Choyke PL. Near-infrared photoimmunotherapy of cancer. Acc Chem Res, 2019;52:2332–2339.
7. Ogawa M, Takakura H. Photoimmunotherapy: A new cancer treatment using photochemical reactions. Bioorg Med Chem, 2021;3:116274.
8. Hirakawa K, Ouyang D, Ibuki Y, Hirohara S, Okazaki S, Kono E, Kanayama N, Nakazaki J, Segawa H. Photosensitized protein-damaging activity, cytotoxicity, and antitumor effects of P(V)porphyrins

Fig. 4. The structure of ZnPc (left) and the relaxation process of photoexcited ZnPc binding to HSA (right). ISC: intersystem crossing.

using long-wavelength visible light through electron transfer. Chem Res Toxicol, 2018;31:371–379.

9. Hirakawa K, Takai S, Horiuchi H, Okazaki S. Photooxidation activity control of dimethylaminophenyltris-(N-methyl-4-pridinio)porphyrin by pH. ACS Omega, 2020;5:27702−27708.

10. Hirakawa K, Murata A. Photosensitized oxidation of nicotinamide adenine dinucleotide by diethoxyphosphorus(V)tetraphenylporphyrin and its fluorinated derivative: Possibility of chain reaction. Spectrochim Acta A, 2018;188:640−646.

11. Ito F, Ishibashi Y, Khan SR, Miyasaka H, Kameyama K, Morisue M, Satake A, Ogawa K, Kobuke Y. Photoinduced electron transfer and excitation energy transfer in directly linked zinc porphyrin/ zinc phthalocyanine composite. J Phys Chem A, 2006;110:12734–12742.

12. He XM, Carter DC. Atomic structure and chemistry of human serum albumin. Nature, 1992;358:209–215.

13. Hirakawa K, Nishimura Y, Arai T, Okazaki S. Singlet oxygen generating activity of an electron donor connecting porphyrin photosensitizer can be controlled by DNA. J Phys Chem B, 2013;117:13490−13496.

14. Hirakawa K, Suzuki A, Ouyang D, Okazaki S, Ibuki Y, Nakazaki J, Segawa H. Controlled photodynamic action of axial fluorinated diethoxyP(V)tetrakis(*p*-methoxyphenyl)porphyrin through self-aggregation. Chem Res Toxicol, 2019;32:1638–1645.

15. Förster, T. Zwischenmolekulare energiewanderung und fluoreszenz. Ann Phys, 1948:437:55−75.

16. Ferrer ML, Duchowicz R, Carrasco B, de la Torre JG, Acuña AU. The conformation of serum albumin in solution: a combined phosphorescence depolarization-hydrodynamic modeling study. Biophys J, 2001;80:2422–2430.

17. Li MY, Cline CS, Koker EB, Carmichael HH, Chignell CF, Bilski P. Quenching of singlet molecular oxygen ($^1O_2$) by azide anion in solvent mixtures. Photochem Photobiol, 2001;74:760–764.

18. Staicu A, Pascu A, Nuta A, Sorescu A, Raditoiu V, Pascu ML. Studies about phthalocyanine photosensitizers to be used in photodynamic therapy. Rom Rep Phys, 2013;65:1032–1051.

19. Usui Y, Kamogawa K. A standard system to determine the quantum yield of singlet oxygen formation in aqueous solution. Photochem Photobiol, 1974;19:245–247.

20. Gieβauf A, van Wickern B, Simat T, Steinhart H, Esterbauer H. Formation of *N*-formylkynurenine suggests the involvement of apolipoprotein B-100 centered tryptophan radicals in the initiation of LDL lipid peroxidation. FEBS Lett, 1996;389:136–140.

21. Gracanin M, Hawkins CL, Pattison DI, Davies MJ. Singlet-oxygen-mediated amino acid and protein oxidation: formation of tryptophan peroxides and decomposition products. Free Radic Biol Med, 2009;47:92–102.

22. Ouyang D, Hirakawa K. Photosensitized enzyme deactivation and protein oxidation by axial-substituted phosphorus(V) tetraphenylporphyrins. J Photochem Photobiol B, 2017;175:125–131.

23. Sakura S. Chemiluminescence of tryptophan enhanced by electrochemical energy. Electrochim Acta, 1992;37:2731–2735.

24. Giraudeau A, Louati A, Gross M, Andre JJ, Simon J, Su CH, Kadish KM. Redox properties of octacyano-substituted zinc phthalocyanine ((CN)$_8$PcZn). New charge-transfer complex. J Am Chem Soc, 1983;105:2917–2919.

25. Feridun SG, Orman EB, Salan Ü, Özkaya AR, Bulut M. Synthesis, characterization, and electrochemical and in-situ spectroelectrochemical properties of novel peripherally and nonperipherally 7-oxy-3-(3,4-dimethoxyphenyl) coumarin substituted phthalocyanines. Dye Pigmt, 2019;160:315–327.

26. Kundu P, Chattopadhyay N. Unraveling the binding interaction of a bioactive pyrazole-based probe with serum proteins: Relative concentration dependent 1:1 and 2:1 probe-protein stoichiometries. Biophys Chem, 2018;240:70–81.

27. Hirakawa K, Yoshida M, Hirano T, Nakazaki J, Segawa H. Photosensitized protein damage by diethyleneglycoxyP(V)tetrakis(*p-n*-butoxyphenyl) porphyrin through electron transfer: Activity control through self-aggregation and dissociation. Photochem Photobiol, in press; doi: 10.1111/php.13517.

28. Ueno LT, Jayme CC, Silva LR, Pereira EB. de Oliveira SM, Machado AEH. Photophysics and spectroscopic properties of zinc phthalocyanine revisited using quantum chemistry. J Braz Chem Soc, 2012;23:2237–2247.

Copper Ion Trapping by Artificial Oligonucleotides Identified using Raman Spectroscopy

Kousuke Meisho, Tatsuya Nishihara, and Kazuhito Tanabe*

Department of Chemistry and Biological Science, College of Science and Engineering, Aoyama Gakuin University, 5-10-1 Fuchinobe, Chuo-ku, Sagamihara, Kanagawa 252-5258, Japan

ABSTRACT

Raman spectroscopy has been applied to measure molecular vibrational modes and obtain structural fingerprints. In this study, we aimed to identify metal ion-ligand complexes by tracking Raman scattered light and applied the system to the detection of copper ions (Cu^{2+}). We employed oligodeoxynucleotides (ODNs) as molecular probes for the detection of metal ions in biological systems because of their high water solubility and biocompatibility. Initially, we synthesized monomeric uridine derivative ($d^{Py}U$) bearing phenylacetylene unit as a Raman tag, and ligand unit for complexation with Cu^{2+}. The $d^{Py}U$ showed strong signal at 2209 cm^{-1}, which were shifted to 2215 cm^{-1} in the presence of Cu^{2+} ion. Then, we prepared ODNs bearing ligand unit for Cu^{2+} ion complexation. The ODN showed a strong Raman signal at approximately 2210 cm^{-1} attributed to the acetylene unit. In addition, when Cu^{2+} ions were added, the signal shifted to the high wavenumber side due to complex formation. Thus, Cu^{2+} could be detected by monitoring the Raman band shift.

INTRODUCTION

Artificial oligodeoxynucleotides (ODNs) have been used as functional materials in living cells and tissues.[1–3] For example, modification of cell membranes, drug delivery, and genetic manipulation have all been achieved using these functional oligonucleotides.[4–6] One of thier most useful applications is as molecular probes.[7,8] Because of the high water solubility and biocompatibility of ODNs, reporter molecule-labeled ODNs have been utilized to visualize a variety of biological factors.

Raman spectroscopy provides a structural fingerprint of the target molecule by detecting the vibrations of chemical bonds.[9] Recently, Raman probes with alkyne tags have shown promise for detecting biomolecules. Our group and others have applied various Raman probes to visualize a series of biofunctional molecules, including molecular oxygen, specified enzymes, and specified DNAs.[10–14]

Herein, we attempted to apply artificial ODNs to detect metal ions using Raman spectroscopy. We designed an artificial nucleobase bearing ligand unit for Cu^{2+} ion, the complexation of which could be tracked by monitoring the Raman spectra. We employed a pyridine derivative[15] as a ligand for Cu^{2+} and modified it with an alkyne as a Raman tag because alkynes exhibit a characteristic and robust Raman signal. The resulting ligand with an acetylene unit was incorporated into a nucleobase, 2'-deoxyuridine, at the 5-position to form **$d^{Py}U$** (Figure 1), which was further introduced into ODNs. Eventually, a monomeric **$d^{Py}U$** derivative and its corresponding ODN with **$d^{Py}U$** showed strong binding and complexation with Cu^{2+}, which led to a signal shift in the Raman spectrum. Thus, the Cu^{2+} ion could be detected by Raman spectroscopy.
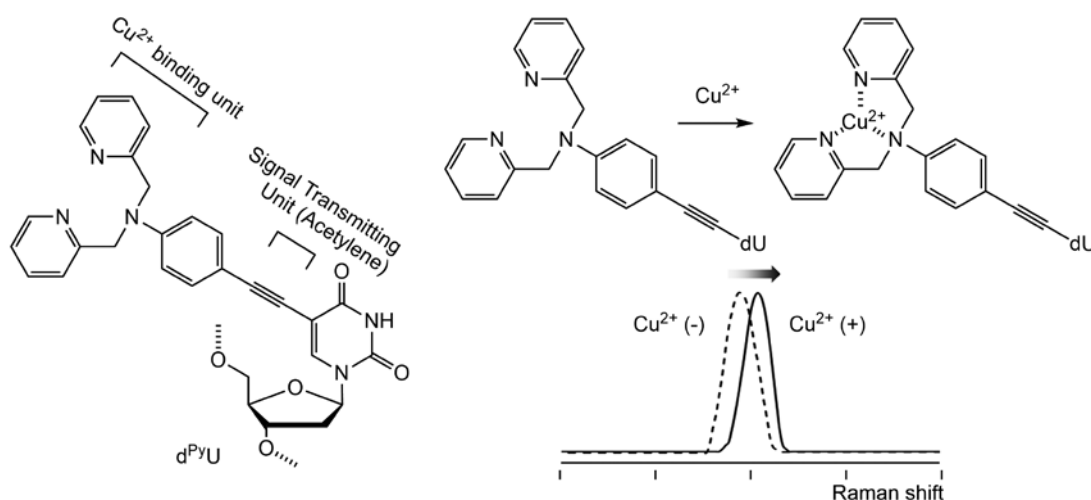

Figure 1. Outline for detection of Cu^{2+} by measurement of Raman spectra and chemical structure of 2'-deoxyuridine derivative bearing ligand unit (**$d^{Py}U$**).

MATERIALS AND METHODs

General Method. Reagents were purchased from Wako pure chemical industries, Tokyo chemical industries and Sigma Aldrich. Compound 1[16] and 2[17] were synthesized by the methods reported previously. NMR spectra were recorded on JEOL JIN-ECX500 II (^{1}H: 500 MHz,^{13}C: 125 MHz) spectrometer and chemical shifts were expressed in ppm downfield from tetramethylsilane, using residual protons in solvents as internal standards. Raman spectrum measurement was carried out on a RENISHAW in Via Raman Microscope.

Synthesis of Ac$_2$-d^{Py}U. To the mixture of Compound 2 (126.8 mg 0.289 mmol), Et$_3$N (330 μL 2.38 mmol) and Pd(PPh$_3$)$_4$ (36.5 mg 0.0316 mmol) in THF (1 mL), compound 1 (137.5 mg 0.314mmol) and CuI (13.4 mg 0.074 mmol) were added and the resulting mixture was stirred for 7 h at ambient temperature. After the reaction, the solvent was removed under reduced pressure, and then, the crude product was purified by by column chromatography (Hex/EtAc=5:1) to give **Ac$_2$-d^{Py}U** as yellow solid (33.2 mg, 19%). ^{1}H NMR (CDCl$_3$, 500 MHz) δ 8.58 (dd, J = 1.0, 4.0 Hz, 2H), 7.78 (s, 1H), 7.62 (ddd, J = 1.5, 7.0, 7.0 Hz, 2H), 7.25 (d, J = 9.5 Hz, 2H), 7.20 (q, J = 7.5 Hz, 2H), 7.17 (dd, J = 5.0, 7.5 Hz, 2H), 6.62 (d, J = 9.5 Hz, 2H), 6.31 (dd, J = 5.5, 8.0 Hz, 1H), 5.22 (ddd, J = 2.5, 2.5, 6.0 Hz, 1H), 4.82 (s, 4H), 4.34 (d, J = 2.5 Hz, 2H), 4.26 (ddd, J = 3.0, 3.0, 3.0 Hz, 1H), 2.51 (ddd, J = 2.0, 5.5, 14.5 Hz, 1H), 2.20 (ddd, J = 7.0, 7.5, 14.5 Hz, 1H), 2.14 (s, 3H), 2.09 (s, 3H); ^{13}C NMR (CDCl$_3$, 125 MHz) δ 170.6, 161.2, 158.2, 158.1, 150.0, 149.4, 140.3, 137.2, 133.2, 131.1, 129.0, 126.8, 122.4, 121.1, 112. 5, 102.0, 95.0, 85.5, 82.7, 74.3, 64.1, 57.3, 38.3, 21.1; FABMS (NBA) m/z 609 [(M + H)$^+$]; HRMS (NBA) calcd for C$_{33}$H$_{31}$N$_5$O$_7$ [(M + H)$^+$], 609.2223; found 609.2228; mp 79–81 ˚C.

Synthesis of compound 3. To the solution of **Ac$_2$-d^{Py}U** (120.3 mg, 0.198 mmol) in MeOH (1.5 mL), NaOH (2 M, 0.5 mL) was added, and then the resulting solution was stirred for 2 h at ambient temperature. After the reaction, the solvent was removed under reduced pressure, and the crude product was purified by column chromatography (CHCl$_3$/MeOH=20:1) to give 3 as yellow solid (85.9 mg, 83%). ^{1}H NMR (CD$_3$OD, 500 MHz) δ 8.53 (dd, J = 1.0, 4.0 Hz, 2H), 8.30 (s, 1H), 7.78 (ddd, J = 1.5, 7.5, 7.5 Hz, 2H), 7.35 (d, J = 8.0 Hz, 2H), 7.31 (dd, J = 5.5, 7.5 Hz, 2H), 7.27 (d, J = 9.0 Hz, 2H), 6.65 (d, J = 9.5 Hz, 2H), 6.26 (t, J = 6.5 Hz, 1H), 4.89 (s, 4H), 4.40 (ddd, J = 3.5, 3.5, 6.5 Hz, 1H), 3.93 (ddd, J = 3.5, 3.5, 3.5 Hz, 1H), 3.82 (dd, J = 3.0, 12.0 Hz, 1H), 3.73 (dd, J = 3.0, 12.0 Hz, 1H), 2.30 (ddd, J = 3.3, 6.0, 13.8 Hz, 1H), 2.24 (ddd, J = 6.5, 6.5, 13.5 Hz, 1H); ^{13}C NMR (CD$_3$OD, 125 MHz) δ 173.0, 171.4, 159.7, 158.1, 157.0, 150.7, 150.4, 139.1, 137.7, 127.5, 124.0, 122.9, 114.1, 96.1, 89.9, 71.6, 62.5, 57.9, 43.0, 30.9, 23.9; FABMS (NBA) m/z 525 [(M + H)+]; HRMS (NBA) calcd. for C$_{29}$H$_{27}$N$_5$O$_5$ [(M + H)$^+$], 525.2012 ; found 525.2012; mp 194–196 ˚C.

Synthesis of compound 4. To the solution of compound 3 (28.7 mg 0.0546 mmol) in pyridine (0.5 mL), DMTrCl (22.2 mg, 0.0655 mmoL) was added. The resulting mixture was stirred for 4 h at ambient temperature, and then heated to 80 ˚C for 12 h. After the reaction, the mixture was extracted with ethyl acetate, washed with water then brine, dried over anhydrous magnesium sulfate and concentrated in vacuo. The crude product was purified by column chromatography (hexane / EtOAc = 2:1) to give 4 as light yellow solid (12.8 mg, 3.5%). ^{1}H NMR (DMSO-d$_6$, 500 MHz) δ 8.52 (d, J = 4.0 Hz, 2H), 7.85 (s, 1H), 7.70 (ddd, J = 2.0, 7.5, 7.5 Hz, 2H), 7.27–7.16 (10H), 7.06 (t, J = 7.5, 7.5 Hz, 1H), 6.85 (d, J = 9.0 Hz, 2H), 6.76 (dd, J = 7.5, 9.0 Hz, 4H), 6.52 (d, J = 9.0 Hz, 1H), 6.08 (t, J = 7.0 Hz, 1H), 5.29 (d, J = 4.5 Hz, 1H), 4.81 (s, 4H), 4.24 (ddd, J = 3.5, 3.5, 8.5 Hz, 1H), 3.90 (ddd, J = 3.0, 3.0, 6.0 Hz, 1H), 3.68 (ddd, J = 3.0, 3.0, 6.0 Hz, 1H), 3.57 (s, 3H), 3.56 (s, 3H), 2.24–2.12 (2H); ^{13}C NMR (DMSO-d$_6$, 125 MHz) δ 162.0, 159.0, 158.6, 149.9, 148.5, 145.2, 142.2, 137.3, 136.1, 135.8, 132.7, 130.2, 130.1, 128.4, 128.1, 127.2, 122.8, 121.6, 113.7, 112.5, 109.7, 99.9, 93.6, 86.4, 85.5, 79.9, 71.0, 70.3, 64.2, 57.3, 55.4; FABMS (NBA) m/z 827 [(M + H)$^+$]; HRMS(NBA) calcd for C$_{50}$H$_{45}$N$_5$O$_7$ [(M + H)$^+$], 827.3319; found 827.3343; mp 110–112 ˚C.

Synthesis of ODN 1. N,N-diisopropylethylamine (41 μl, 0.24 mmol) and 2-cyanoethyldiisoproryl-chlorophosphoramidite (21 μl, 0.094 mmol) were added to compound 4 (38.5 mg, 0.047 mmol) in anhydrous acetonitrile (580 μl) and stirred for 1.5 h at room temperature. After the reaction, the mixture was filtered and placed on DNA synthesizer. After automated DNA synthesis, **ODN 1** was purified by reversed phase HPLC. The purity and concentration of the oligomers were determined by complete digestion with AP, P1 and phosphodiesterase I at 37 ˚C for 15 h. Identities of synthesized oligomers were identified by MALDI-TOF mass spectrometry (**ODN 1**: [M - H]$^-$ calcd. 6234.1, found 6234.2.

Measurement of Raman Spectra. Ac$_2$-d^{Py}U and **ODN 1** were solved in designated solvents and measured their Raman spectra (Ex. 532 nm).

RESULTS AND DISCUSSION

The synthesis of the ligands bearing an acetylene unit on 2'-deoxyuridine is illustrated in Figure 2A. Phenylacetylene 1 and iodo-deoxyuridine derivative 2 were coupled to give **Ac$_2$-d^{Py}U**.[16,17]

Initially, we measured the absorption spectra of monomeric **Ac$_2$-d^{Py}U** to characterize the complexation with the Cu^{2+} ion. As shown in Figure 2B, we observed absorption at 360 nm in the absence of Cu^{2+}. The addition of Cu^{2+} resulted in a decrease of the absorption at 360 nm, whereas an increase in absorption at 310 nm was observed. An isosbestic point was located, which indicates
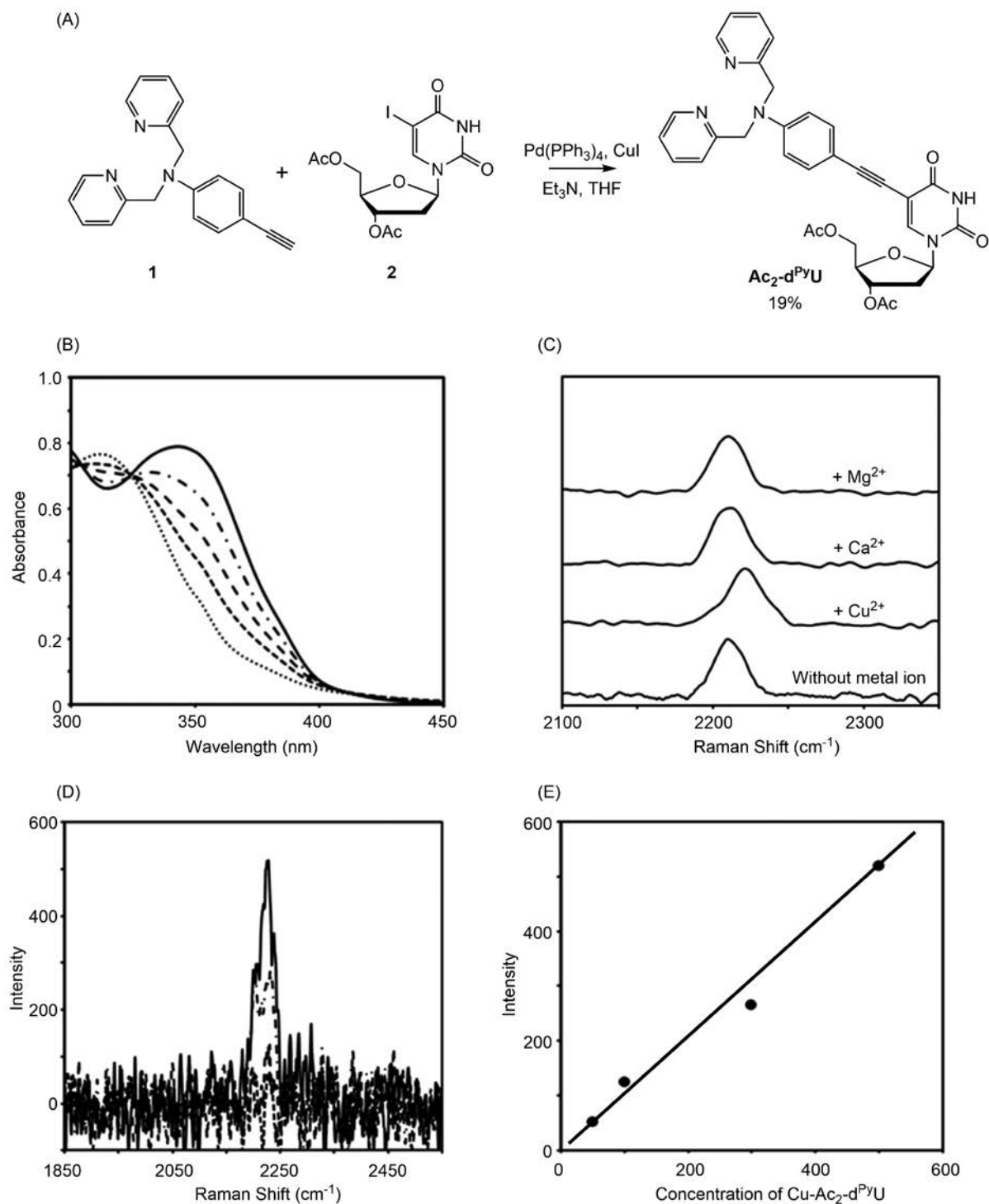
Figure 2. (A) Synthesis of **Ac2-d^{Py}U**. (B) Absorption spectra of **Ac$_2$-d^{Py}U** (25 μM) in the presence of CuCl$_2$ (0 (solid line), 5 (chain line), 10 (long dashed line), 15 (dashed line) and 25 μM (dotted line)). (C) Raman spectra of **Ac$_2$-d^{Py}U** (500 μM) in the presence or absence of CuCl$_2$ (500 μM), MgCl$_2$ (500 μM) or CaCl$_2$ (500 μM). (D) Raman spectra of **Ac$_2$-d^{Py}U** in the presence of CuCl$_2$. The Raman spectra of various concentration (500 μM: solid line, 300 μM: chain line, 100 μM: dashed line, 50 μM: dotted line) of the complex consisted of Cu^{2+} and **Ac$_2$-d^{Py}U** were measured. (E) Plot of Raman signal intensity at 2227 cm^{-1} vs concentration of complex consisted of Cu^{2+} and **Ac$_2$-d^{Py}U**. The Raman spectra were measured using 532 nm excitation.
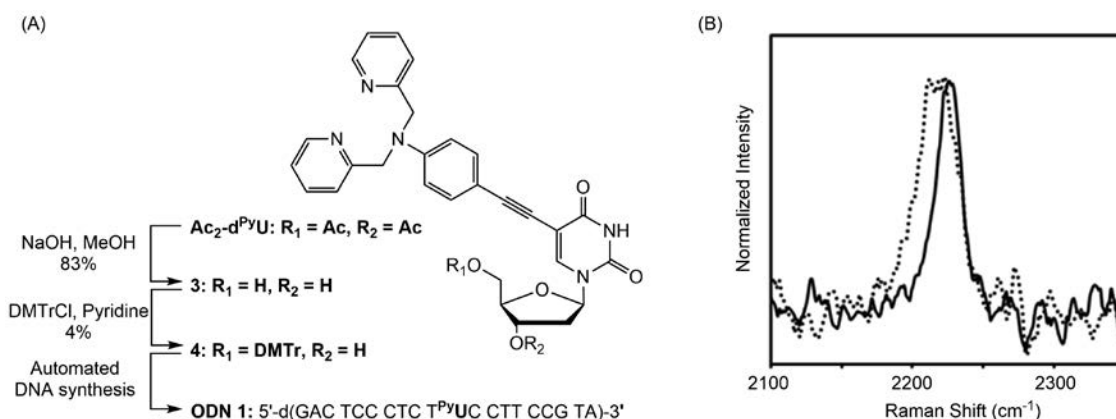
Figure 3. (A) Synthesis of **ODN 1**. (B) Raman spectra of **ODN 1** (500 μM) in the presence (solid line) or absence (dotted line) of CuCl$_2$ (500 μM). The Raman spectra were measured using 532 nm excitation.

a quantitative change from **Ac₂-d^{Py}U** to the **Ac₂-d^{Py}U-Cu^{2+}** complex. From this ultraviolet titration, we estimated the apparent dissociation constant, K_d (2.5 μM). Thus, **d^{Py}U** retained the binding ability with Cu^{2+}, even when the ligand moiety was on the nucleobase.

We next measured the Raman spectra in the presence of Cu^{2+} ions. As shown in Figure 2C, **Ac₂-d^{Py}U** showed a typical band arising from the acetylene group at 2209 cm^{-1}. When 1 equiv of Cu^{2+} was added to **Ac₂-d^{Py}U**, the band shifted from 2209 to 2215 cm^{-1}. These results indicate that the binding of Cu^{2+} caused a shift in the vibrational frequency of the acetylene unit in **Ac₂-d^{Py}U**. In separate experiments, similar treatment of **Ac₂-d^{Py}U** by other metal ions such as Mg^{2+} or Ca^{2+}, which exhibit diverse function in the cells, was conducted, but a negligible change in the Raman band at 2209 cm^{-1} was observed (Figure 2C). Thus, **Ac₂-d^{Py}U** showed selective binding with Cu^{2+}. The sensitivity of this system was also evaluated. The Raman spectra of **Ac₂-d^{Py}U** were measured in the presence of various concentrations of Cu^{2+}. As shown in Figure 2D, the signal of acetylene units was clearly observed at concentrations above 100 μM. In addition, concentration and signal intensity were found to be almost proportional (Figure 2E).

As shown above, the complexation of Cu^{2+} and modified nucleobase resulted in a signal shift and thus, it is most likely that the detection and quantification of metal ion by Raman spectra is feasible, but the detailed mechanism for the signal shift is unclear. Recent study revealed that the protonation at conjugated cytosine caused shrinkage of C-C triple bond, leading to Raman signal shift of acetylene.[12] We speculate that a similar conformational change may have occurred in this nucleobase, resulting in the Raman signal shift.

In light of these basic properties of **Ac₂-d^{Py}U**, we next characterized the specific complexation of Cu^{2+} with **d^{Py}U** in DNA. For this purpose, we prepared ODNs bearing **d^{Py}U** as shown in Figure 3A. After hydrolysis of **Ac₂-d^{Py}U** under basic conditions to remove two acetyl groups, the hydroxyl group at the 5'-side of compound **3** was selectively alkylated by DMTrCl. The resulting compound

4 was incorporated into DNA via phosphoramidite, using a DNA synthesizer. We prepared **ODN 1** bearing one modified uridine bearing ligand unit at the center of the strand. The synthesized **ODN 1** was identified by measurement of MALDI-TOF mass spectrometry. After the synthesis, we measured the Raman spectra of **ODN 1** in aqueous solution (Figure 3B). In the Raman spectra, one robust band was observed around 2210 cm^{-1}, which was assigned to acetylene units of **d^{Py}U** in the ODN. Thus, this spectrum supports the incorporation of **d^{Py}U** in the strand, and indicates that **d^{Py}U** could show a clear Raman signal even in the DNA strand. We also measured its Raman spectra in the presence of Cu^{2+} ions. When 1 equiv of Cu^{2+} was added to the solution of **ODN 1**, the signal shifted to the high wavenumber side, as with the monomeric **Ac₂-d^{Py}U**. These results strongly indicate that **ODN 1** is bound with Cu^{2+} ion at the **d^{Py}U** ligand unit to show its shifted Raman signal.

CONCLUSION

In conclusion, complexation between ligand and Cu^{2+} cations was tracked by monitoring changes in molecular vibrations. The nucleobase with Cu^{2+}-binding ligand, **d^{Py}U**, was designed and prepared, in which an acetylene unit was introduced as a reporter tag for the measurement of Raman spectra. Acetylated derivatives of **d^{Py}U** showed a band at 2209 cm^{-1} typical of acetylene, and its complexation with Cu^{2+} resulted in a Raman band shift, whereupon the wavenumber was increased by 6 cm^{-1}. Thus, the complexation with metal ions resulted in a band shift. We also prepared ODNs bearing **d^{Py}U** and applied them to the capture of Cu^{2+}. The ODNs showed a signal shift in the presence of Cu^{2+}, thus, we found that the ODNs also complexed with target metal ions to show a characteristic Raman signal. Modified ODNs have been used as functional biomolecules, which can be applied to molecular imaging, gene technologies, and gene therapies. The present system is promising as Raman probes for metal ions, and therefore, the application of the system to Raman imaging for cellular metal ions is in progress.

REFERENCES

(1) Schnitzler, T., Herrmann, A. *Acc. Chem. Res.* **2012**, *45*, 1419.

(2) Kwak, M., Herrmann, A. *Chem. Soc. Rev.* **2011**, *40*, 5745.

(3) Liu, K., Zheng, L., Ma, C., Göstl, R., Herrmann, A. *Chem. Soc. Rev.* **2017**, *46*, 5147.

(4) Huo, S., Li, H., Boersma, A. J., Herrmann, A. *Adv. Sci.,* **2019**, *6*, 1900043.

(5) Qiu, L., Wu, C., You, M., Han, D., Chen, T., Zhu, G., Jiang, J., Yu, R., Tan, W. *J. Am. Chem. Soc.*, **2013**, *135*, 12952.

(6) Meng, Z., Yang, J., Liu, Q., de Vries, J. W., Gruszka, A., Rodríguez-Pulido, A., Crielaard, B. J., Kros, A., Herrmann, A. *Chem. Eur. J.* **2017**, *23*, 9391.

(7) Kainuma, R., Motohashi, Y., Nishihara, T., Kurihara, R., Tanabe, K. *Org. Biomol. Chem.* **2020**, *18*, 5406.

(8) Yoshihara, K., Takagi, K., Son, A., Kurihara, R., Tanabe, K. *ChemBioChem*, **2017**, *18*, 1650.

(9) Larkin, P. *Infrared and Raman Spectroscopy*; Elsevier: **2011**.

(10) Fujioka, H., Shou, J., Kojima, R., Urano, Y., Ozeki, Y., Kamiya, M. *J. Am. Chem. Soc*. **2020**, *142*, 20701.

(11) Takemura, S., Watanabe, H., Nishihara, T., Okamoto, A., Tanabe, K. *RSC Advances*. **2020**, *10*, 36119.

(12) Itaya, R., Idei, W., Nakamura, T., Nishihara, T., Kurihara, R., Okamoto, A., Tanabe, K. *ACS Omega* **2021**, 6, 31595.

(13) Makanai, H., Nishihara, T., Tanabe, K. *ACS Appl. Nano Mater*. **2022**, 5, 2, 2935.

(14) Yamakoshi, H., Dodo, K., Okada, M., Ando, J., Palonpon, A., Fujita, K., Kawata, S., Sodeoka, M. *J. Am. Chem. Soc*., **2011**, *133*, 6102–6105.

(15) Dubois, R. J., Landee, C. P., Rademeyer, M., Turnbull, M. M. *J. Coord. Chem*. **2019**, *72*, 1785.

(16) Macial-Contreras, M., Daykin, K, L., Simmons, J. T., Allen, J. R., Hooper, Z. S., Davidson, M. W., Zhu, L. *Org. Biomol. Chem*. **2017**, *15*, 9139.

(17) Netzel, T. L., Zhao, M., Nafisi, K., Headrick, J., Sigman, M. S., Eaton, B. E. *J. Am. Chem. Soc*. **1995**, *117*, 9119.

Highly Fluorescent Isomorphic Nucleobase Analogs Based on the Thieno[3,4-*d*]-pyrimidine

Soyoung Park,[*,1] and Hiroshi Sugiyama[*,2]

[1]*Immunology Frontier Research Center, Osaka University, Yamadaoka, Suita, Osaka, 565-0871, Japan*
[2]*Institute for Integrated Cell-Material Sciences (iCeMS), Kyoto University, Yoshida-ushinomiyacho, Sakyo-ku, Kyoto 606-8501, Japan*

*Corresponding author:

Prof. Dr. Soyoung Park, Prof. Dr. Hiroshi Sugiyama
Tel.: (+)81-75-753-9765; Fax: (+)81-75-753-3670
E-mail: spark@ifrec.osaka-u.ac.jp, sugiyama.hiroshi.3s@ kyoto-u.ac.jp (H.S.)

KEYWORDS

fluorescent isomorphic nucleobase, thieno[3,4-d]-pyrimidine, B-Z transition, FRET pair

ABSTRACT

Fluorescent nucleobases are receiving attention as robust and useful probes to study nucleic acid structures and interactions with proteins. We have a long been engaged in the development and application of emissive isomorphic nucleobases. In this review, we introduce our research results focusing on fluorescent isomorphic nucleobase analogs based on the thieno[3,4-*d*]-pyrimidine and discuss their characteristic and application.

INTRODUCTION

Fluorescent probes are very powerful and convenient tools for detection and investigation of biomolecules, such as DNA, RNA, and proteins. Therefore, numerous efforts have been made to develop useful fluorescent probes. Since natural nucleobases are not fluorescent, the development of fluorescent nucleobase analogs is one of the important research subjects in chemical biology. Especially, the fluorescent isomorphic nucleobases that have fluorescent properties while maintaining a structural similarity as that of natural nucleobases have received much attention from the perspective of expanding the artificial genetic alphabet with various functions (1-7). In 1969, Stryer reported that a nucleobase analog, 2-Aminopurine (2AP, Figure 1), had a red-shifted absorption spectrum compared to the absorption spectrum of natural nucleobases, and that its fluorescence properties were strongly dependent on its surrounding environment (8). In the double-stranded DNA structure, the fluorescence of 2AP is apt to be quenched by interaction with neighboring bases, but its fluorescence increases when it becomes single-stranded or flips out of the double helix by interaction with proteins. 2AP has been widely used as a fluorescent probe to detect conformational changes and energy transfer within nucleic acids as well as the interactions between nucleic acids and proteins due to its similar structure and reactivity to enzymes compared to the natural adenine base. Starting with 2AP, large numbers of fluorescent nucleobase analogs have been developed.

This review is organized as personal account about fluorescent isomorphic nucleobase analogs based on the thieno[3,4-*d*]-pyrimidine. Thus, we summarize our work on the synthesis and utilization of DNA nucleoside derived from thieno[3,4-*d*]-pyrimidine and address the prospects of future application.
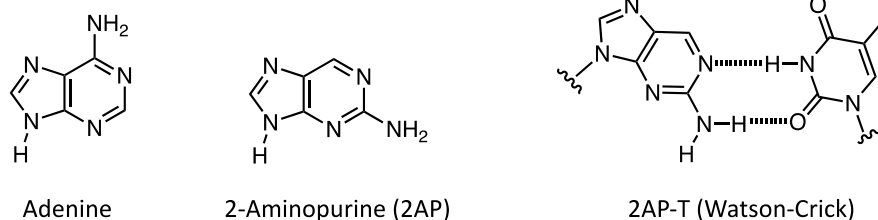

Figure 1. The chemical structure of adenine, 2-aminopurine (2AP) and hydrogen bonding of 2AP to T in Watson-Crick base pairing

1. thdG, 2-aminothieno[3,4-*d*]pyrimidine G-mimic deoxyribonucleoside

Original structures of nucleobases emit pointless fluorescence to use a chemical biology tool. Thus, chemical modification is necessary to endow fluorescence property. For this purpose, various fluorescent nucleobase analogs have been developed to gratify useful photophysical properties and isomorphic characteristic such as Watson–Crick base pairing. Recently, Tor and coworkers have developed the highly emissive and isomorphic RNA nucleosides derived from thieno[3,4-*d*]-pyrimidine and reported their remarkable photophysical features including visible light emission and a high quantum yield (9-11). This inspired us to exploit fluorescent DNA nucleosides based on a thienopyrimidine heterocycle (Figure 2). We turned on a guanine derivative because of

its important role in the structural dynamics of DNA such as the transition between B-DNA and Z-DNA. As scheme 1, we synthesized thdG, 2-aminothieno[3,4-*d*]pyrimidine G-mimic deoxyribonucleoside (12). The thienopyrimidine heterocycle was synthesized from the commercially available methyl 4-aminothiophene-3-carboxylate hydrochloride. Friedel–Crafts C-glycosylation at the C9 position of the thienoguanine afforded isomorphic guanine nucleoside analog. The fundamental photophysical properties of the thdG monomer are shown in Table 1. Similar to thG RNA nucleoside, thdG deoxyribonucleoside showed an absorption maximum at 349 nm and visible emission at 455 nm with a high quantum yield (0.58) in water. The phosphoramidite of thdG could be incorporated into DNA oligonucleotide and thermal denaturation experiment indicated that thdG could replace a G base with comparable thermodynamic stability and base pairing
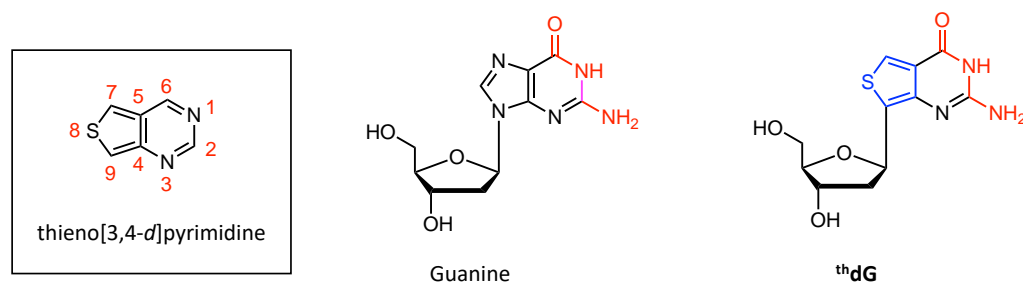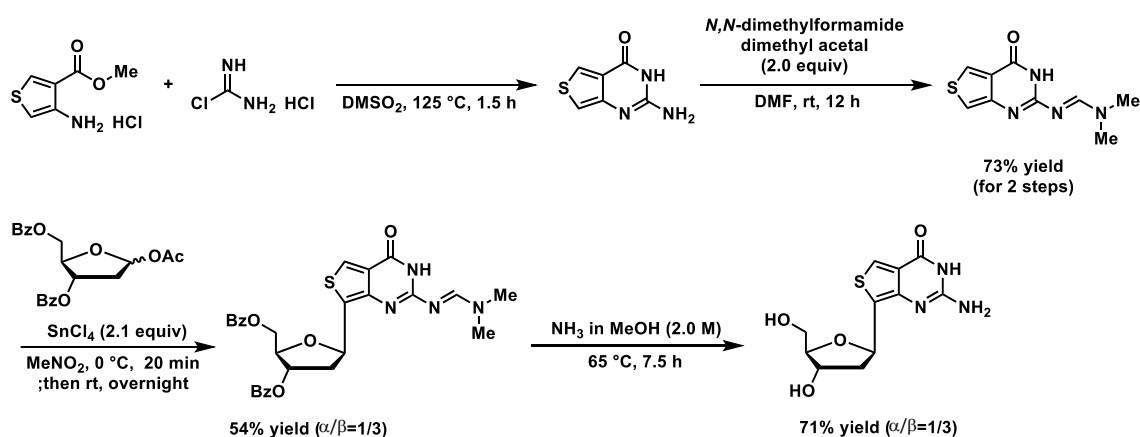

Figure 2. The chemical structures of thieno[3,4-*d*]pyrimidine, guanine and thdG

**Scheme 1**. Synthesis of thdG

selectivity (Figure 3).

It is known that Z-DNA has characteristic zigzag structure (four-base π-stacks). In 2003, we reported that B-Z transition could be detected by using the fluorescence change of 2-aminopurine within discrete four-base π-stacks in Z-DNA (13-14). Based on the isomorphicity and the photophysical properties of **thdG**, we exploited the utility of **thdG** to monitor the conformational changes between right-handed B-DNA and left-handed Z-DNA. Since **thdG** displays a tendency to prefer the anti-conformation and stabilizes B-form DNA in DNA duplex, we prepared the CG repeat DNA sequences containing m8G as a Z-stabilizing unit (15-17). The fluorescence of the self-complementary

dodecamer d(CGCXCYCGCG)₂ increased proportionally as the salt concentration increased (Figure 4). In addition, fluorescence of **thdG** could be applied to monitor DNA–protein interactions. Z-DNA-binding domain-containing proteins such as RNA adenosine deaminase (ADAR1) have received attention with relevance to their biological significance in gene regulation, innate immunity, and cancer diseases (18-23). We utilized a Zab domain of ADAR1. As shown in Figure 4c, when we added Zab into the solution of **thdG**-containing Z-DNA sequence, strong blue emission was observed with the naked eye. This indicates **thdG** can be used as a useful probe to detect the conformational changes and protein interactions.

Encouraged by practical photophysical properties

Table 1. Photophysical properties of **thdG**

solvent	λ_{abs}/nm (ε/$10^3M^{-1}cm^{-1}$)	λ_{em}/nm (ϕ)	$\phi\varepsilon$	τ/ns	Stokes shift/cm^{-1}
water	349 (4.26)	455 (0.58)	2471	20.5	9370
dioxane	329 (5.37)	429 (0.85)	4565	14.0	7085
MeOH	327 (3.80)	460 (0.47)	1786	13.7	8842
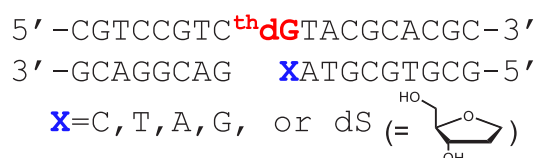
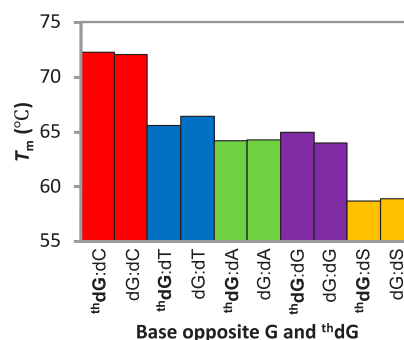|	thdG:dC	thdG:dT	thdG:dA	thdG:dG	thdG:dS
T_m (°C)	72.3	65.6	64.2	65.0	58.9

Figure 3. Thermal stability and selectivity of base pairing of **thdG**
Reproduced with permission from ref. 12. Copyright 2014 The Royal Society of Chemistry

of **thdG**, we investigated to enzymatic incorporation by naturally occurring enzymes and replication systems. We have synthesized a visible fluorescent nucleoside triphosphate, **thdGTP** based on published procedures (Scheme 2).

Primer extension assays with KF polymerase showed that **thdGTP** could be incorporated into the opposite site to cytosine like native GTP (24). Full-length products were observed as blue bands in the unstained gel without the aid of the FAM-labeled primer (Figure 5). We also investigated the performance of **thdGTP** for PCR amplification of much longer templates which contain numbers of cytosines. We found that it was difficult to incorporate proximal **thdGTP** into the DNA strand consecutively and thus conducted PCR amplification using a mixture of dGTP and **thdGTP**. PCR amplification of 298-, 480-, and 761-mer DNA using pGEM or pUC18 plasmids afforded the desired length of fluorescent PCR product labeled by **thdGTP** (Figure 6). The results demonstrate that highly emissive **thdGTP** can be recognized by natural DNA polymerases and amplified as a surrogate of natural dGTP. Further application of **thdGTP** is expected such as the construction of fluorescent DNA nanostructures and in vivo fluorescent imaging.
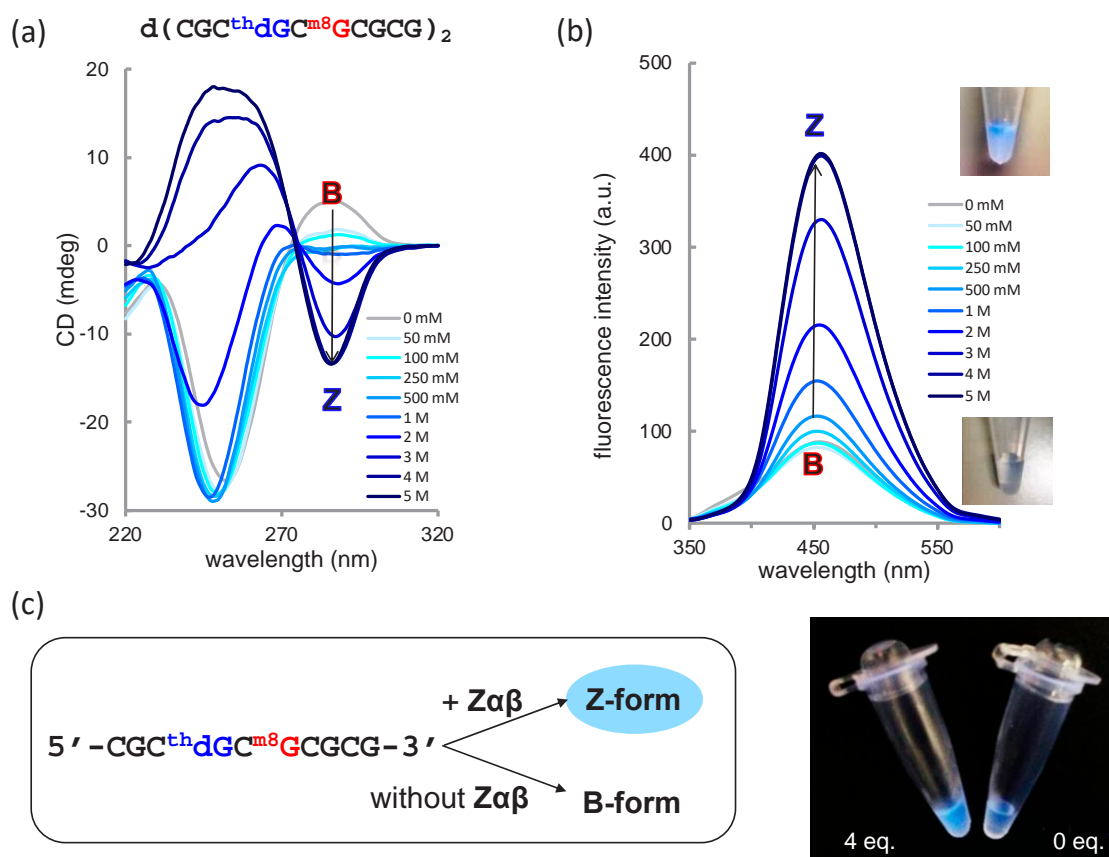
Figure 4. Detection of the conformational changes from B-DNA to Z-DNA through changes in fluorescence intensity (a) observation of the B–Z transition by CD spectroscopy. (b) Change of fluorescence of $NaClO_4$ at 5 °C. Samples contained 5 µM of oligonucleotides in 20 mM sodium cacodylate buffer (pH 7.0). The photo was taken under UV irradiation. (c) Visual detection of B–Z transition by Zαβ interaction. 4 eq. (left) or 0 eq. (right) of Zαβ was added to 1.3 µM of ODN9 and 100 mM of NaCl in 20 mM Tris-HCl buffer (pH 7.5). After incubation at 37 °C for 30 min, the photo was taken under UV irradiation. Reproduced with permission from ref. 12. Copyright 2014 The Royal Society of Chemistry
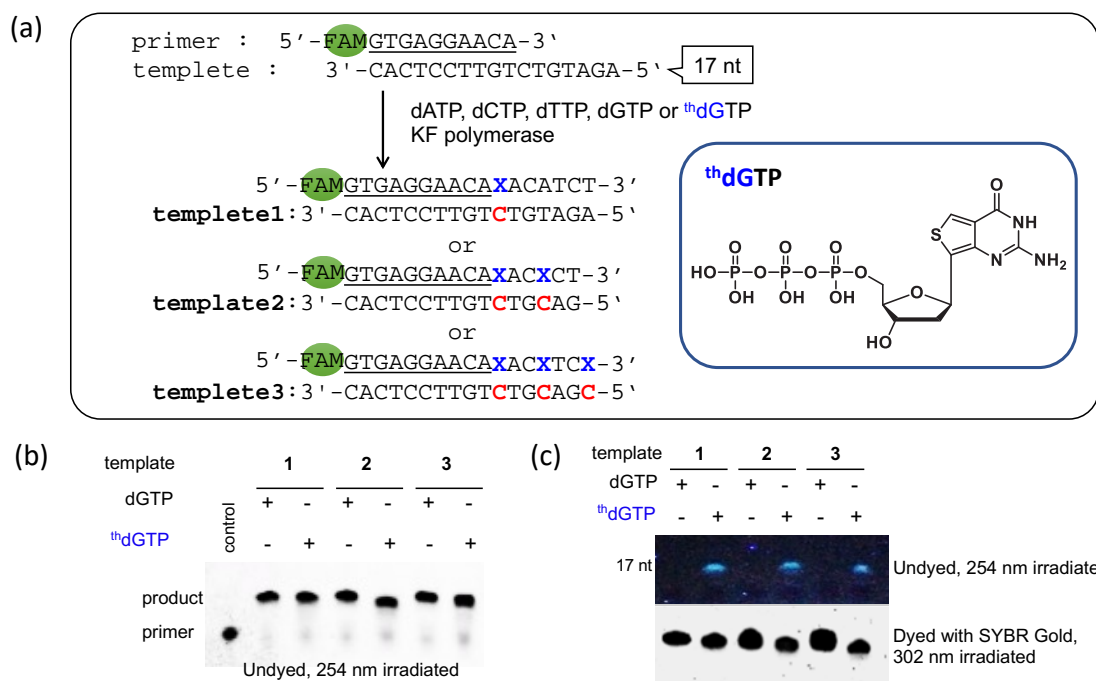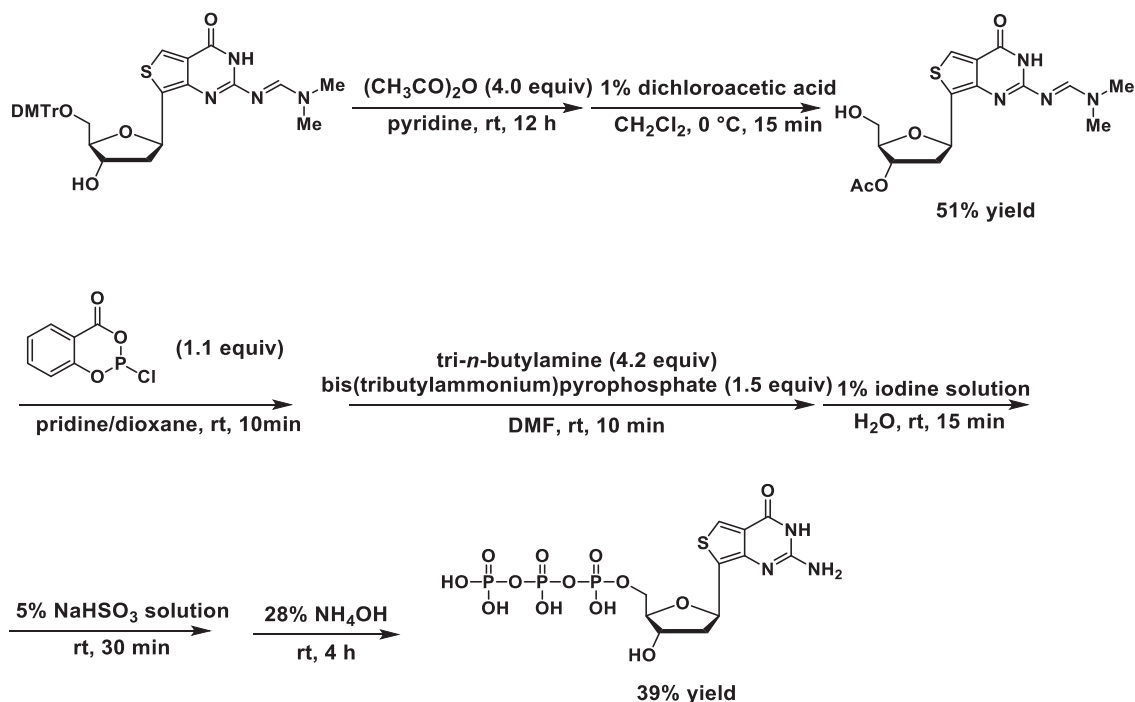
Scheme 2. Synthesis of **ᵗʰdGTP**

(a)

```
primer :  5'-FAMGTGAGGAACA-3'
templete :   3'-CACTCCTTGTCTGTAGA-5'   17 nt

        dATP, dCTP, dTTP, dGTP or ᵗʰdGTP
        KF polymerase

        5'-FAMGTGAGGAACAXACATCT-3'
templete1:3'-CACTCCTTGTCTGTAGA-5'
                    or
        5'-FAMGTGAGGAACAXACXCT-3'
templete2:3'-CACTCCTTGTCTGCAG-5'
                    or
        5'-FAMGTGAGGAACAXACXTCX-3'
templete3:3'-CACTCCTTGTCTGCAGC-5'
```

ᵗʰdGTP

(b)

Undyed, 254 nm irradiated

(c)

Undyed, 254 nm irradiated

Dyed with SYBR Gold, 302 nm irradiated

Figure 5. (a) Primer extension experiments with 17-mer templates **1–3**, in the presence of either natural dGTP or **ᵗʰdGTP** and three dNTPs (dATP, dTTP, and dCTP). (b) Analyses by denaturing gel electrophoresis of primer-extended products with each template after 30 min incubation at 37 °C. Lane 'control' corresponds to incubation with a mixture of template, primer, and dNTPs without the Klenow fragment. (c) Analyses by denaturing gel electrophoresis of primer-extended products using primer without FAM labeling.
Reproduced with permission from ref. 24. Copyright 2014 The Royal Society of Chemistry
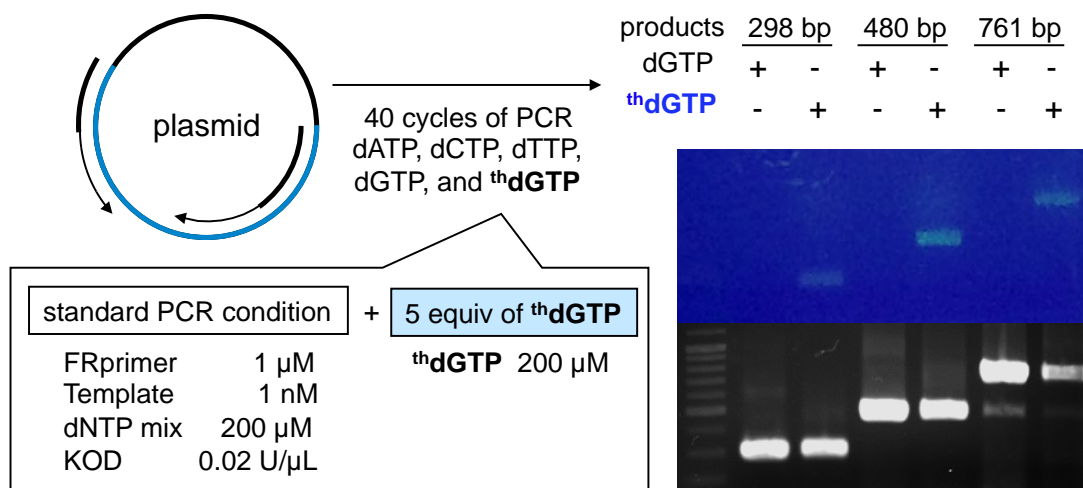
Figure 6. **ᵗʰdG** labeling for long fluorescent DNA. Analyses by agarose gel electrophoresis of PCR-amplified products; **ᵗʰdGTP** (5 equiv, 1 mM) was added to 200 μM dNTPs (dCTP, dTTP, dATP, and dGTP) and standard PCR reaction mixture. Photograph taken (top) under 254 nm irradiation before staining, and (bottom) after staining with ethidium bromide. Reproduced with permission from ref. 24. Copyright 2014 The Royal Society of Chemistry

2'-*OMe*-ᵗʰG, highly emissive 2'-*O*-methylated G analog

2'-*O*-methylation is a naturally occurring modification of RNA and it could be found in tRNA and small RNAs. 2'-*O*-Methyl-modification of oligonucleotides is the most commonly used strategy for antisense medicinal chemistry, aptamer-based diagnostics and therapeutics because 2'-*O*-methyl-modified RNA afforded higher nuclease resistance and binding affinity to target compared to unmodified oligonucleotides. In this context, we synthesized a highly emissive 2'-*O*-methylated G analog, 2'-*OMe*-ᵗʰG according to our previous study (25). The photophysical properties of 2'-*OMe*-ᵗʰG is similar to ᵗʰdG and shows absorption maximum at 320 nm and visible emission at 457 nm with a high quantum yield of 0.652 in water. The phosphoramidite of 2'-*OMe*-ᵗʰG could be incorporated into DNA oligonucleotides of 5'-d(CGTCCGTCXTACGCACGC)-3' by automated solid-phase synthesis. DNA duplexes containing 2'-*OMe*-ᵗʰG–C base pair showed almost identical thermal stability (T_m 72.1 °C) compared with that of native a G–C base pair (T_m 72.1 °C). The base pairing selectivity was also observed through thermal denaturation experiment (Figure 7). For ᵗʰdG, we found that the B–Z transition became more difficult when ᵗʰdG was incorporated in place of a dG and

used a Z-stabilizing unit such as 8-methylguanine (m8G) to induce B-Z transition. The oligonucleotide containing 2'-*OMe*-ᵗʰG could convert to Z conformation without the help of a Z-DNA inducer and increase the fluorescence with increasing $NaClO_4$ concentration. Interestingly, B-Z transition could be modulated by temperature as well as high salt conditions and these features have been applied to develop DNA-based switching devices (13-14). Since 2'-*OMe*-ᵗʰG outperformed in B-Z transition with useful photophysical properties, we thought out that the equilibrium between B-DNA and Z-DNA could be controlled by temperature leading to change in fluorescence. We devised a visible DNA nanothermometer and observed that the fluorescence intensity of 2'-*OMe*-ᵗʰG-containing oligonucleotides changed relying on the temperature as its B–Z transition occurred (Figure 8). Strong fluorescence enhancement was observed at 5 °C by Z-conformation, whereas the fluorescence intensity decreased at 40 °C by the increased B-conformation. The fluorescence change could be reproducible according to the change in the proportion of Z- and B-DNA under repetitive temperature cycles. A visible nanothermometer based on photophysical property of 2'-*OMe*-ᵗʰG and DNA conformational change will be exploited for the development of biocompatible nanodevices to monitor the temperature in an intracellular environment.
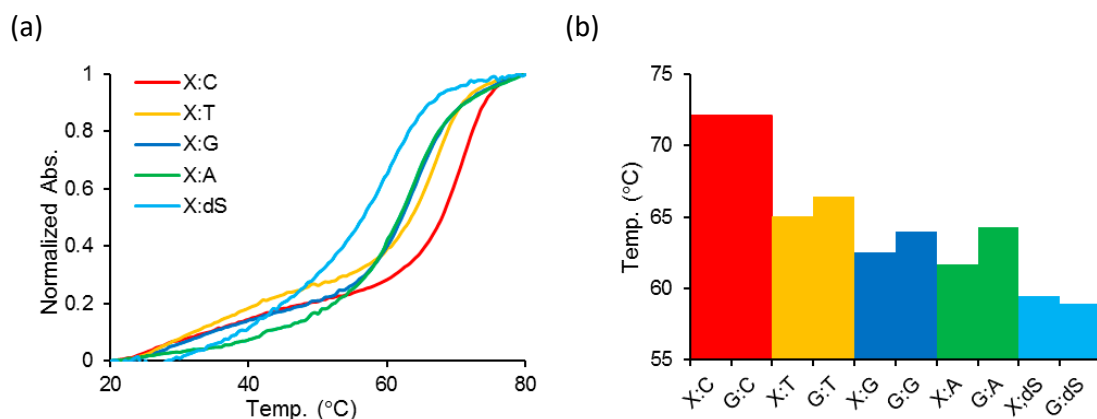
(a)

(b)

Figure 7. Fidelity of 2'-*OMe*-**th**G against canonical bases. (a) Thermal melts of oligonucleotides: 5'–CGTCCGTCXTACGCACGC–3' (X = 2'-*OMe*-**th**G) and complementary strand, 5'–GCGTGCGTAYGACGGACG–3' (Y = C, T, A, G, or dSpace, 2'-*OMe*-**th**G). (b) Comparison of T_m values. All samples contained 5 μM of each oligonucleotide strand, 20 mM Na cacodylate (pH 7.0), and 100 mM NaCl.

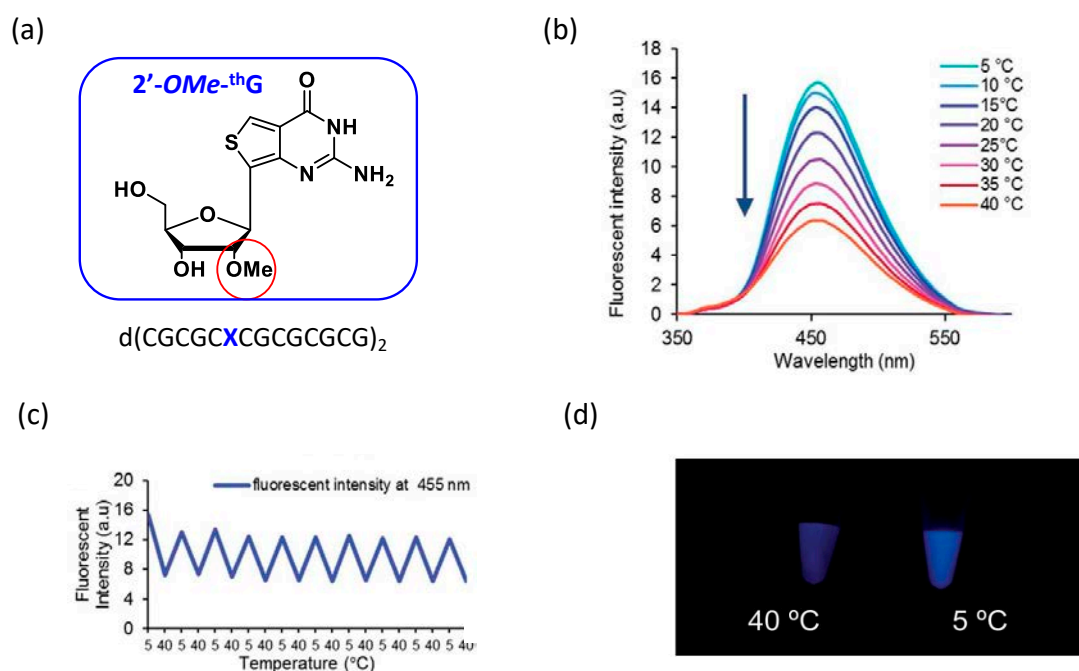Reproduced with permission from ref. 25. Copyright 2015 The Royal Society of Chemistry

(a)

(b)

(c)

(d)

Figure 8. Visible nanothermometer using 2'-*OMe*-**th**G. (a) Chemical structure of 2'-*OMe*-**th**G (b) Change in fluorescence intensity by temperature. (c) Repeated experiments showing fluorescence emission at 5 °C and 40 °C. (d) Photo of visible nanothermometer. Samples contained 5 μM of ODN9 in 20 mM sodium cacodylate buffered (pH 7.0) 3.5 M NaClO₄. The photo was taken under UV (365 nm) irradiation.

Reproduced with permission from ref. 25. Copyright 2015 The Royal Society of Chemistry

3. *th*dT, thieno[3,4-*d*]pyrimidine T-mimic deoxyribonucleoside

The comparable resemblance and noteworthy photophysical properties of **th**dG and 2'-*OMe*-**th**G to the native nucleosides steered us to expand the utility of the emissive DNA nucleoside analogs containing a thieno[3,4-*d*]-pyrimidine core. We synthesized thieno[3,4-*d*]-pyrimidine T-mimic deoxynucleoside, **th**dT, and a thio-analogue of thymidine triphosphate, **th**dTTP, as shown scheme 3 (26). The fundamental photophysical properties of **th**dT were summarized in Table 2. The **th**dT deoxyribonucleoside has an absorption maximum at 303 nm and the emission maxima are shifted toward a shorter wavelength as a visible fluorescence at 420 nm in water. **th**dT phosphoramidite could be readily incorporated into oligonucleotides by the automated solid-phase synthesis. In thermal denaturation assays, DNA duplexes including the **th**dT-A base pair indicated a comparable thermal stability to that of a duplex with a native T-A base pair and competent base pairing selectivity (Figure 9a and 9b). We investigated fluorescence features of DNA duplexes containing **th**dT and found that the fluorescence intensity significantly increased when a **th**dT-containing DNA strand was hybridized with a complementary strand having an abasic site opposite **th**dT (Figure 9c). It suggests that **th**dT can be used as a fluorescent probe to monitor a formation of an abasic site in DNA duplexes related with base-excision repair system. Based on the previous study of **th**dTTP we verified the utility of **th**dTTP for enzymatic incorporation. The primer extension assays showed that **th**dTTP could be incorporated as a complementary nucleotide to an adenine residue by using KF polymerase (Figure 10). Like **th**dGTP, the result indicated that the incorporation of **th**dT was difficult in the presence of consecutive adenine residues. Therefore, we performed PCR amplification using a mixture of dTTP and **th**dTTP to complement the inadequate incorporation of **th**dT. A 298-mer PCR amplification using KOD Plus polymerase gave a desired PCR product with assistance from native dTTP and the content of **th**dTTP was confirmed by the enzyme digestion and HPLC analysis (Figure 11). This suggests show the potential of **th**dT as a fluorescent thymidine surrogate for further applications.
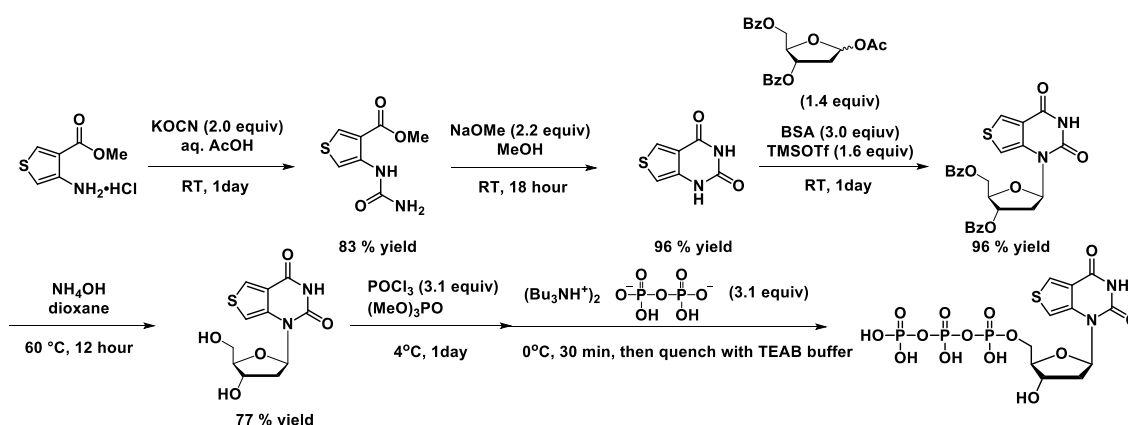
Scheme 3. Synthesis of **th**dT and **th**dTTP

Table 2. Photophysical properties of **th**dT

solvent	λ_{abs}/nm (ε/10^{3}M^{-1}cm^{-1})	λ_{em}/nm (ϕ)	$\phi\varepsilon$	τ/ns	Stokes shift/cm^{-1}
water	303 (3.10)	420 (0.58)	1798	15.1	9194
dioxane	308 (3.59)	360 (0.11)	395	10.4	4690
MeOH	304 (2.98)	414 (0.42)	1252	9.7	8740

ODN1-2: 5'-CGTCCGTC**X**TACGCACGC-3' **X**= **ᵗʰdT** or T
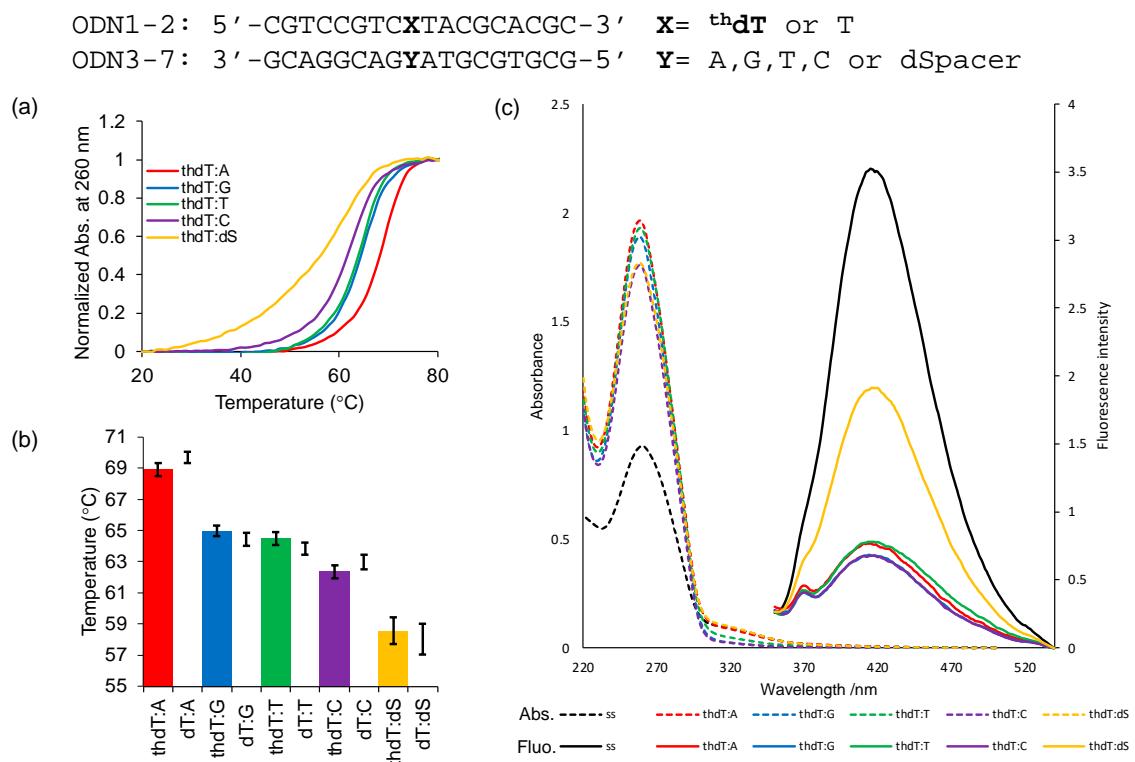ODN3-7: 3'-GCAGGCAG**Y**ATGCGTGCG-5' **Y**= A,G,T,C or dSpacer

Figure 9. Thermal stability and selectivity of base pairing. (a) Thermal melts of **ᵗʰdT** containing DNA. Oligonucleotides: 5'-CGTCCGTC**ᵗʰdT**TACGCACGC-3' paired with complementary strand: 5'-GCGTGCGTA**Y**GACGGACG-3' **Y** = A, T, C, G, or dSpacer. (b) Comparison of T_m values. (c) Absorbance (dashed lines) and fluorescence properties (solid lines) of DNA duplexes containing matched or mismatched bases. All samples contained 5 μM of each oligonucleotide strand, 20 mM Na cacodylate (pH 7.0) and 100 mM NaCl. Excitation at 325 nm.
Reproduced with permission from ref. 26. Copyright 2017 The Chemical Society of Japan
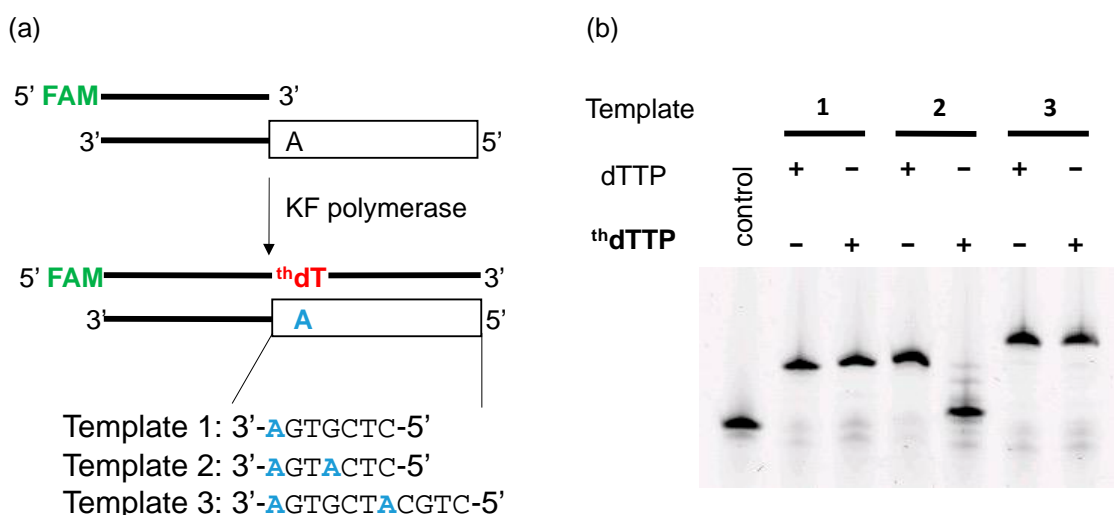
Figure 10. (a) Primer extension experiments with a FAM-labeled primer and template **1** to **3**, in the presence of the natural dTTP or **ᵗʰdTTP,** and three dNTPs (dATP, dGTP and dCTP). (b) Analyses of primer-extended products by denaturing gel electrophoresis.
Reproduced with permission from ref. 26. Copyright 2017 The Chemical Society of Japan
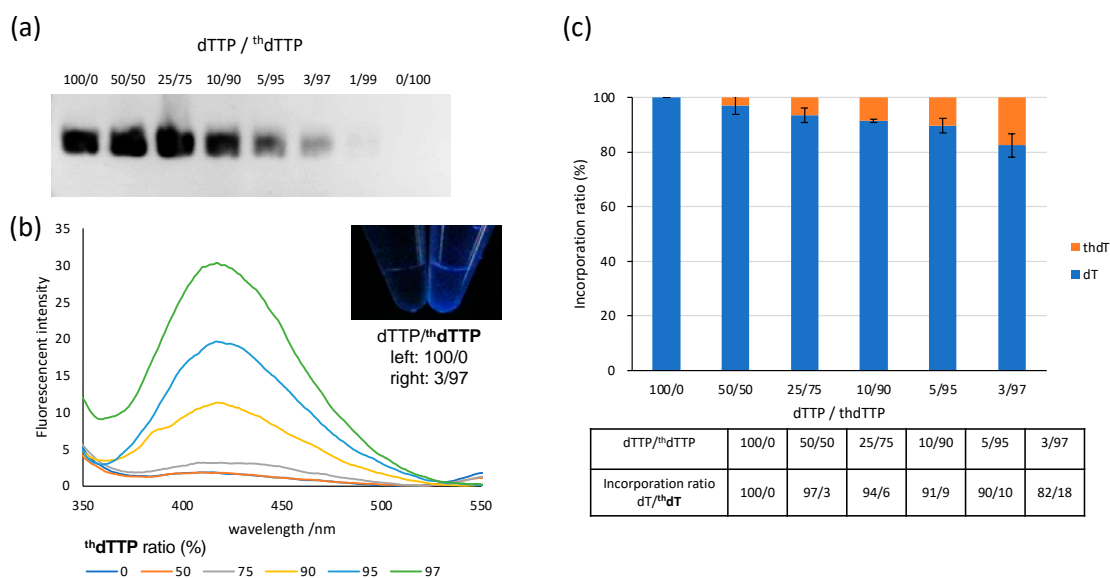
Figure 11. (a) Analyses by agarose gel electrophoresis of amplified 298 bp products. PCR amplification was performed with dATP, dCTP, and dGTP (200 μM each) and a combined total of 200 μM dTTP and **thdTTP** mixture (100/0, 50/50, 25/75, 10/90, 5/95, 3/97, 1/99, and 0/100). (b) Fluorescence spectra of purified DNA solutions obtained as described in (a) from dTTP/**thdTTP** ratios. All samples contained 30 ng/μL DNA. The excitation wavelength was 303 nm. (c) Relationship between the dTTP/**thdTTP** ratio and the extent of **thdT** incorporation. Averages of more than two runs.

4. Application of thdG as a donor in FRET pair

Förster resonance energy transfer (FRET) is a physical phenomenon in which the energy of an excited fluorescent molecule (donor) is transferred nonradiatively to another fluorescent molecule (acceptor). In the case of the fluorescence spectrum of the donor and the absorption spectrum of the acceptor significantly overlap, when two fluorescent molecules are in close proximity, the energy emitted by the excited donor is transferred and the fluorescence of the acceptor is observed instead of the fluorescence from the donor. The FRET efficiency depends on the distance between the donor and acceptor and the orientation factor. It is inversely proportional to the sixth power of the distance if the orientation factor is not considered, and this makes FRET a useful tool for measuring intermolecular distance and conformational changes (27-29). In the general FRET system to study nucleic acids, the fluorophores are introduced through flexible linkers, and the orientation factor cannot be subjected to the calculation of FRET efficiency due to the free rotation of the fluorophore. In this context, researchers have developed useful approaches to construct orientation-dependent FRET system in DNA helixes. For instance, Kato et al. developed a FRET system by incorporation of pyrene and perylene as a donor–acceptor pair using a D-threoninol linker and reported orientation-controlled FRET efficiency (30). Wilhelmsson and co-workers reported on the first nucleobase-analogue FRET pair which consists of 1,3-diaza-2-oxophenoxazine (tC^O) as the energy donor and 7-nitro-1,3-diaza-2-oxophenothiazine (tC$_{nitro}$) as the energy acceptor (31). Despite of its remarkable orientation-dependent FRET efficiency, the lack of fluorescence of tC$_{nitro}$ arouses the need for improvement. We focused on the practical
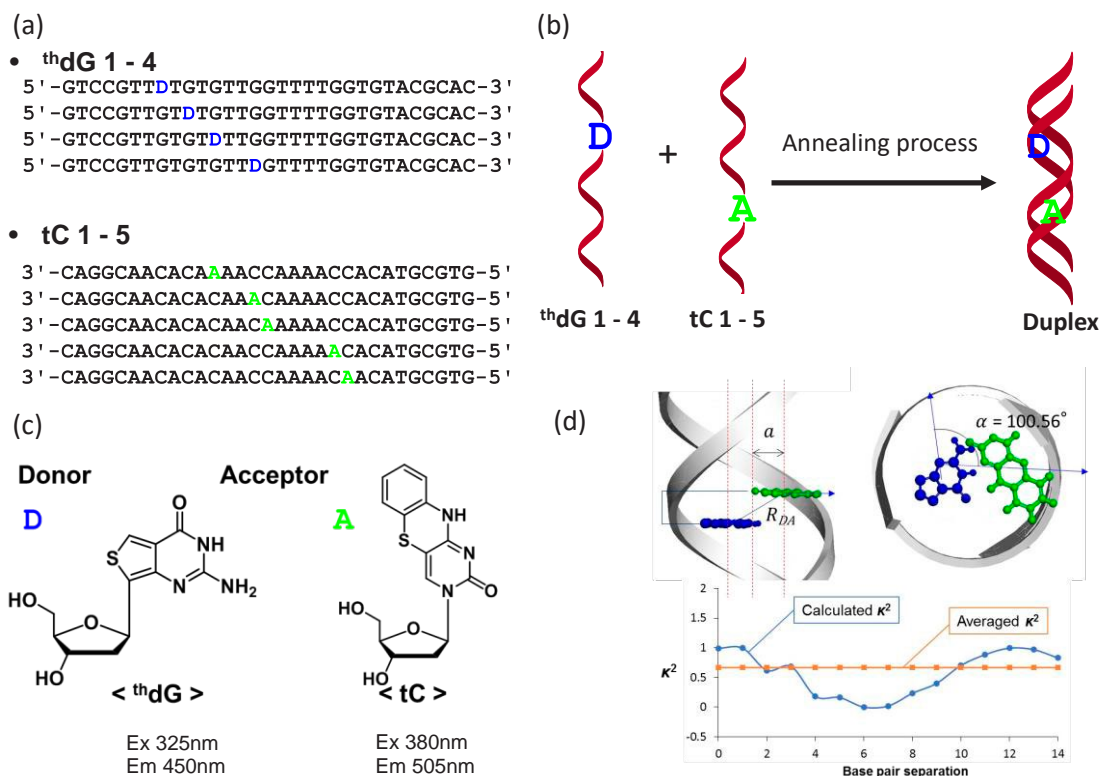
Figure 12. (A) Designed oligonucleotides for FRET study. (b) Conceptual illustration of **thdG**- and **tC**-containing duplexes for 0 and 14 base pair separations. (c) Chemical structures of **thdG** (donor) and **tC** (acceptor). (d) Orientation factors between **thdG** and **tC** were calculated as either fixed transition dipole moments obtained by Gaussian 09W (blue line with circle symbols) or as freely rotating transition dipole moments (orange line with square symbols).
Reproduced with permission from ref. 32. Copyright 2017 John Wiley and Sons.
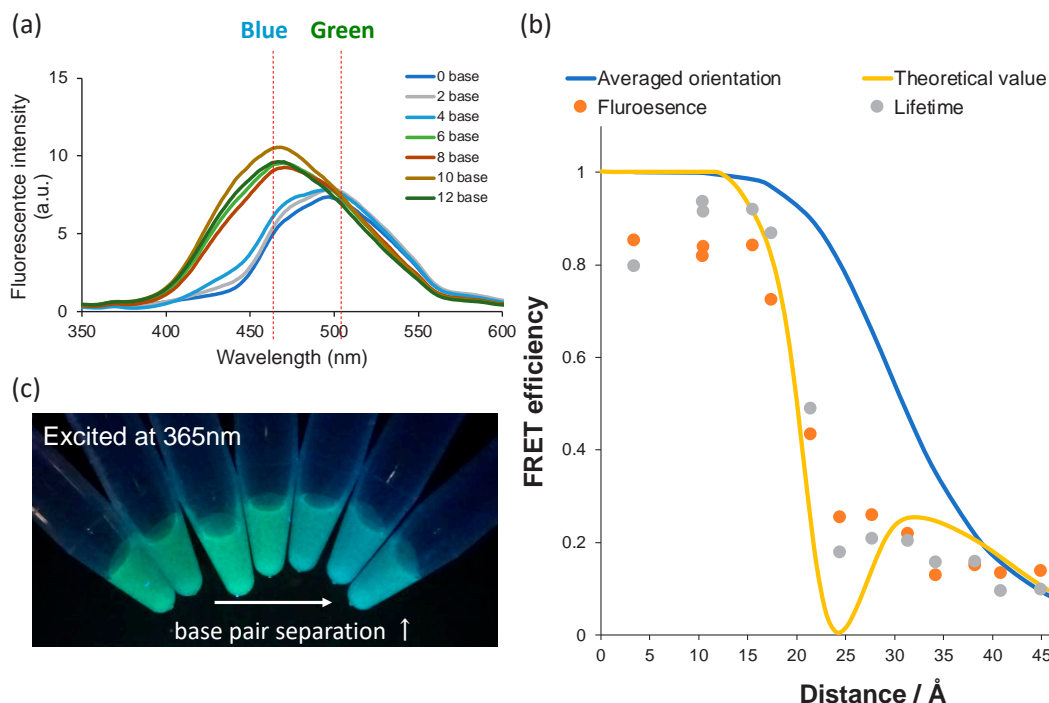
Figure 13. (a) Fluorescence spectra of **thdG**- and **tC**-modified DNAs excited at 325 nm. (b) FRET efficiency calculated from steady-state fluorescence (orange dots) and time-resolved fluorescence (gray dots). The theoretical value was derived from the calculated orientation factors (yellow line) and the averaged orientation factors (blue line). (c) Photograph of samples excited at 365 nm. The samples with 0, 3, 5, 7, 9, 11, and 13 base pair separations are arranged from left to right. All samples contained 5 μM of each oligonucleotide strand, 25 mM phosphate buffer (pH 7.5), and 100 mM NaCl.
Reproduced with permission from ref. 32. Copyright 2017 John Wiley and Sons.

photophysical property and isomorphicity of th**dG** and 2'-*OMe*-th**G** for the establishment of a new FRET system with nucleobase analogs. We utilized two fluorescent isomorphic nucleobase analogs, th**dG** as the energy donor and tC as the energy acceptor and devised a Watson–Crick base-pairable FRET pair based on their satisfiable spectral overlap (32). We synthesized 31-mer oligonucleotides containing th**dG** and tC in different positions to systematically control donor and acceptor separations from 0 to 14 base pairs (Figure 12). After confirmation of thermal stability of DNA duplexes containing th**dG**-tC pair, we measured fluorescence spectra and fluorescence lifetime to study the FRET efficiency of the th**dG** –tC pair inside DNA.

Fluorescence spectra of th**dG**- and tC-modified DNA showed green fluorescence of tC acceptor when the base-pair separation was short. Whereas the fluorescence gradually changed from green to blue fluorescence of th**dG** donor as the distance between donor and acceptor

increased. We calculated FRET efficiency from steady-state fluorescence and time-resolved fluorescence. Theoretical values were calculated considering the averaged orientation factors and variable orientation of th**dG** and tC, respectively (Figure 13). Although there were some unconformities between the experimental FRET efficiencies and the theoretical values, the results indicated that devised th**dG**–tC FRET pair in DNA helix was obviously controlled by orientation factors as well as distance. Furthermore, we utilized the th**dG**–tC FRET pair for in situ visualization of the B–Z transition. When we used hairpin type oligonucleotide with a 6-base-pair separation between 2'-*OMe*-th**G** and tC, we observed the emission maximum shift from 480 nm to 458 nm as NaClO$_4$ concentration increased (Figure 14). This result indicated that the FRET efficiency varied depending on the contribution of orientation factor by DNA conformational change from B- to Z-form.
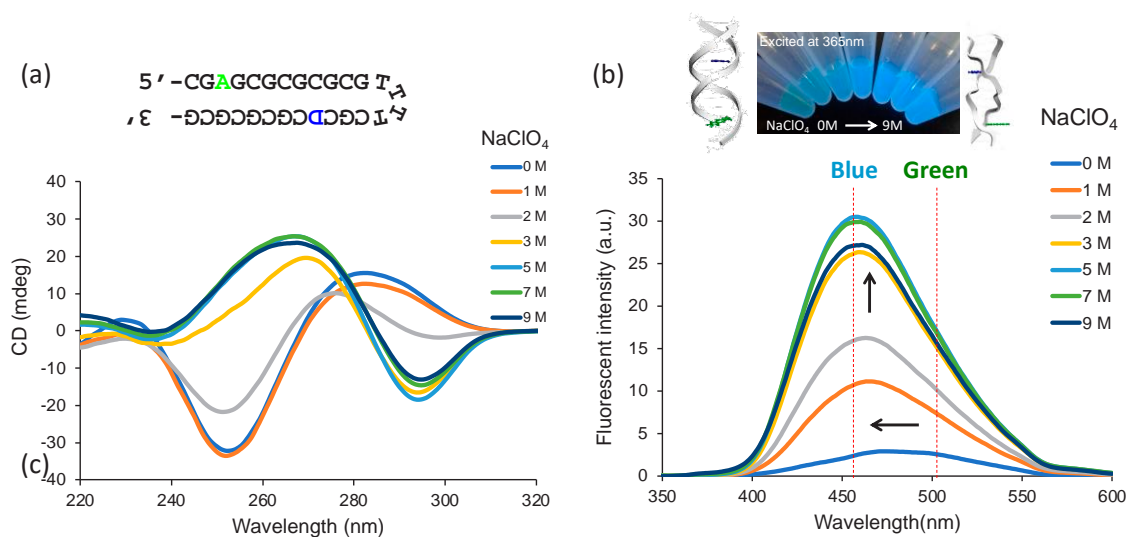

Figure 14. (a) CD spectroscopy about conformational changes from B-DNA to Z-DNA at various NaClO$_4$ concentrations (0 M, 1 M, 2 M, 3 M, 5 M, 7 M, and 9 M). (b) fluorescence intensity and photograph of samples under UV (365 nm) irradiation for 6-base-pair separations. All samples were prepared at 5 μM in 20 mM sodium cacodylate buffer (pH 7.0) at 5 °C. Reproduced with permission from ref. 32. Copyright 2017 John Wiley and Sons.

A potential of distance- and orientation factor-dependent **thdG**–tC FRET system led us to further application. We applied **thdG**–tC FRET pair to nucleosome to help understanding a geometric DNA model on nucleosome in gene regulation processes. We selected Widom 601 145 bp DNA sequence and prepared nucleosomal DNA labeled with **thdG** at the 40th nucleotide in the top strand and at the 27th or 41st nucleotide in the bottom strand by PCR amplification using **thdG** or tC-modified primer (33). After reconstitution with histone octamer, we measured steady-state fluorescence and evaluated FRET efficiencies based on the specific position of **thdG**–tC FRET pair. As shown Figure 15, nucleosome with D40th+A41st afforded FRET efficiency as 0.10. Meanwhile, higher FRET efficiency (0.25) was obtained with nucleosome containing D40th+A27th. Considering only distance with averaged orientation factor, FRET efficiencies of the nucleosome with D40th+A41st and D40th+A27th was calculated to be 0.04 and 0.57, respectively. This indicates that FRET efficiency of **thdG**–tC pair is highly dependent on the orientation factor in the nucleosome. **thdG**–tC FRET system can be a versatile tool to investigate conformational change of nucleosomal DNA by biochemical reaction during genetic processes.
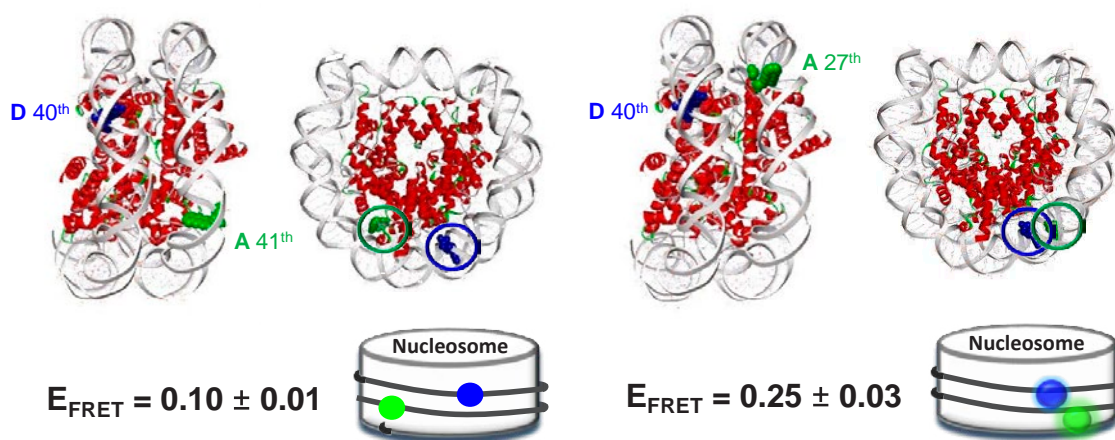

Figure 15. Schematic illustration of positions of donor and acceptor on nucleosome (Protein Data Bank code 3LZ0). Donor and acceptor are shown in a blue and green CPK representation. Calculated FRET efficiencies of two nucleosome (D 40th + A 41st or D 40th + A 27th) with mean errors. The FRET efficiencies were checked in triplicate. Reproduced with permission from ref. 32. Copyright 2018 John Wiley and Sons.

Conclusion and Perspectives

We started our step to develop practical fluorescent nucleobases to fulfil both comparable resemblance and significant photophysical properties. For this purpose, thieno[3,4-*d*]-pyrimidine heterocycle was very attractive structural motif and enabled us to establish various fluorescent approaches for the investigation of nucleic acids of interest. Hundreds of fluorescent nucleobases have been reported; however, this research area requires new nucleobase probes possessing high quantum yields and red-shifted absorption and emission wavelength for in-vivo study. We continue our efforts to design and synthesis new highly emissive isomorphic nucleobases with in-depth implementations supported by computational approach (34-38).

Conflicts of interest

There are no conflicts to declare.

Acknowledgements

References

1. Rist, M. J., Marino, J. P. Fluorescent Nucleotide Base Analogs as Probes of Nucleic Acid Structure, Dynamics and Interactions. *Curr. Org. Chem*. 2002; *6*; 775–793.

2. Wilhelmsson, L. M. Fluorescent Nucleic Acid Base Analogues. *Quart. Rev. Biophy*. 2010; *43*; 159–183.

3. Tanpure, A. A., Pawar, M. G., Srivatsan, S. G. Fluorescent Nucleoside Analogs: Probes for Investigating Nucleic Acid Structure and Function. *Isr. J. Chem*. 2013; *53*; 366–378.

4. Xu, W., Chan, K. M., Kool, E. T. Fluorescent Nucleobases as Tools for Studying DNA and RNA.

Nat. Chem. 2017; *9*; 1043–1055.

5. Hocek, M., Fojta, M. Nucleobase Modification as Redox DNA Labelling for Electrochemical Detection. *Chem. Soc. Rev.* 2011; *40*; 5802–5814.

6. Dai, N., Kool, E.T. Fluorescent DNA-Based Enzyme Sensors. *Chem. Soc. Rev.* 2011; *40*; 5756–5770.

7. Sinkeldam, R. W., Greco, N. J., Tor, Y. Fluorescent Analogs of Biomolecular Building Blocks: Design, Properties, and Applications. *Chem. Rev.* 2010; *110*; 2579–2619.

8. Ward, D. C. Reich, E. Stryer, L.Fluorescence Studies of Nucleotides and Polynucleotides. *J. Biol. Chem.* 1969; *244*; 1228–1237.

9. Shin, D., Sinkeldam, R. W., Tor, Y. Emissive RNA Alphabet. *J. Am. Chem. Soc.* 2011; *133*; 14912–14915.

10. Noé, M. S., Sinkeldam, R. W., Tor, Y. Oligodeoxynucleotides Containing Multiple Thiophene-Modified Isomorphic Fluorescent Nucleosides. *J. Org. Chem.* 2013; *78*; 8123–8128.

11. Rovira, A. R., Fin, A., Tor, Y. Expanding a Fluorescent RNA Alphabet: Synthesis, Photophysics and Utility of Isothiazole-Derived Purine Nucleoside Surrogates. *Chem. Sci.* 2017; *8*; 2983–2993.

12. Park, S., Otomo, H., Zheng, L., Sugiyama, H. Highly Emissive Deoxyguanosine Analogue Capable of Direct Visualization of B-Z Transition. *Chem. Commun.* 2014; *50*; 1573–1575.

13. Tashiro, R., Sugiyama, H. A Nanothermometer Based on the Different π-stackings of B- and Z-DNA. *Angew. Chem. Int. Ed.* 2003; *42*; 6018–6020

14. Tashiro, R., Sugiyama, H. Biomolecule-based Switching Devices that Respond Inversely to Thermal Stimuli. *J. Am. Chem. Soc*. 2005; *127*; 2094–2097.

15. Sugiyama, H., Kawai, K., Matsunaga, A., Fujimoto, K., Saito, I., Robinson, H., Wang, A. H.-J. Synthesis, Structure and Thermodynamic Properties of 8-Methylguanine-containing Oligonucleotides: Z-DNA under Physiological Salt Conditions. *Nucleic Acids Res.* 1996; *24*; 1272–1278.

16. Xu, Y., Ikeda, R., Sugiyama, H. 8-Methylguanosine: a Powerful Z-DNA Stabilizer. *J. Am. Chem. Soc.* 2003; *125*; 13519–13524.

17. Chen, F. Y.-H., Park, S., Otomo, H., Sakashita, S., Sugiyama, H. Investigation of B-Z Transitions with DNA Oligonucleotides Containing 8-Methylguanine. *Artificial DNA: PNA & XNA* 2014; *5*; e28226.

18. Rich, A., Zhang, S. Z-DNA: the Long Road to Biological Function. *Nat. Rev. Genet.* 2003; *4*; 566–572.

19. Nakahama, T., Kawahara, Y. Deciphering the Biological Significance of ADAR1–Z-RNA Interactions. *Int. J. Mol. Sci.* 2021; *22*; 11435.

20. Kuriakose, T., Kanneganti, T.-D. ZBP1: Innate Sensor Regulating Cell Death and Inflammation. *Trends Immunol.* 2018; *39*; 123–134.

21. Herbert, A. Z-DNA and Z-RNA in Human Disease. *Commun. Biol.* 2019; *2*; 7.

22. Jiao, H., Wachsmuth, L., Kumari, S., Schwarzer, R.; Lin, J., Eren, R. O., Fisher, A., Lane, R., Young, G. R., Kassiotis, G., Kaiser, W. J., Pasparakis, M. Z-Nucleic-acid Sensing Triggers ZBP1-Dependent Necroptosis and Inflammation. *Nature* 2020; *580*; 391–395.

23. Hao, Y., Yang, B., Yang, J., Shi, X., Yang, X., Zhang, D., Zhao, D., Yan, W.; Chen, L., Zheng, H., Zhang, K., Liu, X. ZBP1: a Powerful Innate Immune Sensor and Double-edged Sword in Host Immunity. *Int. J. Mol. Sci.* 2022; *23*; 10224.

24. Otomo, H., Park, S.,Yamamoto, S., Sugiyama, H. Amplification of Fluorescent DNA Through Enzymatic Incorporation of a Highly Emissive Deoxyguanosine Analogue. *RSC Adv.* 2014; *4*; 31341–31344.

25. Yamamoto, S., Park, S., and Sugiyama, H. Development of a Visible Nanothermometer with a Highly Emissive 2'-*O*-Methylated Guanosine Analogue. *RSC Adv.* 2015; *5*; 104601–104605.

26. Okamura, I., Park, S., Hiraga, R., Yamamoto, S., Sugiyama, H. Synthesis, Photophysical Properties, and Enzymatic Incorporation of an Emissive Thymidine Analogue. *Chem. Lett.* 2017; *46*; 245–248.

27. Jares-Erijman, E. A., Jovin, T. M. FRET Imaging. *Nat. Biotechnol.* 2003; *21*; 1387–1395.

28. Preus, S., Wilhelmsson, L. M. Advances in Quantitative FRET-Based Methods for Studying Nucleic Acids. *ChemBioChem* 2012; *13*; 1990–2001.

29. Bood, M., Sarangamath, S., Wranne, M. S., Grøtli, M., Wilhelmsson, L. M. Fluorescent Nucleobase Analogues for Base–Base FRET in Nucleic Acids: Synthesis, Photophysics and Applications. *Beilstein J. Org. Chem.* 2018; *14*; 114–129.

30. Kato, T., Kashida, H., Kishida, H., Yada, H., Okamoto, H., Asanuma, H. Development of a Robust Model System of FRET Using Base Surrogates Tethering Fluorophores for Strict Control of Their Position and Orientation within DNA Duplex. *J. Am. Chem. Soc.* 2013; *135*; 741–750.

31. Börjesson, K., Preus, S., El-Sagheer, A. H., Brown, T., Albinsson, B., Wilhelmsson, L. M. Nucleic Acid Base Analog FRET-Pair Facilitating Detailed Structural Measurements in Nucleic Acid Containing Systems. *J. Am. Chem. Soc.* 2009; *131*; 4288–4293.

32. Han, J. H., Yamamoto, S., Park, S., Sugiyama, H. Development of a Vivid FRET System Based on a Highly Emissive dG-dC Analogue Pair. *Chem. Eur. J.* 2017; *23*; 7607–7613.

33. Han, J. H., Park, S., Hashiya, F., Sugiyama, H. Approach to the Investigation of Nucleosome Structure by Using the Highly Emissive Nucleobase thdG–tC FRET Pair. *Chem. Eur. J.* 2018; *24* ; 17091–17095.

34. Hirashima, S., Han, J. H., Tsuno, H., Tanigaki, Y., Park, S., Sugiyama, H. New Size-Expanded Fluorescent Thymine Analogue: Synthesis, Characterization, and Application. *Chem. Eur. J.* 2019; *25*; 9913–9919.

35. Han, J. H., Hirashima, S., Park, S., Sugiyama, H.

Highly Sensitive and Selective Mercury Sensor Based on Mismatched Base Pairing With [diox]T. *Chem. Commun.* 2019; *55*; 10245–10248.

36. Wee, A. W., Yum, J. H., Sugiyama, H., Park, S. Synthesis and Application of a ^{19}F-labeled Fluorescent Nucleoside as a Dual-mode Probe for i-motif DNAs. *RSC Chem. Biol.* 2021; *2*; 876–882.

37. Hirashima, S., Park, S., Sugiyama, H. Evaluation by Experimentation and Simulation of a FRET Pair Comprising Fluorescent Nucleobase Analogs in Nucleosomes. *Chem. Eur. J.* 2023; 29, e202203961.

38. Kumagai, T., Kinoshita, B., Hirashima, S., Sugiyama, H., Park, S. Thiophene-extended Fluorescent Nucleosides as Molecular Rotor-type Fluorogenic Sensors for Biomolecular Interactions. *ACS Sens.* 2023; *8*, 923–932.

Fluorination of Tetraphenylporphyrin Zinc Complex Enhances the Protein Photodamaging Activity through Electron Transfer Mechanism

Kazutaka Hirakawa[1,2,3*], Satoki Matsui[1], and Shigetoshi Okazaki[4]

[1] Applied Chemistry and Biochemical Engineering Course, Department of Engineering, Graduate School of Integrated Science and Technology, Shizuoka University, Johoku 3-5-1, Naka-ku, Hamamatsu 432-8561, Japan
[2] Department of Optoelectronics and Nanostructure Science, Graduate School of Science and Technology, Shizuoka University, Johoku 3-5-1, Naka-ku, Hamamatsu, Shizuoka 432-8561, Japan
[3] Cooperative Major in Medical Photonics, Shizuoka University, Johoku 3-5-1, Hamamatsu 432-8561, Japan
[4] Preeminent Medical Photonics Education and Research Center, Hamamatsu University School of Medicine, Handayama 1-20-1, Higashi-ku, Hamamatsu, Shizuoka 431-3192, Japan

*Corresponding author:

Prof. Dr. Kazutaka Hirakawa
Tel.: (+)81-53-478-1287; Fax: (+)81-53-478-1287
E-mail: hirakawa.kazutaka@shizuoka.ac.jp

ABSTRACT

Photosensitized protein-damaging activity of tetraphenylporphyrins was examined. Tetrakis(pentafluorophenyl) porphyrin zinc complex (ZnT5FPP) photosensitized the oxidation of human serum albumin (HSA), whereas zinc complexes of tetraphenylporphyrin (ZnTPP) and tetrakis(4-fluorophenyl)porphyrin (ZnT1FPP) did not show protein-photodamaging ability. Fluorination enhanced the oxidative activity of zinc porphyrin through the electron transfer mechanism; the redox potential of one-electron reduction of ZnT5FPP (-0.84 V vs. SCE) was significantly higher than that of ZnTPP (-1.25 V) and ZnT1FPP (-1.21 V). The singlet oxygen ($^1O_2$)–generating activity of these zinc porphyrins was also confirmed; and their quantum yields were almost the same. The inhibition of protein photodamage by sodium azide, a $^1O_2$ quencher, showed that the $^1O_2$-mediated mechanism partly contributes to the protein photodamage by ZnT5FPP. However, the protein photodamage was not completely inhibited by an excess amount of sodium azide. Because the Gibbs energy of photoinduced electron transfer from tryptophan to the photoexcited ZnT5FPP is negative (-0.47 eV), electron-transfer oxidation is possible in terms of thermodynamics. These results suggest that fluorination can enhance the protein-photodamaging activity of tetraphenylporphyrin zinc complexes through the electron transfer mechanism.

Keywords

Tetraphenylporphyrin zinc complex; Fluorination; Protein photodamage; Singlet oxygen; Electron transfer

INTRODUCTION

Porphyrin is a well-known endogenous photosensitizer that can produce singlet oxygen ($^1O_2$) under visible-light irradiation [1-3]. Various metal complexes of porphyrins can be formed [1], and the zinc ion is one of the most important intrinsic metal ions [4]. Porphyrin zinc complexes can be easily formed, and the synthesis of zinc porphyrins is relatively easy [5]. Therefore, porphyrin zinc complexes have been studied as photosensitizers, including for use in photodynamic therapy (PDT) of cancer [1,6-8]. In general, $^1O_2$ production is an important mechanism of biomolecule oxidation by photoexcited zinc porphyrins [6]. Photoinduced electron transfer is another important mechanism of photosensitized biomolecule oxidation [9-11]. A photosensitizer molecule's high redox potential is advantageous for its photooxidative activity through electron transfer [9-11]. However, the redox potential of zinc porphyrins is relatively low and is not appropriate for the photooxidation of biomolecules

through electron transfer [12]. Because tumor tissue exists in hypoxic conditions [13], the effect of the $^1O_2$ mechanism is restricted, and the effect of the electron transfer mechanism may be preserved in the tumor environment [9-11]. Previous reports have demonstrated that the fluorination of zinc porphyrins can increase the redox potential [14]. In this study, the possibility of electron transfer–mediated protein oxidation by a fluorinated porphyrin zinc complex was examined. Non-fluorinated and fluorinated porphyrins were used as photosensitizers (Fig. 1).
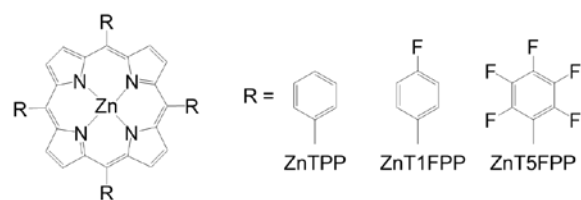

Fig. 1. Structures of zinc porphyrins.

EXPERIMENTAL

Tetraphenylporphyrin (TPP) was purchased from Sigma-Aldrich Co. LLC. (St. Louis, MO, USA). Tetrakis(4-monofluorophenyl)porphyrin (T1FPP) and tetrakis(pentafluorophenyl)porphyrin (T5FPP) were synthesized according to the Adler method [15]. These zinc complexes, ZnTPP, ZnT1FPP, and ZnT5FPP were obtained by the treatment of the corresponding free-base porphyrin with zinc acetate (FUJIFILM Wako Pure Chemical Co., Ltd. (Osaka, Japan) according to the previous report [14]. Human serum albumin (HSA) was purchased from Sigma-Aldrich Co. LLC. Dimethyl sulfoxide (DMSO) and sodium azide (NaN_3) were purchased from FUJIFILM Wako Pure Chemical Co., Ltd. (Osaka, Japan). Spectroscopic-grade water was purchased from Dojin Chemicals Co. (Kumamoto, Japan). Methylene blue was obtained from Kanto Chemical, Co., Inc. (Tokyo, Japan). Sodium phosphate buffer (0.1 M, pH 7.6) was obtained from Nacalai Tesque Inc. (Kyoto, Japan). These chemical agents were used as received.

Redox potential of zinc porphyrins in benzonitrile was measured with a potentiostat/galvanostat (HA-301, Hokuto Denko Co., Tokyo, Japan), a digital function generator (DF1906, NF Co., Yokohama, Japan), and a midi logger (GL900-4, Graphtec Co., Yokohama, Japan), using a platinum working electrode (BAS Inc., Tokyo, Japan), a platinum counter electrode (BAS Inc.), and saturated calomel electrode (SCE, BAS Inc.). The absorption spectra of samples were measured with the UV-VIS spectrophotometer UV-1650PC (Shimadzu, Kyoto, Japan). The fluorescence spectra of samples were measured with an F-4500 fluorescence spectrophotometer (Hitachi, Tokyo, Japan). The fluorescence lifetime (τ_f), which equals the singlet excited-state (S_1) lifetime, of zinc porphyrin and HSA was measured with a Fluorescence Lifetime System TemPro (HORIBA, Kyoto, Japan). The excitation wavelength for the τ_f measurements for zinc porphyrins and HSA were 402 nm and 294 nm, respectively. The fluorescence quantum yield (Φ_f) was measured with an absolute photoluminescence quantum yield measurement system (C9920-20, Hamamatsu Photonics KK, Hamamatsu, Japan). The $^1O_2$ production was directly measured by near-infrared luminescence at around 1,270 nm from $^1O_2$ relaxation, which corresponds to the $^1O_2$ ($^1\Delta_g$)-$^3O_2$($^3\Sigma_g^-$) transition, as reported previously [16].

To evaluate the HSA damage, the sample solution containing 5 μM zinc porphyrins and 10 μM HSA was prepared in a 10 mM sodium phosphate buffer (pH 7.6) including 5% ethanol. The sample solution was irradiated with a light-emitting diode (LED, λ_{max}= 585 nm, 2.0 mW cm^{-2}, CCS Inc., Kyoto, Japan). The intensity of the LED was measured with an 8230E optical power meter (ADC Corporation, Tokyo, Japan). The fluorescence intensity of HSA at 350 nm was measured with a Hitachi 650-60 fluorescence photometer. The excitation wavelength for this assay was 298 nm. The amount of damaged HSA was estimated from the results of fluorometry based on the diminishment of the intrinsic fluorescence of tryptophan residue of HSA by photooxidation, as reported previously [9-11].

RESULTS AND DISCUSSION

Electrochemical properties of zinc porphyrins

The cyclic voltammograms are shown in Fig. 2. Typical oxidation and reduction peaks were observed. The redox potentials of one-electron oxidation (E_{ox}) of ZnTPP, ZnT1FPP, and ZnT5FPP are listed in Table 1. The redox potential of ZnT5FPP was relatively large, suggesting strong oxidative ability through photoinduced electron transfer. The redox potentials of one-electron reduction (E_{red}) of these zinc porphyrins in water were roughly calculated using dielectric continuum theory [17] using the following equation:

$$E_{red} = E_{ox} + \frac{e}{8\pi\epsilon_0 r}\left(\frac{1}{\epsilon_{bz}} - \frac{1}{\epsilon_w}\right) - E_{0\text{-}0} \tag{1}$$

where e is the elementary charge (1.602×10^{-19} C), ϵ_0 is the permittivity of the vacuum, r is the radius of zinc porphyrins, ϵ_{bz} is the dielectric constant of benzonitrile (25.2), ϵ_w is that of water (78.5), and $E_{0\text{-}0}$ is the excitation energy of zinc porphyrins, which was calculated from the fluorescence maximum. The r was calculated by the density functional theory at the ωB97X-D/6-31+G* level (ZnTPP: 5.38 Å; ZnT1FPP: 5.43 Å; and ZnT5FPP: 5.62 Å), utilizing the Spartan'20 (Wavefunction Inc., Irvine, CA, USA). The calculated volumes of ZnTPP, ZnT1FPP, and ZnT5FPP were 651.25 Å^3, 651.25 Å^3, and 651.25 Å^3, respectively, and the r values were estimated under the assumption that these zinc porphyrins are sphere. The obtained values of $E_{0\text{-}0}$ are listed in Table 1. The tryptophan residue of protein is easily oxidized through photoinduced electron transfer. Thus, the Gibbs energy (ΔG) for the electron-transfer oxidation of tryptophan by photoexcited zinc porphyrins was roughly calculated using the following equation:

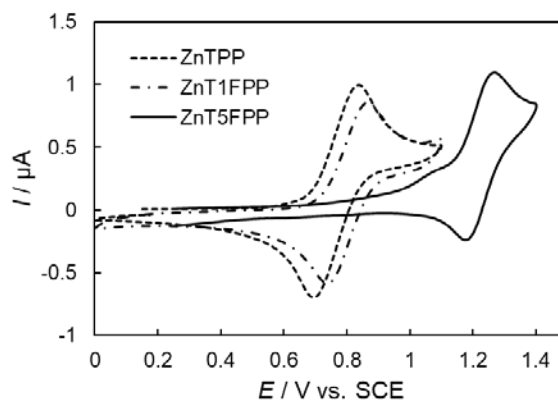$$\Delta G = - e(E_{red} - E_{ox}') - E_{0\text{-}0} \tag{2}$$

Fig. 2. Cyclic voltammograms of zinc porphyrins.

where E_{ox}' is the redox potential of one-electron oxidation of amino acid (tryptophan) (0.78 V vs. SCE in an aqueous solution) [18]. The estimated ΔG values are listed in Table 1. These results demonstrate the relatively strong oxidative activity of ZnT5FPP through electron transfer in the photoexcited state.

Singlet oxygen production photosensitized by zinc porphyrins

A typical near-infrared emission at around 1270 nm assigned to the $^1O_2$ was detected during photoirradiation of these zinc porphyrins. The quantum yield of $^1O_2$ production (Φ_Δ) was estimated by comparison with the near-infrared emission intensity using methylene blue (Φ_Δ of methylene blue: 0.52, [19]). The estimated Φ_Δ of ZnTPP, ZnT1FPP, and ZnT5FPP in ethanol were 0.90, 0.91, and 0.93, respectively (Table 2). The Φ_Δ of ZnT5FPP is slightly larger than that of ZnTPP and ZnT1FPP. The triplet excited (T_1) state energy of ZnT5FPP (1.70 eV) [20] is also larger than that of ZnTPP and ZnT1FPP (1.61 eV) [21]. The large values of these Φ_Δ suggest that these zinc porphyrins can photooxidize biomolecules through $^1O_2$ production.

Interaction between human serum albumin and zinc porphyrins

The absorption spectra of the zinc porphyrins were changed by the addition of HSA, a water-soluble protein (Fig. 3), similarly to other previously reported porphyrin cases [9]. This absorption spectral change can be explained by the interaction between zinc porphyrin molecules and HSA. The apparent binding constant (K) between zinc porphyrin molecules and HSA was calculated using the Benesi-Hildebrand equation [22] under the assumption that one zinc porphyrin molecule binds to the HSA surface (1:1 complex). The estimated K values for ZnTPP, ZnT1FPP, and ZnT5FPP were 9.5×10^4 M^{-1}, 9.6×10^4 M^{-1}, and 7.1×10^4 M^{-1}, respectively. These results suggest that pentafluorophenyl groups slightly decrease the interaction between zinc porphyrin molecules and HSA.

The binding position of zinc porphyrins on HSA was roughly estimated using the Förster resonance energy transfer (FRET) method based on the energy-transfer theory [23] with a previously reported procedure [10]. The average diameter of HSA is about 80 Å [24], and the tryptophan residue is located almost at the center of HSA [25]. The critical distances of the FRET from the tryptophan to the zinc porphyrin molecules, which were calculated from the fluorescence spectrum of tryptophan and the absorption spectrum of these zinc porphyrins, were 29.8 Å (ZnTPP), 26.1 Å (ZnT1FPP), and 33.0 Å (ZnT5FPP). However, the τ_f of the tryptophan residue of HSA, which was not decreased by these zinc porphyrins. These results suggest that these zinc porphyrin molecules bind to the HSA surface.

Photosensitized HSA oxidation by zinc porphyrins

The photosensitized HSA damage by these zinc porphyrins was evaluated using the fluorescence intensity of the tryptophan residue of HSA, which shows the typical fluorescence as being around 350 nm, as reported previously [9-11]. HSA photodamage by ZnTPP and ZnT1FPP was barely observed, whereas ZnT5FPP photosensitized the HSA damage (Fig. 4). The quantum yield of HSA photodamage by ZnT5FPP (Φ_D: 4.3×10^{-4}) was estimated from the initial decomposition rate and the absorbed photon fluence by ZnT5FPP (Table 2). Since the apparent binding constants of ZnTPP and ZnT1FPP were rather larger than that of ZnT5FPP, the difference in binding position may affect the photosensitized HSA–damaging activity of these zinc porphyrins. The HSA photodamage by ZnT5FPP was partially (44%) inhibited by the addition of NaN$_3$, a $^1O_2$ quencher [26]; suggesting the contribution of $^1O_2$. The $^1O_2$ production activity of ZnT5FPP was confirmed as mentioned above. However, HSA damage was observed in the presence of NaN$_3$. The HSA damage photosensitized by ZnT5FPP with NaN$_3$ can be explained by the electron transfer mechanism. The contribution of the electron transfer mechanism was speculated to be 56%. The calculated ΔG (Table 1) supported tryptophan oxidation by the photoexcited ZnT5FPP through electron transfer.

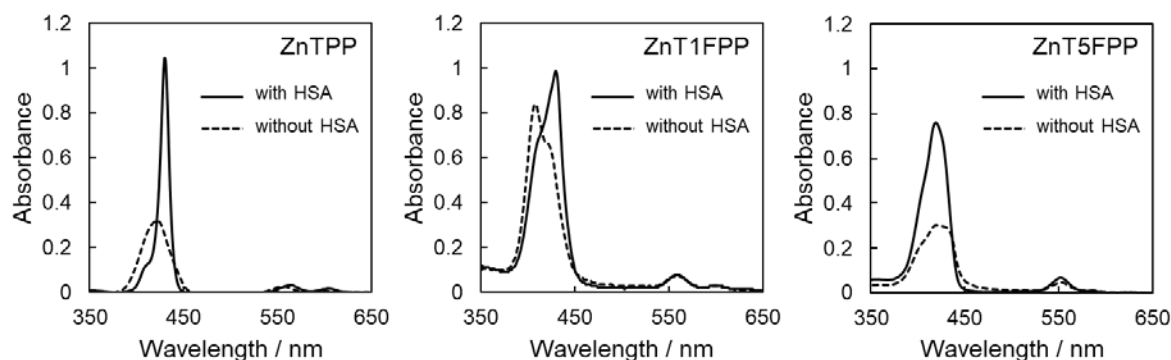The analyzed fluorescence lifetimes (τ_f) of ZnT5FPP

Fig. 3. Absorption spectra of zinc porphyrins with or without HSA. The sample solution contained 5 μM zinc porphyrins with or without 10 μM HSA in a 10 mM sodium phosphate buffer (pH 7.6) plus 5% ethanol.
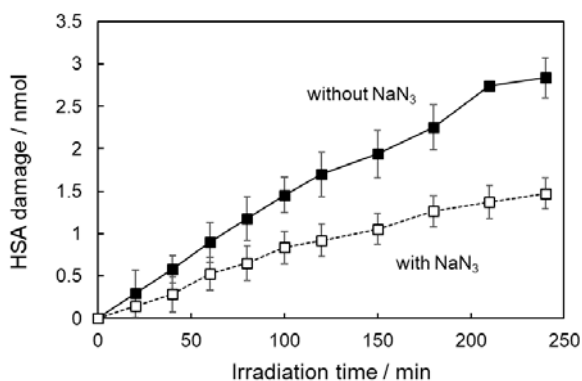
Fig. 4. The time profile of photosensitized HSA damage by ZnT5FPP. The sample solution contained 5 μM ZnT5FPP and 10 μM HSA with (□) or without (■) 10 mM NaN_3 in a 10 mM sodium phosphate buffer (pH 7.6) plus 5% ethanol. The sample solution was irradiated with an LED (λ_{max}= 585 nm, 2.0 mW cm^{-2}). Data represents the mean ± SD (n = 3).

without HSA were as follows: 0.05 ns (85%), 0.40 ns (13%), and 2.15 ns (2%). The shortest lifetime species can be explained by the self-aggregation of ZnT1FPP molecules. These values suggest that the photoexcited state of most ZnT5FPP molecules was deactivated through self-aggregation. In the presence of HSA, the τ_f values were changed to 0.23 ns (45%), 1.40 ns (38%), and 5.21 ns (17%). The longest lifetime can be explained by the fact that the vibrational deactivation of photoexcited ZnT5FPP was inhibited by interaction with HSA, as previously reported [27]. The shortest and middle lifetimes may be explained by the electron transfer quenching of photoexcited ZnT1FPP molecules. The electron-transfer rate constant (k_{ET}) from tryptophan to photoexcited ZnT5FPP can be speculated by the following equation:

$$k_{ET} = \frac{1}{\tau_{f1}} - \frac{1}{\tau_{f2}} \tag{3}$$

where τ_{f1} is the shortest (0.23 ns) or middle (1.40 ns) lifetime, and τ_{f1} is the longest lifetime (5.21 ns). The calculated values of k_{ET} were 4.2×10^9 s^{-1} and 5.2×10^8

s^{-1}. The rate constant of the diffusion-controlled process (7.4×10^4 s^{-1}), which is calculated from the diffusion-controlled rate coefficient in water at 298 K (7.4×10^9 M^{-1} s^{-1}) and the concentration of ZnT5FPP, was much smaller than that of the estimated values. These findings kinetically support the association of ZnT5FPP molecules with HSA and the electron transfer-mediated oxidation of HSA by the S_1 of ZnT5FPP. The T_1 state energy level of ZnT5FPP is relatively low (1.70 eV) [20], and the estimated ΔG value is small (-0.07 eV). Therefore, the possibility of electron transfer oxidation of HSA by the T_1 state of ZnT5FPP can be excluded.

HSA has one tryptophan residue [25], which can be easily damaged by $^1O_2$ and electron transfer mechanism [9,10,27,28]. Tryptophan oxidation could be used as an indicator to evaluate the extent of protein damage. However, other amino acids of HSA can be damaged through $^1O_2$ production and the electron transfer mechanism. A previous report showed that P(V) porphyrins photosensitize the oxidation of tyrosine, methionine, histidine, cysteine, and arginine through these mechanisms [28]. It can be speculated that ZnT5FPP photosensitize the oxidation of tyrosine (E_{ox}' = 0.84 V vs. SCE [29], ΔG = -0.38 eV), methionine (E_{ox}' = 1.01 V vs. SCE [30], ΔG = -0.21 eV), and cysteine (E_{ox}' = 0.80 V vs. SCE [31], ΔG = -0.42 eV) through the electron transfer from the thermodynamic point of view. These ΔG values were roughly calculated using the equation (1). Other amino acids, histidine and arginine, may be oxidized by ZnT5FPP through $^1O_2$ mechanism.

CONCLUSIONS

ZnTPP, ZnT1FPP, and ZnT5FPP could photosensitize $^1O_2$ production in ethanol. These zinc porphyrins bound to HSA, a water-soluble protein. However, ZnTPP and ZnT1FPP could not induce HSA photodamage, the oxidation of tryptophan residue. These results can be explained by the fact that the binding position of ZnTPP and ZnT1FPP is not appropriate for the photooxidation

Table 1 Redox potential of zinc porphyrins and the Gibbs energy of the electron-transfer oxidation of tryptophan

Porphyrin	E_{ox} / V [a]	E_{red} / V [b]	E_{0-0} / eV [c]	ΔG / eV
ZnTPP	0.77	-1.25	2.06	-0.03
ZnT1FPP	0.80	-1.21	2.05	-0.06
ZnT5FPP	1.22	-0.84	2.10	-0.47

[a]: Redox potential of one-electron oxidation in benzonitrile. [b]: Redox potential of one-electron reduction in an aqueous solution. [c]: S_1 energy in an aqueous solution.

Table 2 Quantum yield of photosensitized HSA damage by zinc porphyrins

Porphyrin	Φ_D	$\Phi_{D(ET)}$ [a]	$\Phi_{D(SO)}$ [b]	Φ_Δ [d]
ZnTPP	ND [c]	ND	ND	0.90
ZnT1FPP	ND	ND	ND	0.91
ZnT5FPP	4.3×10^{-4}	2.4×10^{-4}	1.9×10^{-4}	0.93

[a]: Quantum yield of HSA damage through electron transfer mechanism. [b]: Quantum yield of HSA damage through $^1O_2$ mechanism. [c]: HSA damage was not observed. [d]: in ethanol.

of tryptophan. The calculated ΔG values show that the possibility of electron transfer–mediated oxidation by ZnTPP and ZnT1FPP is very small. ZnT5FPP could oxidize HSA under photoirradiation. HSA damage by ZnT5FPP could be explained by the mechanisms of $^1O_2$ production and electron transfer (Fig. 5). The quantum yields of relaxation process of photoexcited zinc porphyrins are listed in Table 3. The observed values of Φ_Δ are comparable to the quantum yield of intersystem crossing (Φ_{isc}) of zinc porphyrin [32,33]. Therefore, it can be speculated that the Φ_{isc} is almost the same as the Φ_Δ. Because the fluorescence intensity of zinc porphyrins was barely decreased by HSA, the determination of electron transfer quantum yield (Φ_{ET}) was difficult. However, this value must be greater than the $\Phi_{D(ET)}$. The pentafluorophenyl groups of ZnT5FPP significantly increase the redox potential, leading to the enhancement of electron-transfer oxidation activity of zinc porphyrins in the S_1 state. In general, zinc porphyrins are recognized as a $^1O_2$ generator under visible-light irradiation. This study showed that fluorination can improve the activity of biomolecule oxidation by zinc porphyrins through the electron transfer mechanism.

Acknowledgments

Notes

The authors declare no conflict of interests.

References

1. Lang K, Mosinger J, Wagnerová DM. Photophysical properties of porphyrinoid sensitizers non-covalently bound to host molecules; models for photodynamic therapy. Coord Chem Rev, 2004;248:321–350.

2. Kou J, Dou D, Yang L. Porphyrin photosensitizers in photodynamic therapy and its applications. Oncotarget, 2017;46:81591–81603.

3. Tian J, Huang B, Nawaz MH, Zhang W. Recent advances of multi-dimensional porphyrin-based functional materials in photodynamic therapy. Coord Chem Rev, 2020;420:213410.
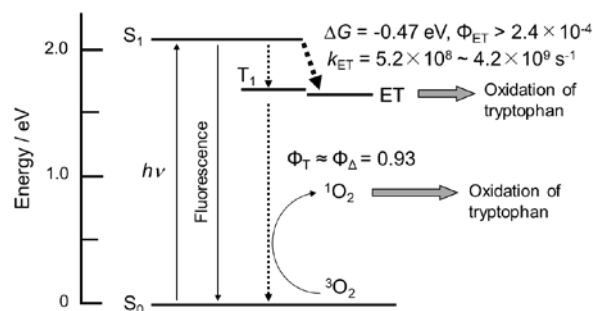

Fig. 5. The relaxation process of photoexcited ZnT5PP and the oxidation mechanism of HSA. ISC: intersystem crossing. ET: electron transfer state (ZnT5FPP anion radical-tryptophan cation radical).

4. Maret W, Li Y. Coordination dynamics of zinc in proteins. Chem Rev, 2009;109:4682–4707.

5. Buchler, JW. Static coordination chemistry of metalloporphyrins. Porphyrins and Metalloporphyrins; Smith, KM. Ed.; Elsevier Scientific Publishing Company: New York, 1975; Chapter 5.

6. Ding K, Zhang Y, Si W, Zhong X, Cai Y, Zou J, Shao J, Yang Z, Dong X. Zinc(II) mtalated porphyrins as photothermogenic photosensitizers for cancer photodynamic/photothermal synergistic therapy. ACS Appl Mater Interfaces, 2018;10:238–247.

7. Benov L, Craik J, Batinic-Haberle I. Protein damage by photo-activated Zn(II) N-alkylpyridylporphyrins. Amino Acids, 2012;42:117–128.

8. Pola M, Kolarova H, Ruzicka J, Zholobenko A, Modriansky M, Mosinger J, Bajgar R. Effects of zinc porphyrin and zinc phthalocyanine derivatives in photodynamic anticancer therapy under different partial pressures of oxygen in vitro. Invest New Drugs, 2021;39:89–97.

9. Hirakawa K, Ouyang D, Ibuki Y, Hirohara S, Okazaki S, Kono E, Kanayama N, Nakazaki J, Segawa H. Photosensitized protein-damaging activity, cytotoxicity, and antitumor effects of P(V)porphyrins using long-wavelength visible light through electron transfer. Chem Res Toxicol, 2018;31:371–379.

10. Hirakawa K, Takai S, Horiuchi H, Okazaki S. Photooxidation activity control of dimethylaminophenyltris-(N-methyl-4-pridinio)porphyrin by pH. ACS Omega, 2020;5:27702−27708.

11. Hirakawa K, Murata A. Photosensitized oxidation of nicotinamide adenine dinucleotide by diethoxyphosphorus(V)tetraphenylporphyrin and its

Table 3 Quantum yield of relaxation process of photoexcited zinc porphyrins

Porphyrin	$\Phi_f{}^a$	$\Phi_{isc}{}^b$	$\Phi_{ET}{}^c$
ZnTPP	0.034	0.90	ND
ZnT1FPP	0.042	0.91	ND
ZnT5FPP	0.022	0.93	$> 2.4 \times 10^{-4}$

[a]: in ethanol. [b]: speculated value ($\Phi_{isc} = \Phi_\Delta$) in ethanol. [c]: The quantum yield of electron transfer from tryptophan to photoexcited zinc porphyrin. This value must be greater than the quantum yield of HSA oxidation through the electron transfer mechanism.

fluorinated derivative: Possibility of chain reaction. Spectrochim Acta A, 2018;188:640−646.

12. Kalyanasundaram K, Neumann-Spallart M. Photophysical and redox properties of water-soluble porphyrins in aqueous media. J Phys Chem, 1982;86:5163−5169.

13. Yoshihara T, Hirakawa Y, Hosaka M, Nangaku M, Tobita S. Oxygen imaging of living cells and tissues using luminescent molecular probes. J Photochem Photobiol C, 2017;30:71–95.

14. Hirakawa K, Saito K, Segawa H. Anomalously selective quenching of S_2 fluorescence from upper excited state of zinc 5-(1'-Pyrenyl)-10,15,20-triphenylporphyrin derivatives through intramolecular charge transfer state. J Phys Chem A, 2009;113:8852–8856.

15. Adler AD, Longo FR, Finarelli JD, Goldmacher J, Assour J, Korsakoff L. A Simplified synthesis for meso-Tetraphenylporphine. J Org Chem, 1967;32:476.

16. Hirakawa K, Nishimura Y, Arai T, Okazaki S. Singlet oxygen generating activity of an electron donor connecting porphyrin photosensitizer can be controlled by DNA. J Phys Chem B, 2013;117:13490–13496.

17. Weller A. Photoinduced electron transfer in solution. Z Phys Chem Neue Folge, 1982;133:93–98.

18. Sakura S. Chemiluminescence of tryptophan enhanced by electrochemical energy. Electrochim Acta, 1992;37:2731–2735.

19. Usui Y, Kamogawa K. A standard system to determine the quantum yield of singlet oxygen formation in aqueous solution. Photochem Photobiol, 1974;19:245–247.

20. Spellane PJ, Gouterman M, Antipas A, Kim S, Liu YC. Porphyrins. 40. Electronic spectra and four-orbital energies of free-base, zinc, copper, and palladium tetrakis(perfluorophenyl)porphyrins. Inorg Chem, 1980;19:386–391.

21. Walters VA, de Paula JC, Jackson B, Nutaitis C, Hall K, Lind J, Cardozo K, Chandran K, Raíble D, Phillips CM. Electronic structure of triplet states of zinc(II) tetraphenylporphyrins. J Phys Chem, 1995;99:1166–1171.

22. Benesi HA, Hildebrand JH. A spectrophotometric investigation of the interaction of iodine with aromatic hydrocarbons. J Am Chem Soc, 1949;71:2703–2707.

23. Förster Th. Zwischenmolekulare energiewanderung und fluoreszenz. Ann Physik, 1948;437:55−75.

24. Ferrer ML, Duchowicz R, Carrasco B, de la Torre JG, Acuña AU. The conformation of serum albumin in solution: a combined phosphorescence depolarization-hydrodynamic modeling study. Biophys J, 2001;80:2422–2430.

25. He XM, Carter DC. Atomic structure and chemistry of human serum albumin. Nature, 1992;358:209–215.

26. Li MY, Cline CS, Koker EB, Carmichael HH, Chignell CF, Bilski P. Quenching of singlet molecular oxygen ($^1O_2$) by azide anion in solvent mixtures. Photochem Photobiol, 2001;74:760–764.

27. Hirakawa K, Yoshida M, Hirano T, Nakazaki J, Segawa H. Photosensitized protein damage by diethyleneglycoxyP(V)tetrakis(*p-n*-butoxyphenyl)porphyrin through electron transfer: Activity control through self-aggregation and dissociation. Photochem Photobiol, 2022; 98:434–441.

28. Ouyang D, Hirakawa K. Photosensitized enzyme deactivation and protein oxidation by axial-substituted phosphorus(V) tetraphenylporphyrins. J Photochem Photobiol B, 2007;175: 125-131.

29. Sun L, Burkitt M, Tamm M, Raymond MK, Abrahamsson M, LeGourrierec D, Frapart Y, Magnuson A, Kenez P.H, Brandt P, Tran A, Hammarström L, Styring S, Åkermark B. Hydrogen-bond promoted intramolecular electron transfer to photogenerated Ru(III): a functional mimic of tyrosinez and histidine 190 in photosystem II. J Am Chem Soc, 1999;121:6834–6842.

30. Tan WT, Goh JK. Electrochemical oxidation of methionine mediated by a fullerene-C_{60} modified gold electrode. Electroanalysis, 2008;20:2447–2453.

31. Beitollahi H, Ganjali MR, Norouzi P, Movlaee K, Hosseinzadeh R, Tajik S. A novel electrochemical sensor based on graphene nanosheets and ethyl 2-(4-ferrocenyl-[1,2,3]triazol-1-yl) acetate for electrocatalytic oxidation of cysteine and tyrosine. Measurement, 2020;152:107302.

32. Taniguchi M, Lindsey JS, Bocianb DF, Holten D. Comprehensive review of photophysical parameters (ε, Φ_f, τ_s) of tetraphenylporphyrin (H_2TPP) and zinc tetraphenylporphyrin (ZnTPP)–critical benchmark molecules in photochemistry and Photosynthesis. J Photochem Photobiol C, 2021;46:100401.

33. Bachilo SM, Weisman RB. Determination of triplet quantum yields from triplet−triplet annihilation fluorescence. J Phys Chem A, 2000;104:7711–7714.

Author Guidelines

Submission of manuscripts

Editor-in-Chief requests authors to submit manuscripts via e-mail <dts211@gmail.com>. Manuscripts must be submitted as Microsoft Word or compatible software (doc or docx files). Figures should be prepared as high resolution (>300 dpi) JPEG files. Only black and white figures are available. Word limit for summary must be 250 words. Authors for whom English is not a mother tongue may submit their manuscript to professional English Editing Service. The work to be submitted has not been published before, is not considered for publication elsewhere. The manuscript for submission must be carefully written and approved fully by all authors. Color artwork is free for submission.

Editor-in-Chief

Daisuke Tsuruta, MD, PhD
Department of Dermatology
Graduate School of Medicine, Osaka Metropolitan University
1-4-3 Asahimachi, Abeno-ku,
Osaka 545-8585, Japan

Manuscript types

Photomedicine and Photobiology accepts original articles, review articles, and letters to the editor. Color figures are normally not applicable for the submission.

Original articles are investigative studies in fields such as photomedicine, photobiology, and photochemistry. It should not exceed 3500 words (10,000 characters in Japanese), including 250 words (750 characters in Japanese) abstract, Figure legends (excluding references), and a maximum of 4 figures/ tables.

Review articles are for authors essentially invited by Editors. However, suggestions from readers are welcome. It should not exceed 5000 words (15,000 characters in Japanese), including 250 words (750 characters in Japanese) abstracts, figure legends (excluding references), and maximum of 5 figures/tables

Letters to the Editor are for brief reports. Word count limits for this category are 1500 words (4,000 characters in Japanese), including legends (excluding references) with 2 figures or tables. Reference should not exceed 10 in number. Abstract is not required for this category.

Manuscript arrangement

The manuscript should be written in either English or Japanese. Double spaced typing and minimal margin of 25 mm are required. Each manuscript requires following: 1) Title page, 2) Abstract and 3-5 key words, 3) Text, 4) acknowledgements, 5) References, 6) Tables/Figures with separate legends. Please number each page. Structured abstract, including Background, Methods, Results and Conclusions, is requested. The abstract should be written in English even if the manuscript was written in Japanese.

References

Number references consecutively in the order appeared in the text. Identify references by Arabic numerals in parentheses. Ex) (1). List all authors when 6 or less. When 7 or more authors exist, list only the first 3 and add "et al." Journal titles should be properly abbreviated according to Index Medicus style. Examples of references are as follows:
1. Rahmani F, Razaei N. Therapeutic targeting of Toll-like receptors: a review of Toll-like receptors and their signaling pathways in psoriasis. Expert Rev Clin Immunol, 2016;12:1289-1298.
2. Frain-Bell W. The photodermatoses. In: Rook A, ed. Recent advances in dermatology. Edinburgh: Churchill Livingstone, 1973: 101-133.

Conflict of Interest

Please disclose all conflict of interests. These include financial, personal, political, intellectual or religious interests.

Offprints

PDF offprint will be provided for authors. If additional printed offprints are required, the authors can order them via e-mail <dts211@gmail.com>.

「Photomedicine and Photobiology」投稿規定

1．筆頭著者は日本光医学光生物学会員とし，共著者は原則として日本光医学光生物学会員に限る．

2．投稿内容は original article（原著），review article（総説），letter to the editor（短報）を主とし，和文または英文で他誌に掲載されていないものとする．投稿原稿は和文と英文のいずれも可とする．

3．投稿原稿の執筆要綱は下記のとおりとする．
　原著（英文 3,500 語，和文 10,000 字）：
　　医学，薬学，生物学，化学，物理学などの分野における光に関連した研究論文．
　　本文，要約，図の説明を含む（参考文献は除く）．図・表は 4 点以内．
　総説（英文 5,000 語，和文 15,000 字）：
　　原則，編集者からの依頼原稿であるが購読者からの推薦も歓迎する．
　　本文，要約，図の説明を含む（参考文献は除く）．図・表は 5 点以内．
　短報（英文 1,500 語，和文 4,000 字）：
　　臨床症例報告や速報的研究．
　本文，図の説明を含む．参考文献は 10 編以内．要約は不要．図・表は 2 点以内．
　　要約は英語で 250 字以内とする．
　　図・表が制限を超える場合については，編集委員会で調整する．

4．原稿は英文あるいは和文で Microsoft Word かそれと互換性のあるソフトウェア（doc or docx file）で作成し，メールで dts211@gmail.com へ提出する．

5．原稿には 1）タイトルページ，2）要約と key words（3－5 個），3）本文，4）謝辞，5）参考文献，6）図・表の説明を記載し，頁番号をつける．

6．要約は和文，英文に関わらず英語（250 語）で，背景，方法，結果，結論と構造化して記載する．

7．図は高解像度（300 dpi 以上）で JPEG ファイルで作成し必ず説明を付ける．図は白黒のみとする．

8．文献は本文に用いられたもののみをあげる．引用番号は本文の引用順とし，本文中の引用箇所にアラビア数字を入れた括弧を記載する．例（1）．

9．文献は，下記の形式に従って記載する．著者は 6 名以下の場合は全員を，7 名以上の場合は最初の 3 名を記載し，「他」または et al. を付ける．雑誌名は Index Medicus に従い適切に略記する．
（例）Rahmani F, Razaei N. Therapeutic targeting of Toll-like receptors: a review of Toll-like receptors and their signaling pathways in psoriasis. Expert Rev Clin Immunol, 2016;12:1289-1298.

　　Frain-Bell W. The photodermatoses. In: Rook A, ed. Recent advances in dermatology. Edinburgh: Churchill Livingstone, 1973: 101-133.

10．利益相反に関してはすべて記載する．

11．著者には PDF のオフプリントを提供します．印刷版が必要な場合はメールでご注文ください．

ヤヌスキナーゼ（JAK）阻害剤

薬価基準収載

リンヴォック®錠

30 mg
15 mg
7.5 mg

ウパダシチニブ水和物錠

RINVOQ

劇薬　処方箋医薬品^(注)　　　　　注）注意－医師等の処方箋により使用すること

● 効能又は効果、用法及び用量、警告・禁忌を含む注意事項
等情報等については電子化された添付文書（電子添文）
を参照してください。

製造販売元
アッヴィ合同会社
東京都港区芝浦3-1-21

〔文献請求先及び問い合わせ先〕
くすり相談室
フリーダイヤル 0120-587-874

2022年11月作成
JP-RNQD-210013-4.0

abbvie

世界中の人々の
より豊かな人生のため、
革新的医薬品に
思いやりを込めて

Lilly

日本イーライリリーは製薬会社として、
人々がより長く、より健康で、充実した生活を実現できるよう、
がん、糖尿病、筋骨格系疾患、中枢神経系疾患、自己免疫疾患、
成長障害、疼痛などの領域で、日本の医療に貢献しています。

日本イーライリリー株式会社
〒651-0086 神戸市中央区磯上通 5-1-28
www.lilly.co.jp

患者様の想いを見つめて、薬は生まれる。

顕微鏡を覗く日も、薬をお届けする日も、見つめています。
病気とたたかう人の、言葉にできない痛みや不安。生きることへの希望。
私たちは、医師のように普段からお会いすることはできませんが、
そのぶん、患者様の想いにまっすぐ向き合っていたいと思います。
治療を続けるその人を、勇気づける存在であるために。
病気を見つめるだけではなく、想いを見つめて、薬は生まれる。
「ヒューマン・ヘルスケア」。それが、私たちの原点です。

ヒューマン・ヘルスケア企業 エーザイ

Eisai

hhc
human health care

AFUTUREFREEOFLF
Global Alliance

エーザイはWHOのリンパ系フィラリア病制圧活動を支援しています。

選択肢をつくる。
希望をつくる。

なんでも選べるこの時代に、
まだ選択肢が足りない世界があります。
そこでは、たったひとつの選択肢が生まれることが、
たくさんの希望につながります。
だから、田辺三菱製薬はつくります。

病と向き合うすべての人に、希望ある選択肢を。

この国でいちばん長く培ってきた
薬づくりの力を生かして、
さまざまな分野で、挑みつづけていきます。
そこに待っている人がいるかぎり。

田辺三菱製薬
https://www.mt-pharma.co.jp/

MITSUBISHI
CHEMICAL
GROUP

生まれは日本。
新しい作用機序を持った
一日一回服用の帯状疱疹治療薬。

2.禁忌(次の患者には投与しないこと)
2.1 本剤の成分に対し過敏症の既往歴のある患者
2.2 リファンピシンを投与中の患者[10.1、16.7.1 参照]

4.効能・効果
○帯状疱疹
○再発性の単純疱疹

5 .効能・効果に関連する注意
〈再発性の単純疱疹〉
5.1 単純疱疹(口唇ヘルペス又は性器ヘルペス)の同じ病型の再発を繰り返す患者であることを臨床症状及び病歴に基づき確認すること。
5.2 患部の違和感、灼熱感、そう痒等の初期症状を正確に判断可能な患者に処方すること。
5.3 口唇ヘルペス又は性器ヘルペス以外の病型に対する臨床試験は実施されていない。[17. 1. 2、17. 1. 3 参照]

6.用法・用量
〈帯状疱疹〉
通常、成人にはアメナメビルとして1回400mgを1日1回食後に経口投与する。
〈再発性の単純疱疹〉
通常、成人にはアメナメビルとして1200mgを食後に単回経口投与する。

7.用法・用量に関連する注意
〈効能共通〉
7.1 空腹時に投与するとアメナメビルの吸収が低下し、効果が減弱するおそれがあるので、食後に服用するよう患者に指導すること。食前又は食間のタイミングで服用する必要がある場合は、軽食等を摂取した上で服用させること。[16.2.1 参照]
〈帯状疱疹〉
7.2 本剤の投与は、発病初期に近いほど効果が期待できるので、早期に投与を開始すること。なお、目安として皮疹出現後5日以内に投与を開始することが望ましい。
7.3 本剤は、原則として7日間使用すること。改善の兆しが見られないか、あるいは悪化する場合には、速やかに他の治療に切り替えること。
〈再発性の単純疱疹〉
7.4 初期症状発現後速やかに本剤を服用することが望ましい。初期症状発現から6時間経過後に服用した患者、また口唇ヘルペスでは皮疹(水疱、膿疱、びらん、潰瘍、痂皮)発現後に服用した患者に対する有効性を裏付けるデータは得られていない。[8.参照]
7.5 次回再発分の処方は1回分に留めること。

8 .重要な基本的注意
〈再発性の単純疱疹〉
次回再発分として処方する場合は、次のことを患者に十分説明し、患者が理解したことを確認すること。[7.4参照]

・初期症状(患部の違和感、灼熱感、そう痒等)出現後6時間以内に服用すること。また、口唇ヘルペスでは皮疹(水疱、膿疱、びらん、潰瘍、痂皮)発現前に服用すること。
・妊婦又は妊娠している可能性のある女性、授乳中の女性は、服用せずに医療機関を受診すること。

9. 特定の背景を有する患者に関する注意(一部抜粋)
9.1 合併症・既往歴等のある患者
9.1.1 免疫機能の低下を伴う患者
悪性腫瘍や自己免疫性疾患など免疫機能の低下を伴う患者に対する有効性及び安全性は確立していない。

10.相互作用
アメナメビルはCYP3Aで代謝される。またCYP3A 及び2B6 を誘導する。[16.4参照]
10.1 併用禁忌(併用しないこと)
リファンピシン(リファジン)
10.2 併用注意(併用に注意すること)
CYP3Aの基質となる薬剤(ミダゾラム、プロチゾラム、ニフェジピン等)、CYP3Aを阻害する薬剤(リトナビル、クラリスロマイシン等)、グレープフルーツジュース、シクロスポリン、CYP3Aを誘導する薬剤(リファブチン、カルバマゼピン、フェノバルビタール等)、セイヨウオトギリソウ(St.John's Wort、セント・ジョーンズ・ワート)含有食品、CYP2B6の基質となる薬剤(エファビレンツ)

11.副作用
次の副作用があらわれることがあるので、観察を十分に行い、異常が認められた場合には投与を中止するなど適切な処置を行うこと。
11.1 重大な副作用
11.1.1 多形紅斑(頻度不明)
11.2 その他の副作用(一部抜粋)
NAG増加、α1ミクログロブリン増加

承認条件:医薬品リスク管理計画を策定の上、適切に実施すること。

●詳細は電子添文をご参照ください。●電子添文の改訂にご留意ください。

処方箋医薬品※
抗ヘルペスウイルス剤

薬価基準収載

アメナリーフ®錠200mg
Amenalief® Tablets : アメナメビル 錠
※注意—医師等の処方箋により使用すること